3D seismic analysis of subsurface gas migration and the gas hydrate system offshore Mauritania

JINXIU YANG

How to cite:

YANG, JINXIU (2013) 3D seismic analysis of subsurface gas migration and the gas hydrate system offshore Mauritania. Doctoral thesis, Durham University.

Department of Earth Sciences, Durham University

3D seismic analysis of subsurface gas migration and the gas hydrate system offshore Mauritania

Jinxiu Yang

A thesis submitted in partial fulfilment of the requirements for the degree of
Doctor of Philosophy at Durham University

2013

Table of Contents

List of Figures

Abstract

3D seismic data are used in this thesis to investigate fluid migration processes and the gas hydrate system offshore Mauritania. The studied interval was deposited during the Neogene, characterised by fine-grained hemipelagic sediments, polygonal faults, mass transport complexes (MTCs), high amplitude anomalies (HAAs), and a widespread bottom simulating reflection (BSR).

In the study area, there are many localized HAAs above some MTCs. Their spatial relationship indicates that there was upward gas migration up the margins or local faults associated with the MTCs. One possible gas source could be dissociated hydrates due to the upward resetting of the BSR, but there may be other sources like in situ biogenic gas. At shallower depth, a gravity-driven fault below the BSR acted as a conduit for gas recycling after hydrate dissociation. There is a close spatial relationship among the fault location, a breached gas accumulation and a shallower free gas zone (FGZ), suggesting the process of gas recycling between hydrates and another gas trap. The BSR is investigated which is composed of alternating high and low amplitudes and characterized by amplitude bands on the BSR map. The high amplitude bands are interpreted to be caused by free gas trapped below the base of gas hydrates, potentially in spaced beds of coarser sediments. These amplitude bands provide evidence of lateral changes in the ambient conditions that control the depth of the BSR, including the variable water depth of the slope, impingement of salt diapir and mud diapir, and canyon cutting at the seabed.

Generally this thesis exemplifies the potential of 3D seismic data in studying the gas hydrate system and related processes. For example, mapping the BSR on 3D seismic data can show lateral changes of the BSR at different depths from only one map, representing an effective method to study the base of gas hydrates.

List of Abbreviations

AGC - Automatic Gain Control
BSR - Bottom simulating reflection
BHSZ - Base of the gas hydrate stability zone
DHI - Direct hydrocarbon indicator
DMO - Dip Move Out
FGZ - Free gas zone
E-W - East to west
GHSZ - Gas hydrate stability zone
Gt - Gigatonne
HHA - High amplitude anomaly
Hz - Hertz, unit of frequency
m m.y.$^{-1}$ - Metre per million years
ms - Millisecond
m s^{-1} - Metre per second
MTC - Mass transport complex
NE-SW - Northeast to Southwest
NW-SE - Northwest to Southest
NMO - Normal Move Out
NW - Northwest
OBC - Ocean-bottom cable
ODP - Ocean drilling program
P-T - Pressure and temperature
P-wave - Primary wave or pressure wave
RMS - Root-mean-square
s - Second
S-wave - Secondary wave or shear wave
TOC - Total Organic Carbon
TWT - Two-way-travel time
3D - Three dimensional
2D - Two dimensional

Declaration

I declare that this thesis, which I submit for the degree of Doctor of Philosophy at Durham University, is my own work and no part of this thesis has previously been submitted for a degree at this or any other university. The work is entirely my own except where reference is made.

Jinxiu Yang

Durham University

Department of Earth Sciences

September 2013

Acknowledgements

First and foremost, I would like to thank my principal supervisor, Professor Richard Davies. His excellent supervision has helped me grow up to an independent researcher. He can always spot my bad habits in researching and remind me to rectify them. At the same time he is never sparing with his compliments and always praises me at the first time when I make some small progress. Thanks also go to Richard's family, his wife April and his two lovely boys. They always make me feel warm whenever I visit.

Sincere thanks go to my second supervisor Neil Goulty, who gave me many good advices. Mads Huuse, Richard Hobbs, Jonny Imber, Jon Gluyas, Qiliang Sun, Shiguo Wu and Yaoling Niu are also thanked for their suggestions to investigate the particular scientific problems I encountered in the research. I thank Joe Cartwright, Qiliang Sun and two other anonymous reviewers of my papers for their helpful comments and suggestions. Dave Stevenson and Gary Wilkinson are thanked who provided essential IT support.

My friends in Durham, Li Li, Hongliang Wang, Hui Huang, Amélie Leduc, Fran Watson, Kate Thatcher, Helen Foster, Suzane Qassim, Leo Newport, Li Su, Cui Liu, Lilian Jiang, Yan Qu, Xuan Chen, Alex B-J, Alex Cicchino and Jing Zhang, thank you all for your friendship and support.

Especially I would like to thank Durham University and China Scholarship Council for supporting my research. Without their support, I would not have the chance to do my PhD here in Durham. Tullow Oil and Petronas are thanked for providing the 3D seismic data on which the research is based. Landmark Graphics Corporation provided Landmark software as part of the LGC University support grant for which I am very grateful.

Finally, I want to dedicate this thesis to my family, my husband Zhenkun Dai, my parents Hongkui Yang and Jing Cao, and my brother Jinhua Yang. Thank you for believing in me all the time. Your support and unconditional love can always spirit me up and give me the strength to overcome any difficulties I meet.

Chapter 1: Introduction

1.1 Research context

Gas hydrates have been recovered globally in permafrost, marine and lake environments (Shipley et al., 1979; Yakushev and Chuvilin, 2000; Vanneste et al., 2001). Research on gas hydrates is increasingly gaining attention from all over the world because gas hydrates are regarded as a potential future energy source which may play a role in affecting global climate change, geological hazards and evolution of oceanic margin (Bünz et al., 2003; Brown et al., 2006; Haacke et al., 2007). In marine environments gas hydrates mainly occur in the uppermost sediments of a few hundreds of metres, at ocean water depths greater than ~400 m and shallower than 3000 m (Fig. 1.1; Shipley et al., 1979; Klauda and Sandler, 2005; Westbrook et al., 2009).

Fig. 1.1 Map of the globe showing the predicted locations of gas hydrates (blue) in water depth < 3000 m (after Klauda and Sandler, 2005; Davies et al., 2012a).

Bottom simulating reflections (BSRs) and fluid migration conduits are obvious seismic features on continental margins (e.g. Shipley et al., 1979; Haacke et al., 2007). There are two types of BSRs, diagenesis-related and hydrate-related (e.g. Berndt et al., 2004). A hydrate-related BSR is a useful seismic indicator to detect the base of gas hydrate stability zone (BHSZ). It is caused by the acoustic impedance contrast between the hydrate-bearing sediments above the reflection and the underlying free gas-charged sediments (e.g. Shipley et al., 1979; Kvenvolden, 1998; Bünz et al., 2003). The high-resolution three-dimensional

(3D) seismic data offshore Mauritania allow accurate mapping of the subsurface in this area, which enables detailed investigation of the base of gas hydrates and related processes.

Although gas hydrates are considered to be a potential energy resource, the specific mechanisms of gas supply for hydrate formation are poorly defined (e.g. Haacke et al., 2007). According to Xu and Ruppel (1999), in natural gas hydrate systems including passive continental margins with low flux, the gas used for hydrate formation is mainly transported by upward fluid advection from below. It is also possible that the in situ biogenic gas generated within the GHSZs is used to form gas hydrates (Hyndman and Davis, 1992).

When the hydrate stability conditions change, gas hydrates will dissociate and release a large volume of gas and water, which may increase the pore pressure and potentially cause overpressure (Schroeter et al., 1983; Haq, 1998; Dickens et al., 1995; Kwon et al., 2008). It has been widely proposed that there may be a significant relationship between hydrate dissociation and submarine slope failures (Katz et al., 1959; McIver, 1977; Dillon and Paull, 1983; Paull et al., 1991). Furthermore hydrate dissociation would lead to the redistribution of hydrocarbons as free gas or hydrate phase to adjust to the new hydrothermal conditions (Tohidi et al., 2001). There are two main sinks for dissociated gas from hydrates: some could be recycled back to the hydrate systems to form hydrates or be trapped in free gas zones (FGZs) below the BSR, and some could be stored in new free gas traps such as stratigraphic traps (Rempel and Buffett, 1997; Pecher et al., 2001; Davies and Clarke, 2010; Yang and Davies, 2013).

On seismic data, a BSR is normally observed as a reflection which is approximately parallel to the seabed and crosscuts stratigraphy (Shipley, 1979; Berndt et al., 2004). However theoretically there should be some lateral changes in the BSR reflection due to the lateral lithological variations or vertical tectonism such as uplift, subsidence, and diapirism (Hübscher and Kukowski, 2003). The seismic amplitude of the BSR reflection may change according to the different concentrations of hydrates and gas which are controlled by the physical properties of sediments (Rodrigo et al., 2009). Since the 3D seismic data offshore Mauritania are of high frequency and the BSR is widespread in this area, detailed mapping can be used to study the base of gas hydrates, FGZ locations, and their planar distribution.

Studies of gas hydrates have been the focus for many geoscientists worldwide (Hyndman and Davis, 1992; Pecher et al., 1996; Bangs et al., 2010). The research in this thesis contributes to the knowledge of gas hydrates in terms of understanding the related fluid migration processes below the BSR and controls on the BSR itself. Chapter 3 demonstrates that the aligned margins of MTCs can act as pathways for upward gas migration; chapter 4 introduces the role of gravity-driven faults in gas recycling between gas hydrates and other gas accumulations; and chapter 5 analyses the geological controls on the gas hydrate systems such as the BSR which marks the position of the base of gas hydrates, as well as the FGZs.

1.2 Gas hydrate systems

Gas hydrates are widely regarded as a potential future energy resource, and it is estimated that the reserve in gas hydrates is twice as large as the conventional hydrocarbon resources (Shipley et al., 1979; Kvenvolden, 2002). So gas hydrates probably represent an important component of the global carbon cycle (Dickens, 1999, 2001abc). Many geoscientists have published global or regional estimates of submarine gas hydrates in the past 40 years (e.g. Trofimuk et al., 1973; McIver, 1981; Hovland et al., 1997; Kvenvolden, 1999; Milkov et al., 2003; Mosher, 2011). Based on their research, the global estimates of hydrate-bound gas decreased gradually from the order of 10^{17}-10^{18} to 10^{14}-10^{15} m^3, probably due to the growing knowledge of the distribution and concentration of gas hydrates (Milkov, 2004).

Until now most of the papers on gas hydrates mainly focus on the distribution of the BSR and related processes like fluid migration, gas recycling and slope slumping, which are probably much easier to detect on seismic data (e.g. Field and Kvenvolden, 1985; Paull et al., 1991). However to accurately estimate the reserves of gas hydrates and to understand their specific roles in climate change and slope evolution, people need to know more about the details of gas hydrate layers such as the distribution, thickness, porosity, saturation and physical property changes during hydrate formation and dissociation (Milkov, 2004). To achieve this, data integration is needed which requires many data such as seismic data, well logging data, core data, chemical analysis data or reliable seismic velocity data (Wood et al., 1994; LeBlanc et al., 2007).

1.2.1 Gas hydrate stability zones (GHSZs)

The stability of gas hydrates is mainly controlled by pressure and temperature (P-T) conditions and GHSZs often occur in environments of high pressure and low temperature (Field and Kvenvolden, 1985; Sloan, 1998; Brown et al., 1996; Bünz et al., 2003). As shown in the phase diagram (Fig. 1.2a), the stability zone of hydrates is defined by three curves, confined by the intersection depths of the hydrate stability curve with the water temperature profile and the heat flow profile. Theoretically the top of the GHSZ is located in the sea water, controlled by the intersection of the hydrate stability curve and the water temperature profile (Fig. 1.2a). But normally people regard the seabed as the top of GHSZ because the hydrates in seawater do not survive long and will float upwards and decompose due to its low density and instability (MacDonald et al., 1994; Paull et al., 1994). The base of the GHSZ (BHSZ) occurs where the hydrate stability curve intersects the heat flow profile and may be marked by a BSR on seismic data (Fig. 1.2a). So the location of the BSR is mainly related to the bottom water temperature, water depth, burial depth and local heat flow

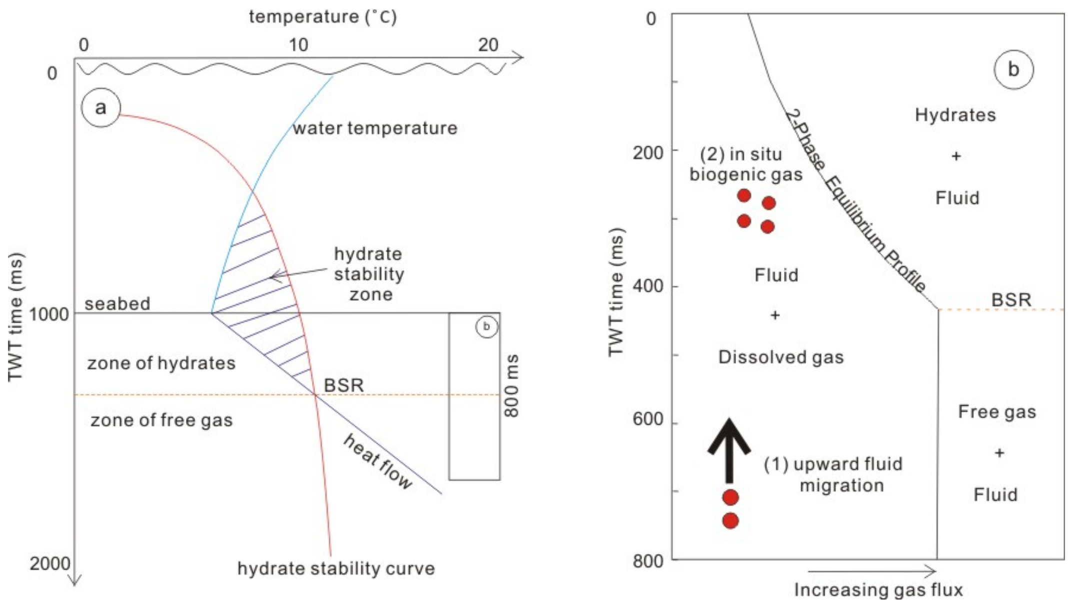

Fig. 1.2 (a): A schematic diagram showing the equilibrium conditions of a GHSZ, mainly controlled by the hydrate stability curve and the heat flow profile (from Xu and Ruppel, 1999). Free gas can be sealed below the GHSZ as a separate phase. (b): Another schematic diagram showing three gas phases (dissolved gas, free gas and gas hydrates) controlled by depth and gas flux (from Davie and Buffett, 2003; Milkov et al., 2004). Two mechanisms of gas supply are proposed, upward fluid migration and in situ biogenic gas.

from the earth (e.g. Mosher, 2011). Additionally, hydrate formation may also be affected by other factors like salinity, gas composition, even the physical properties of host sediments (e.g. Cooper and Hart, 2002). When the pore fluid gas concentration in the GHSZ reaches gas saturation (maximum gas solubility), additional gas production will lead to the formation of hydrates (Fig. 1.2b; Paull et al., 1994; Xu and Ruppel, 1999). However, some other researchers proposed that it is possible that dissolved gas can be used to form gas hydrates (Brown et al., 1996; Haacke et al., 2007).

As introduced in section 1.1, there are two main types of BSR on seismic data, diagenesis-related and hydrate-related (e.g. Shipley et al., 1979; Berndt et al., 2004). These two types of BSR are often characterized by strong reflection strength due to the high acoustic impedance contrast, and both cross-cut stratigraphy. A diagenesis-related BSR is caused by a diagenetic transition, often from opal A to opal CT, but the smectite-illite conversion or a sudden increase in the abundance of authigenic carbonates can also lead to the occurrence of diagenesis-related BSRs (Isaacs, 1982; Davies and Cartwright, 2002; Berndt et al., 2004). A hydrate-related BSR is the key seismic indicator of gas hydrates, and it is thought to be more controlled by the free gas below rather than the overlying hydrates because a minor amount of free gas can change the seismic velocity significantly (Dai et al., 2004; Riedel et al., 2006). The hydrate-related BSR gets deeper as the seabed depth increases, while the diagenesis-related BSR often has a constant depth below the seabed or even gets shallower as the seabed depth increases due to earlier opal transition at greater pressure (Hübscher and Kukowski, 2003; Berndt et al., 2004).

The occurrence of gas hydrates is not always accompanied by an obvious BSR on seismic data, and hydrates may exist where there is no BSR (Bünz et al., 2003; Kumar et al., 2006). According to Holbrook et al. (1996), on Leg 164 gas hydrates were proven to exist at three sites (994, 995 and 997) which were drilled along a transect extending from the ridge flank on the Blake Ridge. However no clear BSR is observed at Site 994 which is located on the southern flank of Blake Ridge, while at Site 997 which is located on the crest of Blake Ridge there is a prominent BSR (Paull et al., 1996). The visibility of a clear BSR is closely related to the topography because distinct BSRs are always observed in areas where the BSR crosscuts stratal reflections at an acute angle and it is hard to recognize a BSR when the hydrate-charged sediment layers are parallel to stratal reflections (Horozal et al., 2009). Although it is widely accepted that gas hydrates occur above the BSR, it is also possible that hydrates and free gas coexist below the BSR which have been observed on the Blake Ridge (Paull et al., 1996; Guerin et al., 1999). That can be caused by the capillary effects of the smaller pores in finer-grained sediments which increase the temperature of hydrate dissociation or by remaining crystalline structures after partial hydrate dissociation (Guerin et al., 1999).

The dissociation of gas hydrates may occur when gas hydrate equilibrium conditions change, which is regarded as a factor in causing overpressure and sediment weakening (Paull et al., 2000; Kwon et al., 2008). When the hydrate stability equilibrium conditions change due to processes like sedimentation, erosion, bottom water temperature change or diapirism, the GHSZ will reset upwards or downwards to the new equilibrium depth range (Rempel and Buffett, 1997; Pecher et al., 2001). As the BHSZ resets upwards, the hydrates at the base of hydrate zone will dissociate, potentially resulting in generating overpressure due to the large volume of released gas and water. The released gas can be recycled back to the hydrate system driven by the overpressure, or stay in other gas traps below the new GHSZ sealed by faults or fine-grained sediments (e.g. Davies and Clarke, 2010). A downward shift of the BHSZ is usually followed by conversion of gas to hydrates, adjusting to new hydrate equilibrium conditions (e.g. Bangs et al., 2010).

1.2.2 Gas sources for hydrate formation

Rempel and Buffett (1997) proposed two sources of gas for hydrate formation (Fig. 1.2b). One is biogenic gas generated from in situ organic-rich sediments within the GHSZ. The other is gas flux into the GHSZ by fluid migration from below, either biogenic or thermogenic (Paull et al., 1994). The latter mechanism is of great importance to the gas hydrate system because the biogenic gas formed within the GHSZ is often considered to be insufficient to ensure the occurrence of gas hydrates (Hyndman and Davis, 1992; Xu and Ruppel, 1999; Haacke et al., 2007). The origin of gas, biogenic or thermogenic, can be determined by analysing the isotopic and compositional data (Rice and Claypool, 1981; Paull et al., 1994).

The biogenic gas mainly consists of methane, with $C_1/C_{1\text{-}5}$ ratio greater than 0.98 (Bernard et al., 1976; Rice and Claypool, 1981; Vially, 1992). It can originate from the decomposition of organic matter by anaerobic microorganisms in rapidly accumulating sediments, especially under low temperatures at shallower depth (Bernard et al., 1976; Rice and Claypool, 1981). As a result, areas of low heat flow and higher burial rate are prone to produce more biogenic gas (Paull et al., 1994; Vially, 1992). Gas hydrates are prone to occur in the upper few hundreds of metres on the continental margins under low temperature and high pressures where biogenic gas may be present.

Thermogenic gas is produced at greater depths (more than 1 km) by thermal cracking of organic matter or oil (Bernard et al., 1976; Sassen et al., 1999; Sassen et al., 2001), and significant quantities of thermogenic gas cannot be generated until temperature reaches 100 °C (Rice and Claypool, 1981). Thermogenic gas often contains heavier hydrocarbons from deep hot hydrocarbon systems, with methane/ethane ratio less than 100 (Sassen et al., 1999). The composition of thermogenic gas is related to the thermal maturity of related source rock and it is suggested that source rocks of higher thermal maturity can produce isotopically heavier carbon than at lower thermal maturity (Sassen, 1988). In this thesis no isotopic or compositional data is available to analyse the origin of gas offshore Mauritania, and only fluid migration processes are investigated which may supply gas to the hydrate zone.

1.3 Fluid migration

Subsurface fluid migration on continental margins is of great significance to marine hydrocarbon systems because it may provide evidence of hydrocarbon migration and distribution, cause slope instability, or even affect climate change (Gay et al., 2003; Bünz et al., 2005; Haacke et al., 2007). Generally there are two mechanisms of fluid migration, diffusion and advection, and it is rare that in one area there is only one single mechanism for gas migration (e.g. Leythaeuser et al., 1982; Berndt, 2005; Gay et al.,2007). Additionally fluid migration has a close relationship with gas hydrate systems. It may supply gas for hydrate formation and provide migration conduits for the released gas from hydrate dissociation (Hyndman and Davis, 1992; Davies and Clarke, 2010; Yang and Davies, 2013).

1.3.1 Diffusion

Diffusion describes the spread of particles through random motion from regions of higher concentration to regions of lower concentration (Krooss et al., 1988; Judd and Hovland, 2007). Diffusion is comparatively inefficient at transporting gas over long distances, and is an exceedingly slow process which disperses rather than concentrates gas (Max, 2003; Judd and Hovland, 2007). Molecular diffusion through water-saturated pore space represents an effective process for primary migration of gas which is dependent on temperature rather than pressure (Leythaeuser et al., 1982; Stainforth and Reinders, 1990). The transport rate by diffusion is also affected by porosity and permeability, adsorption and desorption on clay minerals and kerogen, and salinity of formation waters (e.g. Leythaeuser et al., 1982). Diffusion of hydrocarbons in the subsurface may destroy the existing gas accumulations by dissipation (Leythaeuser et al., 1982; Krooss and Leythaeuser, 1996). As a result, Leythaeuser et al. (1982) proposed that large gas accumulations can persist through long periods of geological time, such as 10^8 years, only when dynamic systems reach steady-state equilibrium between the diffusion-related loss through the cap rock and the continuous replenishment from the source rock.

1.3.2 Advection

Advection is a transport mechanism by fluids due to the bulk motion of fluids in a particular direction (Kopf, 2002). On seismic data focused fluid migration indicated by the presence of chimneys, faults, mud volcanos, sand injections and pockmarks is often regarded as advection transport, probably driven by overpressure (Fig. 1.3; Hovland and Judd, 1988; Pecher et al., 2010; Løseth et al., 2011; Sun et al., 2013). The build-up of overpressure can be linked to reasons in geology, tectonic and geochemistry (Milkov, 2000), such as compressional tectonics (e.g. Sultan et al., 2007), gas generation, high sedimentation rate (e.g. Sun et al., 2012), compaction (Gordon and Flemings, 1998) and diagenetic reactions which release pore fluids (e.g. Bruce, 1984). According to previous studies, focused fluid flow systems are of great significance to hydrocarbon reservoirs (e.g. Abrams, 1992; Gay et al., 2007). As a large capacitor of gas (mainly methane) in the global carbon cycle, gas hydrates are closely related to focused fluid migration (e.g. Hyndman and Davis, 1992; Haacke et al., 2007). Xu and Ruppel (1999) proposed that the gas hydrate layers in advection-dominated systems are thicker than in diffusion-dominated systems for the high rate of fluid flux.

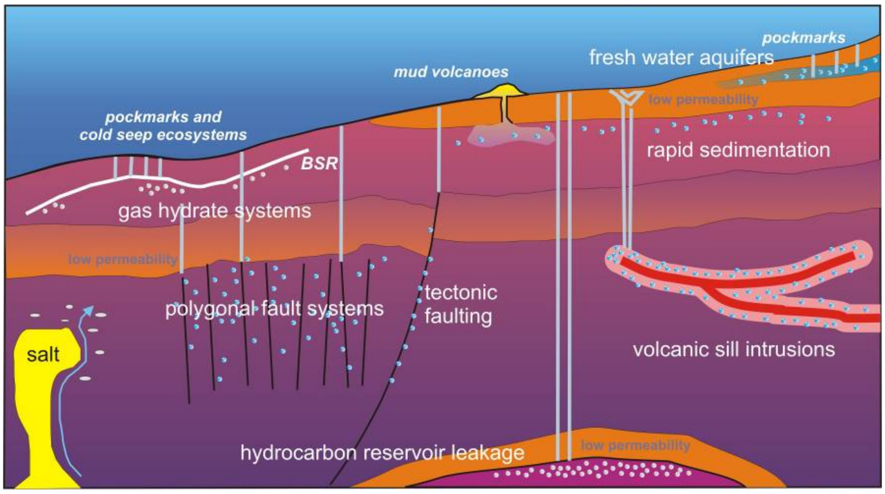

Fig. 1.3 A summary sketch showing focused fluid migration pathways on a passive continental margin and location of the gas hydrate systems (from Berndt, 2005).

1.4 Research objectives

This research focuses on the gas hydrate system on a passive continental margin and investigates related fluid migration processes below the BSR, using the 3D seismic data from offshore Mauritania. 3D seismic datasets used in hydrate studies are quite rare and this is an exceptionally good dataset clearly showing the characteristics of the BSR which marks the base of gas hydrates, as well as other related structures. Fluid migration conduits below gas hydrate systems, such as chimneys and faults, have been widely observed on seismic data and they are interpreted to supply gas to gas hydrate systems or provide pathways for gas recycling between gas hydrate systems and other free gas traps (Abrams, 1992; Berndt, 2005; Yang and Davies, 2013). In this research the high resolution 3D seismic data enable to do detailed mapping of the subsurface to study the gas hydrate system and related processes. The objectives of this thesis are to:

1) Investigate the processes of fluid migration below gas hydrates by analysing the localized amplitude anomalies (chapters 3 and 4). Consider the lateral fluid migration along stratigraphy in these processes. Understand the

relationships among the process of fluid migration, nearby structures and the gas hydrate system.

2) Through mapping the BSR rather than stratal reflections, study the amplitude change of the BSR and its distribution in different areas (chapter 5). Investigate how one could use such mapping to understand the geological controls on the gas hydrate system offshore Mauritania.

1.5 Geological setting

The passive continental margin offshore Mauritania in West Africa is characterized by a relatively narrow shelf and a moderately broad continental rise (Fig. 1.4; Vear, 2005; Antobreh and Krastel, 2007). The opening of the North Atlantic Ocean initiated during the Mid-Jurassic which was probably triggered by seafloor spreading adjacent to the Mauritanian Basin (Vear, 2005; Antobreh and Krastel, 2007). At present the continental slope is generally smooth, with a dip of ~ 1–3° (Henrich et al., 2008).

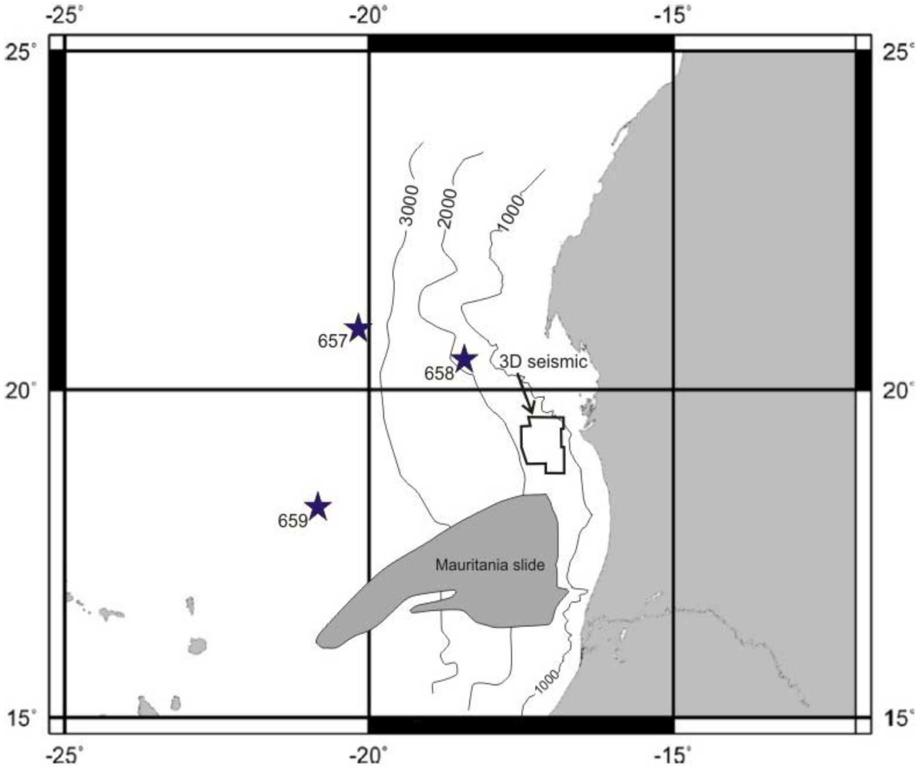

Fig. 1.4 Location map of the continental margin offshore Mauritanian, showing the locations of the Mauritania Slide, nearby three OPD sites (657, 658 and 659) and the 3D seismic data set.

According to Vear (2005), the continental margin offshore Mauritania is a potential petroleum play where the Miocene turbidite channels of high porosity act as reservoirs which are sealed by fine-grained sediments of channel abandonment facies or hemipelagic shale drapes of low permeability. The deep-marine mudstones deposited during the Cenomanian-Turonian or other intervals such as the Albian and the Paleocene may represent possible source rocks (Vear, 2005). The Neogene is comparatively thick in Mauritania, although it is thin along most of the West African margin (Vear, 2005). There are many mass transport complexes (MTCs) formed within the Neogene succession, related to the deposition of poorly consolidated sediments probably due to the high sedimentation rates in the slope environment (Henrich et al., 2008; Antobreh and Krastel, 2007). The Mauritania Slide complex is one of the largest MTCs on the Northwest African continental margin, ~ 34,000 km^2, and it is characterized by retrogressive sliding (Krastel et al., 2006; Davies et al., 2012b). The MTCs studied in this thesis are located to the north of the Mauritania Slide (Fig. 1.4), also featured by retrogressive sliding.

For the last few millions of years, large volumes of aeolian sediments from the Sahara Desert have been transported into this area (Antobreh and Krastel, 2007; Henrich et al., 2008). This thesis focuses on the gas hydrate system and only studies the shallower succession which is characterized by fine-grained turbidites, debris flows and hemipelagic sediments (Vear, 2005; Krastel et al., 2006). The sedimentation rate offshore of Mauritania is variable, from several to hundreds of m m.y.$^{-1}$, controlled by the changes of climate, sediment supply and tectonic setting during geological time (Ruddiman et al., 1988). The interval investigated in this thesis is located between the seabed and ~ 950 ms below, deposited since the Neogene (Vear, 2005). The sedimentation rate for this interval is high, averaging 80-160 m m.y.$^{-1}$, probably due to the ocean margin upwelling regime (Krastel et al., 2006; Henrich et al., 2008).

1.6 Thesis outline

In this section all chapters will be described individually. Chapters 3-5 have been written as manuscripts for publication, and they focus on different topics associated with the gas hydrate system from bottom to top (Fig. 1.5). Each chapter contains introduction, geological background, data and methodology, observations, interpretations, discussion and conclusions, which repeat some contents in chapters 1 and 2. In chapters 3-5, pronouns referring to the author (Jinxiu Yang) appear in the plural form (i.e. we replaces I) as an acknowledgement of co-authors in the manuscripts. The thesis only contains manuscripts for which I am the first author.

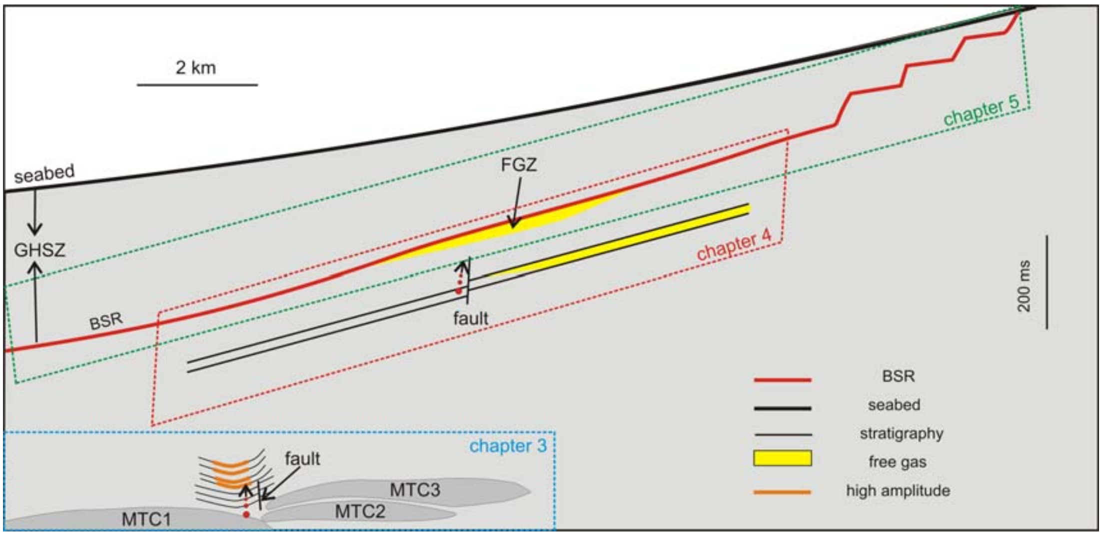

Fig. 1.5 A simplified cross section showing three phenomena from deep to top which will be described in chapters 3, 4 and 5 respectively.

Chapter 1 introduces the research context, research progress in gas hydrate systems and fluid migration. Geological background is also described in this chapter, as well as the objectives of this thesis.

Chapter 2 describes the 3D seismic data and related methodology used in the research, including a brief introduction on data generation and processing. Seismic interpretation is the basis of the main work in this thesis, and its basic principles are described in this chapter as well. Additionally the seismic attributes used in mapping and interpretation are also introduced.

Chapter 3 examines some localized high amplitude anomalies (HAAs) located above some buried MTCs which indicate upward fluid migration controlled by the MTCs. The work in this chapter has been published as: ‘Gas migration below gas hydrates controlled by mass transport complexes, offshore Mauritania’, in the journal of Marine and Petroleum Geology. Richard Davies and Mads Huuse are my co-authors (Doi: 10.1016/j.marpetgeo.2013.09.003).

Approximately 70% of this paper is my own work, with Richard Davies contributing around 25% and Mads Huuse 5%.

Chapter 4 investigates gravitational faults which act as migration pathways for gas recycling after hydrate dissociation. The work in this chapter has been published as: 'Gravity-driven faults: Migration pathways for recycling gas after the dissociation of marine gas hydrates', in *Marine Geology* with Richard Davies as the only co-author (Doi: 10.1016/j.margeo.2012.11.013). Over 70% of the final paper is my own work, with Richard Davies contributing approximately 30%.

Chapter 5 describes a method of mapping the BSR instead of stratigraphic reflections to study the characteristics of the BSR offshore Mauritania and its geological controls. The location of FGZs is also investigated. The work in this chapter is ready to be submitted as 'Controls on the base of gas hydrates offshore Mauritania: determined by 3D seismic imaging of the bottom simulating reflection' with Richard Davies as the only co-author. About 80% of the final manuscript is my own work, with Richard Davies contributing the remaining 20%.

Chapter 6 discusses the principal findings described in this thesis, as well as areas of uncertainties. This chapter also raises some interesting topics for future work, and list the main conclusions.

Chapter 2: Data and methodology

Many types of data and methods have been used to research gas hydrates, such as 2D or 3D seismic data, borehole data, hydrate samples, numerical modelling, and laboratory based analysis of hydrate-bearing sediments (e.g. Shipley et al., 1979; Dickens et al., 2001abc; Hovland et al., 2002; Lee and Collett, 2011; Yang and Davies, 2013). This thesis is mainly based on the analysis of the 3D seismic data offshore Mauritania. No additional data are available here to calibrate the 3D seismic data. However there are some Ocean Drilling Program (ODP) well data in nearby areas (Ruddiman et al., 1988), through which the geological background of the study area can be inferred. The following sections introduce the 3D seismic data such as seismic acquisition, processing, interpretation and related methodologies for seismic studies of gas hydrates. The list of abbreviations provides a brief explanation of the abbreviations used in this thesis.

2.1 3D seismic data

The earth is three-dimensional, and the petroleum reserves are also stored in three-dimensional traps (Brown, 2010). Therefore the application of 3D seismic technology can provide the most complete and precise picture of the subsurface structural and stratigraphic features, increase drilling efficiency and offset some exploration risks (e.g. Cartwright and Huuse, 2005). Compared to traditional 2D seismic data which exerted a major influence on the development of basin analysis in the 1960s and 1970s (Sheriff and Geldart, 1995), 3D seismic data are of significantly higher quality, with a dense grid of lines which enables to map the subsurface features in 3D detail to a resolution of only a few tens of metres, or even just a few metres (Fig. 2.1; Saeland and Simpson, 1982; Brown, 2010; Cartwright and Huuse, 2005; Appendix A).

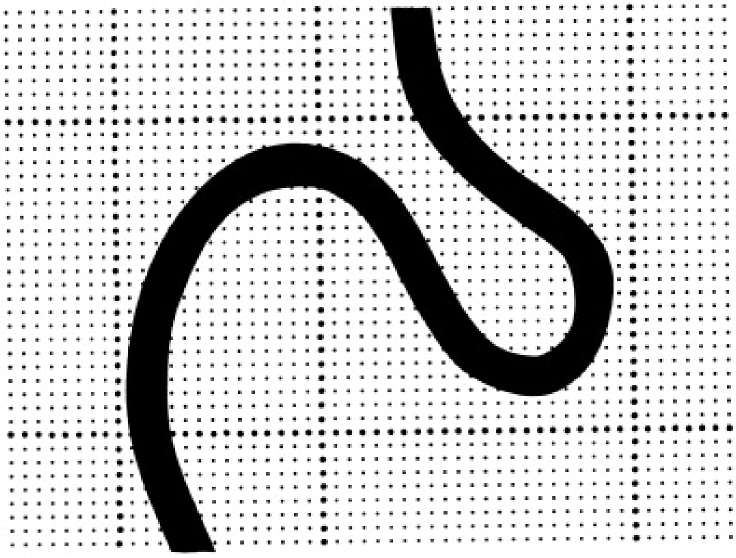

Fig. 2.1 Areal coverage of a 3D survey (fainter dots) compared to the coverage of a grid of five 2D lines (bold dots), and the ability of each to delineate a meandering channel (from Brown, 2010).

2.1.1 Marine seismic data acquisition

An acoustic wave generating device is used to produce body waves which subsequently travel down through the subsurface and are reflected back towards the surface by geological interfaces (e.g. sequence boundaries, unconformities; Bacon et al., 2007). Air guns are the traditional and widely used energy source for the majority of marine seismic surveys (Brown, 2010). The receiving devices detect the reflected signals and measure their amplitude and arrival two-way-travel times after the source is fired. The collected data reveal information about the two-way-travel time to geological interfaces and changes in related rock properties (Bacon et al., 2007). Marine seismic surveys are mainly concerned with P-wave reflections to detect the reflected energy because S-waves do not transmit through fluids as fluid has no capacity for shear (Bacon et al., 2007).

There are two main methods used for marine seismic data acquisition. One uses hydrophones deployed in a streamer or streamers towed behind a vessel at a depth of a few metres, to which the seismic source may be attached (Fig. 2.2; Brown, 2010; Lee et al., 2004). The other one requires that the recording sensors sink to the seafloor and are connected to a stationary recording vessel, called ocean bottom cable (OBC) or ocean bottom seismic (OBS) (Fig. 2.3; Brown, 2010; Rajput et al., 2012). The recording sensors include hydrophones, geophones, or both.

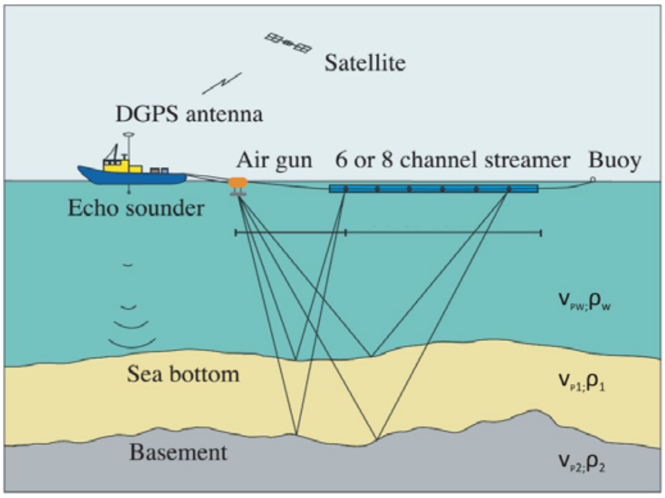

Fig. 2.2 A cartoon showing a method of seismic data acquisition in a marine setting with the streamer towed behind (from Lee et al., 2004).

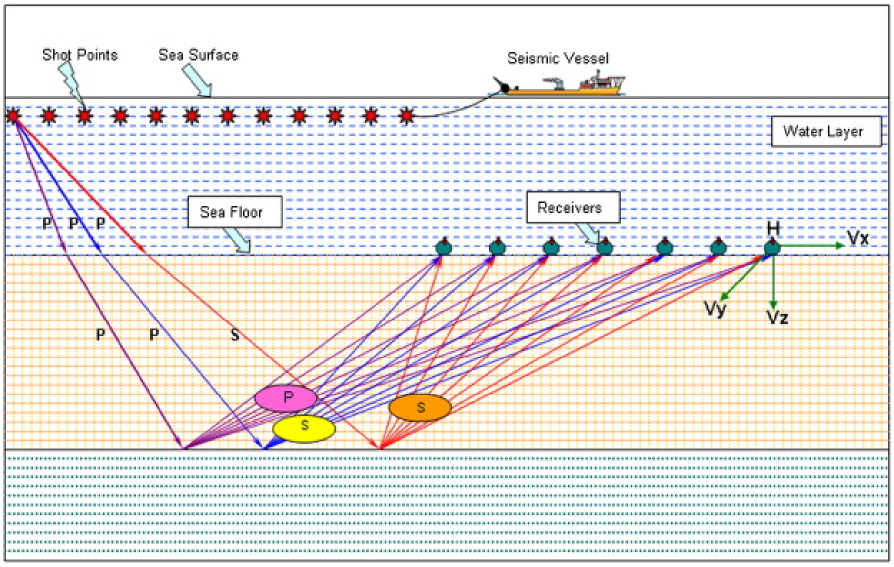

Fig. 2.3 A cartoon showing a method of seismic data acquisition in a marine setting with receivers sinking to the seafloor (from Rajput et al., 2012). H, V_x, V_y and V_z indicate horizontal and vertical velocity components.

The speed at which a seismic wave travels through the subsurface layers is governed by the seismic velocity of the materials in which they are travelling (Bacon et al., 2007). The acoustic impedance of certain material, Z, is defined by the following equation:

$$Z = V_p \rho \qquad \text{Eq. 2.1}$$

where V_p is the velocity of seismic P-wave and ρ is the density of related material.

When seismic waves travel through an interface between two materials with different acoustic impedances, some of the wave energy will reflect at the interface while some will be transmitted through the interface (Benson and Wu, 1999; Bacon et al., 2007). The amplitude of the reflected wave is predicted by multiplying the amplitude of the incident wave by the seismic reflection coefficient R which is determined by the impedance contrast between the two materials above and below the geological interface (Fig. 2.2):

$$R = (V_{p2}\rho_2 - V_{p1}\rho_1) / (V_{p2}\rho_2 + V_{p1}\rho_1) \qquad \text{Eq. 2.2}$$

2.1.2 Processing of seismic data

Due to cost considerations, environmental concerns, topography and other obstructions, the surface acquisition grid is quite coarsely sampled and the offset and azimuth distributions are less than uniform which may lead to spatial variation in the amplitudes and phase of data volume, as well as structural errors (Brown, 2010). As a result, the acquired seismic data cannot be interpreted directly to image the subsurface, and several processing steps are required to manipulate the acquired data into an image that can be used to infer the subsurface structure. The specific objectives of seismic processing are to enhance signal, suppress noise, migrate seismic events to the appropriate location in space, provide velocity information and increase resolution (Bacon et al., 2007).

There are three major steps in seismic processing: deconvolution, stacking and migration (Fig. 2.4). Deconvolution is a process that acts on the data along time axis and improves the temporal resolution by compressing the basic seismic wavelet. Stacking is an iterative process of applying Normal Move Out (NMO), Dip Move Out (DMO) and standard velocity analysis, and finally summation of traces at each common mid-point (Yilmaz and Doherty, 1987). It compresses the data volume in the offset direction and yields the plane of stack section. Migration moves dipping events to their true locations at subsurface, collapses diffraction and thus increases lateral resolution (Yilmaz and Doherty, 1987). Migrating a stacked section is called poststack migration, while migrating a prestacked section is called prestack migration. Additionally there are two other methods to classify migration types (Yilmaz and Doherty, 1987). One is time migration and depth migration, with the final product displaying in either depth or time. The other is 2D migration and 3D migration.

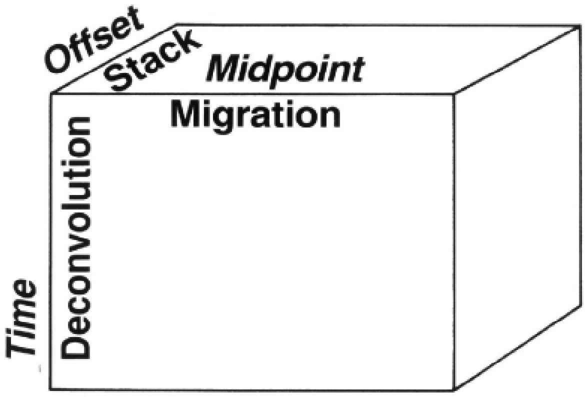

Fig. 2.4 Seismic data volume represented in processing coordinate: midpoint-offset-time (from Yilmaz and Doherty, 1987).

Different migration methods can be used in different areas based on their velocity distribution and structural complexity (Fig. 2.5; Brown, 2010).

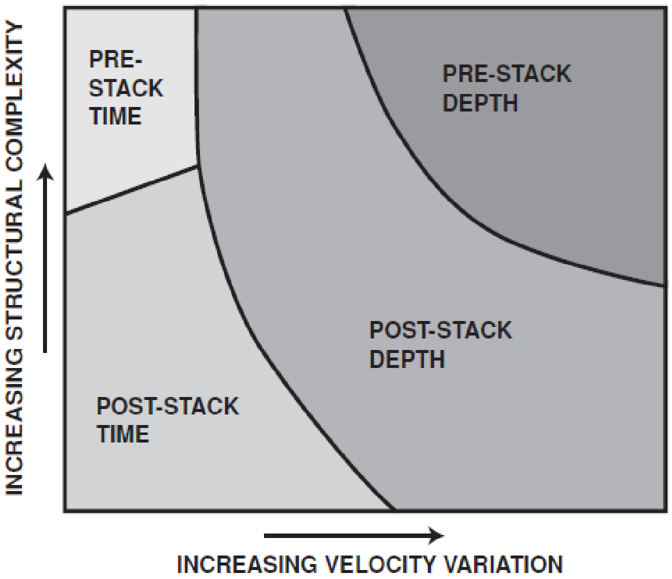

Fig. 2.5 Appropriate methods of migration as a function of structures and velocity variation (from Brown, 2010).

The 3D seismic data used in this research have been processed but not zero-phased, and no Automatic Gain Control (AGC) was applied. The polarity of the seismic data in this thesis can be described as 'SEG normal', according to the convention of the Society of Exploration Geophysicists (SEG; Bacon et al., 2007). SEG normal polarity often corresponds to a downward increase in acoustic impedance, displayed as a positive wavelet (Fig. 2.6; Bacon et al., 2007; Sheriff and Geldart, 1995). A reflection of SEG normal polarity begins with a downward deflection, often represented by a central peak for a zero-phase wavelet (Fig. 2.6a). For a minimum phase waveform, SEG normal polarity has a negative first break (Fig. 2.6b). However it is possible that sometimes the polarity may not correspond to the processors' convention due to the mistakes in seismic acquisition or processing (Bacon et al., 2007). To avoid this, the polarity of reflections can be confirmed by comparing the seismic data with well synthetics (Bacon et al., 2007). Since there is no well data in this study area, the polarity of the seabed is simply regarded as SEG normal, and the polarity of other reflections is recognized by comparing them with the seabed polarity.

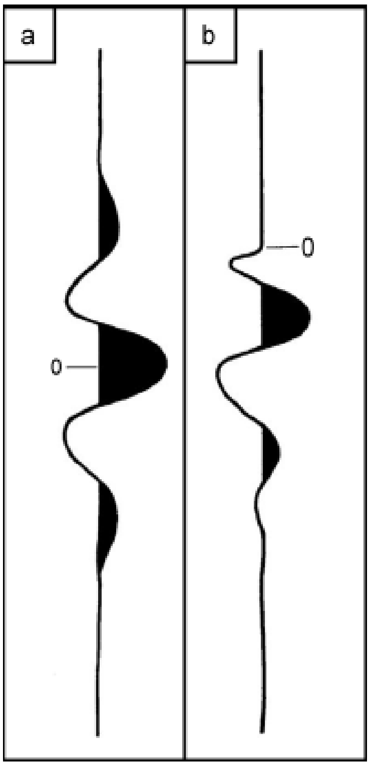

Fig. 2.6 SEG normal polarity standard. For a positive reflection (a): The centre of a positive symmetrical wavelet is a peak. (b): A minimum-phase wavelet begins with a down kick (from sheriff and Geldart, 1995; Ireland, 2011).

2.1.3 Resolution of seismic data

There is always a degree of uncertainty in 2D or 3D seismic interpretation because of the vertical and horizontal seismic resolution. One fundamental objective of the 3D seismic method is increasing resolution, both vertically and horizontally, which is also the aim of seismic processing (Fig. 2.7; Brown, 2010). The resolution of seismic data is always measured in terms of seismic wavelength (λ) which is determined by seismic velocity (v) and frequency (f):

$$\lambda = V / f \qquad \text{Eq. 2.3}$$

The vertical resolution of seismic data is given by:

$$\text{vertical resolution} = \lambda_0 / 4 \qquad \text{Eq. 2.4}$$

The horizontal resolution of seismic data is given by:

$$\text{horizontal resolution} = \lambda_0 / 2 \qquad \text{Eq. 2.5}$$

where λ_0 is the wavelength at the dominant frequency. In this thesis only the strata at shallower depth are investigated, less than 1000 ms below the seabed, which have low velocity. As a result, the seismic data for the investigated strata have high frequency content and thus have high resolution both vertically and horizontally.

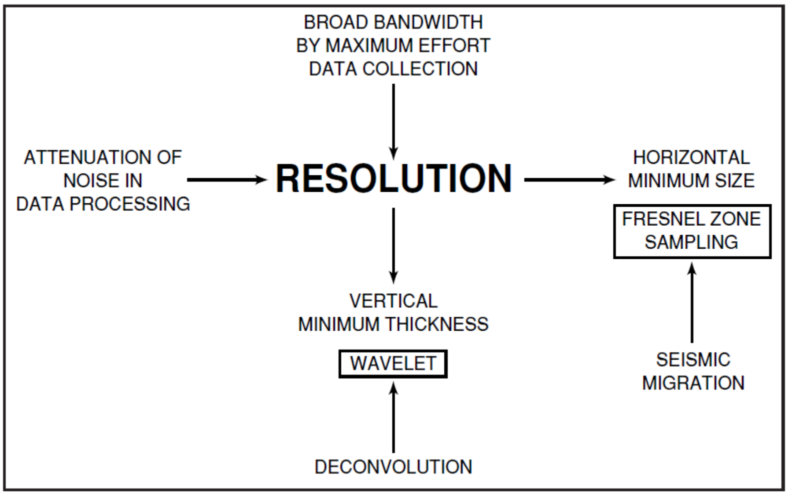

Fig. 2.7 Factors affecting horizontal and vertical seismic resolution (from Brown, 2010).

2.1.4 Interpretation of seismic data

2.1.4.1 Seismic interpretation

Seismic interpretation mainly involves tracing and correlating continuous reflections throughout the 2D or 3D seismic data to obtain a coherent geological story and understand the structural and stratigraphic characteristics at certain geological layers (Brown, 2010). Compared to 2D seismic surveys, 3D seismic data provide the following improvements in seismic interpretation: (a) sharper definition of structural features; (b) reliable correlation of horizons and fault traces between closely spaced tracks; (c) detailed time contour maps from time-slice sections; and (d) an improved velocity model for depth conversion (Brown, 2010).

The accuracy of seismic interpretation can be guaranteed by well ties to some degree because well data have the best source of stratigraphic information (Bacon et al., 2007; Brown, 2010). Stratigraphic horizons recognized from wells can be tied to related reflections on a seismic survey by constructing a synthetic seismogram, which is especially easier for a 3D seismic survey than a 2D survey because the 3D seismic data can show more accurate positioning of subsurface features (Bacon et al., 2007). There are three main steps to create a seismic seismogram (Fig. 2.8; Edwards, 1998; Bacon et al., 2007): (1) convert the well logs into logs in two-way travel time, using the sonic log; (2) multiply sonic log and density log together to produce an acoustic impedance log (Eq. 2.1) and calculate the reflection coefficient (Eq. 2.2); and (3) convolve the reflection coefficient with a chosen zero phase wavelet which represents the seismic data to produce a synthetic seismogram. The synthetic seismogram represents a modelled seismic trace at the well location, and is used to compare with the real seismic trace around the well location (Fig. 2.9; Bacon et al., 2007). A good match between the well synthetic and seismic dataset improves the accuracy and the resolution of seismic interpretation (Bacon et al., 2007). However this ignores the effect of anisotropy. Vertical seismic profile (VPS) data from wells can provide a more precise tie between well and seismic data (Bacon et al., 2007). This kind of data is recorded by shooting a surface seismic source into a borehole geophone. However no well data or VPS data is available in this studied area, so no well tie can be made in this thesis.

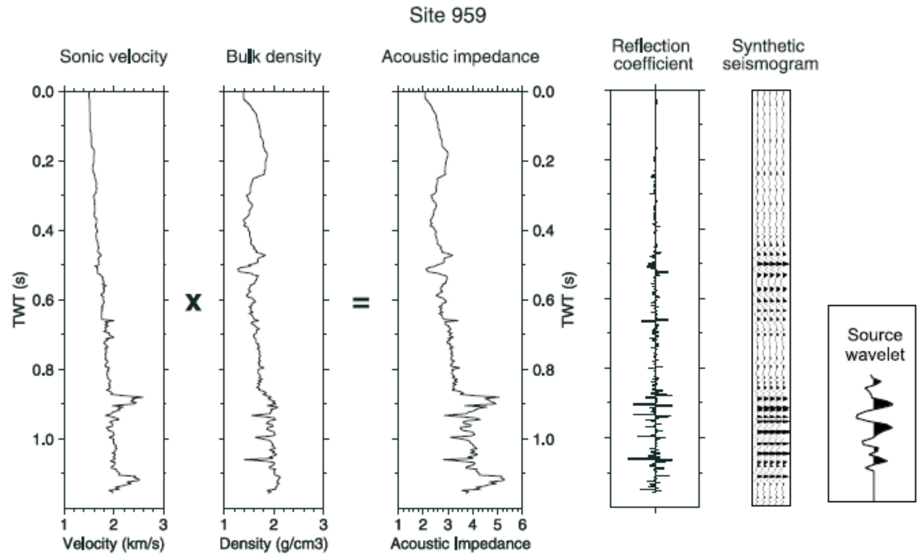

Fig. 2.8 Synthetic seismogram generation. Well logs are from Hole 959D (from Edwards, 1998).

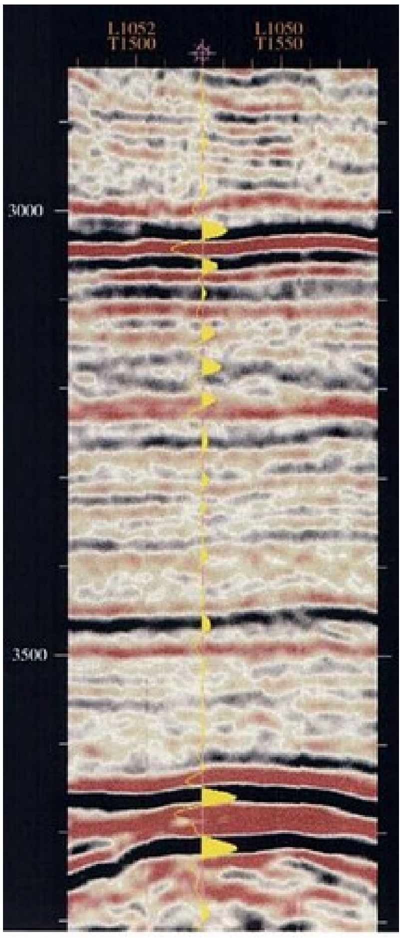

Fig. 2.9 A synthetic seismogram superposed on a seismic section at the well location (from Bacon et al., 2007).

Seismic interpretation includes stratigraphic interpretation, structural interpretation and reservoir identification (Brown, 2010). Stratigraphic interpretation is based on the principle that seismic reflections follow chronostratigraphic interfaces between beds (Emery et al., 1996). According to Mitchum and Vail (1977), seismic stratigraphic interpretation mainly involves recognition, correlation and age determination of seismic sequences with age often determined from well data, and seismic facies analysis which analyzes parameters like reflection configuration, amplitude, continuity, velocity and frequency to study the lithology, stratigraphic and depositional features of related sediments. Structural interpretation is also based on mapping seismic reflections, and structures can be best identified from 3D seismic data, especially from cross sections intersecting the structures and perpendicular to their strike directions (Bacon et al., 2007). Reservoir identification primarily indicates the recognition of direct hydrocarbon indicators (DHIs) on seismic data (Brown, 2010; Bacon et al., 2007).

The fundamental activity of seismic interpretation is making maps of seismic reflections (Bacon et al., 2007). However not all seismic reflections represent chronostratigraphic interfaces. For example, bottom simulating reflections (BSRs) interpreted from seismic data may represent diagenetic transformations (Isaacs, 1982) or phase boundaries between hydrates and free gas (Shipley et al., 1979). Both BSR types crosscut chronostratigraphic interfaces and mainly form under specific pressure and temperature conditions. Flat spots, which are hydrocarbon indicators, also crosscut adjacent seismic reflections due to the flat contacts between hydrocarbon and water (Brown, 2010).

2.1.4.2 Interpretation workflow in Landmark

In this thesis all the seismic interpretation has been done using Landmark OpenWorks, a Unix-based software package from Landmark Graphic Corporation which is widely used in oil and gas industry. The SeisWorks 3D software within OpenWorks is the industry standard for 3D seismic data analysis and interpretation. Landmark's next generation DecisionSpace Desktop is also used to do seismic interpretation, which is the surface interpretation software within OpenWorks.

Typical seismic interpretation workflow within Landmark SeisWorks or DecisionSpace Desktop is: (1) create a horizon file; (2) select a horizon and a tracking mode; (3) select an interpretation mode in seismic view; (4) select seismic sections to interpret; (5) interpret the horizon on intersecting lines; (5) perform auto-picking using interpreted horizon as 'seedpoints'; and (6) interpolation to fill in holes in the horizon. There are three tracking modes to search for the adjacent amplitudes along the selected horizon: (a) 'Auto Dip', the autotracking mode in which the tracker follows the dip you specify and amplitude is tracked based on the first and last traces selected by the user; (b) 'Auto Track', the autotracking mode where the tracker determines the dip and is generally used in good quality and consistent data to follow a well-defined, continuous horizon that may have variable dip; and (c) 'Point', the manual tracking mode where the user defines each point and is mainly used in poor quality and discontinuous data. After seismic interpretation, the generated horizons are known as 'time-structure' maps displaying the two-way-travel time (TWT) for the seismic waves to travel from the seabed to related horizons.

2.1.5 Seismic attributes

Using the Seismic Attribute Generation software and the 'time-structure' maps from seismic interpretation, a few types of attributes can be calculated such as amplitude, frequency, phase, relief, structural and miscellaneous attributes (Landmark, 2005). The amplitude, phase, and frequency attributes are 1D trace attributes computed down seismic traces. The structural attributes are 3D volume attributes computed across traces as well as down. Seismic attributes can be improved by deriving them on coherency filtered seismic data rather than on the original seismic data (Landmark, 2005). Most seismic attributes are largely independent of the polarity or phase of the original seismic data, although some are affected, for example phase attribute and relative acoustic impedance. Furthermore most seismic attributes are computed in an analysis window of adjustable size. The window size controls the resolution of the attribute: larger windows produce smoother attributes, which have lower resolution, and smaller windows produce less smooth attributes, which have higher resolution (Landmark, 2005).

The seismic attributes used in this thesis include amplitude and structural attributes. The amplitude attributes mainly include reflection strength, relative amplitude change, response amplitude and root-mean-square (RMS) amplitude, which reveal the magnitude of the seismic trace values or changes in these values. Structural attributes quantify elements of geological structure as recorded by seismic data, and mainly include azimuth, dip, discontinuity, and discontinuity along dip. In this thesis the reflection strength and RMS amplitude are mapped to generate related amplitude maps, providing information on hydrocarbon accumulations, focused fluid flow conduits, lithology and deformational structures (e.g. Brown, 2010). Dip maps and cross sections from the discontinuity-along-dip attribute volume are also used to study the structural features.

Understanding the colour principles can help an interpreter to maximize the use of colour, therefore selecting or modifying the correct colour bar is essential for analysing seismic data (Brown, 2010). The Colour Bar task pane allows people to view one or more colour bars and associated histograms applied to data, and it can be used in Map, Section and Cube views (Landmark, 2005). There are two fundamental colour schemes, contrasting and gradational. Cross sections or maps displayed in contrasting colour scheme are normally accompanied by a legend showing the range of values associated with different colours. The gradational colour scheme can be used to look for trends, shapes, patterns and continuity, and it is the most universally applicable colour scheme for interpreting seismic data (Brown, 2010). The seismic cross sections in this thesis are displayed with gradational black for positive amplitudes (peaks) and gradational red for negative amplitudes (troughs), which is called double-gradational black-white-red colour scheme.

2.2 3D seismic survey

The 3D seismic survey used in this thesis is located on the passive continental margin, ~ 100 km offshore Mauritania in NW Africa (Fig. 1.5). The 3D seismic dataset covers an area of ~ 4000 km^2, consisting of 3481 inlines and 5521 crosslines. They were processed by post-stack time-migration without being zero-phased, and no Automatic Gain Control (AGC) was applied. The main frequency of the 3D seismic data is 50 Hz, yielding a vertical resolution of approximately 8.5 m which equals one quarter of the wavelength at the dominant frequency assuming a sediment velocity of 1700 m s^{-1} (Davies and Clarke, 2010). The final bin spacing of the seismic grid is 25 m x 25 m. On seismic cross sections, a reflection event consisting of a red loop followed by a black loop represents an increase of acoustic impedance, known as a positive impedance contrast. This 3D seismic dataset requires no further processing before interpretation, and only seismic interpretation was carried out in this research.

Seismic cross sections are displayed in two-way-travel time (TWT) or depth (m) vertically, and horizontal axis (x, y) in metres (m) or kilometres (km). TWT can be converted into depth if accurate velocity information is available, using different algorithms according to specific cases. In this research the seismic data are in TWT vertically, but values of time can be converted into depth if needed. The time-to-depth conversion in this thesis is calculated using the following function, simply assuming the seismic wave path is vertical:

$$D = T\,V/2 \qquad \text{Eq. 2.6}$$

where D is the depth, T is the TWT and V is the assumed seismic velocity (Davies and Clarke, 2010).

A 2D seismic dataset is also available in this study area, but it does not help much in this research due to its limited resolution (see Appendix A). The frequency of the 2D seismic data is ~ 20 Hz, generating a vertical resolution of ~ 21.25 m. The 3D seismic data have a vertical resolution of ~ 8.5 m, suggesting that the 3D seismic data are far better in displaying the subsurface images than the 2D seismic data (Fig. 2.10). As a result only the 3D seismic data are displayed in the main parts of this thesis. See Appendix A for some 2D seismic lines and compare the plan-view TWT map of the seabed generated from the 2D seismic data with that from the 3D seismic data.

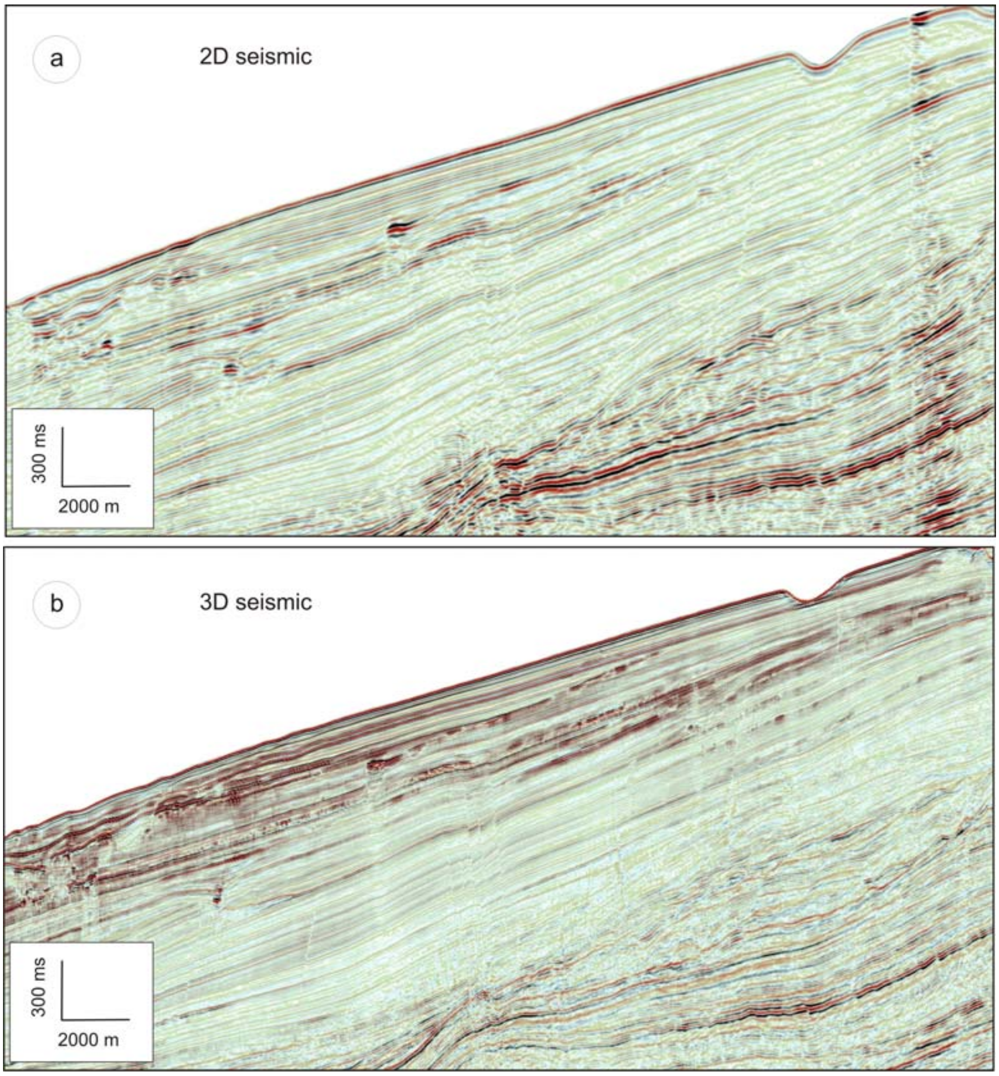

Fig. 2.10 Resolution comparison between 2D and 3D seismic. (a): A seismic line from the 2D seismic data offshore Mauritania. (b): The same seismic line from the 3D seismic data.

2.3 Well data

Data integration is important for accurate reservoir characterization which uses seismic, well log, and petro-physical information (Deshenenkov et al., 2011). To improve the accuracy of seismic interpretation, well-to-seismic ties are normally used to tie seismic back to a ground truth by comparing with well-log data using synthetics seismograms. The link between well data and seismic data is the wavelet, and an accurately determined wavelet is then used for forward seismic modelling (Linari, 2004). Unfortunately no well data is available in the study area for correlating with the 3D seismic data. But the scientific wells drilled at nearby places can be used to study the geological background. Vear (2005) comprehensively described the petroleum plays of the Mauritanian continental margin based on a considerable amount of well data, seismic data and other data due to the exploration and appraisal efforts to date. Tens of exploration wells were drilled on the Mauritanian continental margin as a result of the exploration activity (Vear, 2005).

The Ocean Drilling Program (ODP) data from the nearby area (Ruddiman et al., 1988) can also be used to study the regional geological background such as the sediment types and sedimentation rate (Fig. 1.4). The data used are from ODP Leg 108:

- Site 657 (21°19.89'N, 20°56.93'W; water depth, 4227 m; 1995) is located on the lower continental rise, 380 km west of Cap Blanc, which is outside the present-day influence of coastal upwelling. The sedimentation rates at Site 657 vary between 20 and 45 m m.y.$^{-1}$ in the Pliocene-Pleistocene and between 2.5 and 7 m m.y.$^{-1}$ in the Miocene.

- Site 658 (20°44.95'N, 18°34.85'W; water depth, 2263 m; 1986) was drilled on the continental slope 160 km west of Cap Blanc, underneath a major coastal upwelling cell. Organic carbon contents reach values of up to 4%. Mean sedimentation rates vary between 72 and 147 m m.y.$^{-1}$.

- Site 659 (18°04.63'N, 21°01.57'W; water depth, 3070 m; 1986) is located on top of the smooth Cape Verde Plateau, northeast of the Cape Verde Islands. Sedimentation rates vary between 4 m m.y.$^{-1}$ (Miocene) and 30 m m.y.$^{-1}$ (Pliocene-Pleistocene).

Further drilling information is available from offshore Mauritania at: http://www.odplegacy.org/ (accessed 10/04/2013).

Additionally ODP data from Leg 164 displayed three deep holes on a 10-km-long transect with water depth ranging from 2770 to 2798 m (Sites 994, 995, 997; Borowski, 2004). Leg 164 is about ‘Gas Hydrate Sampling on the Blake Ridge and Carolina Rise’, and the three sites penetrate below the base of gas hydrate stability zone within the same stratigraphic interval. These three sites are referred in this thesis to show that gas hydrates may exist even where there is no clear BSR (chapter 1):

- Hole 994 A: 31°47.141'N, 75°32.751'W; water depth, 2797.6 m; 1995.

  Hole 994 B: 31°47.139'N, 75°32.740'W; water depth, 2797.6 m; 1995.

  Hole 994 C: 31°47.139'N, 75°32.753'W; water depth, 2799.1 m; 1995.

  Hole 994 D: 31°47.142'N, 75°32.750'W; water depth, 2799.1 m; 1995.

  Site 994 is located on the southern flank of the Blake Ridge. No BSR is observed under Site 994, although there were gas hydrates recovered.

- Hole 995 A: 31°48.210'N, 75°31.343'W; water depth, 2778.5 m; 1995.

  Hole 995 B: 31°48.217'N, 75°31.336'W; water depth, 2776.9 m; 1995.

  Site 995 is located on the southern flank of the Blake Ridge within the same stratigraphic interval as Site 994. A modest BSR is present at Site 995 at ~ 530 ms sub-bottom. Comparison of Sites 994 and 995 can help understand the nature of BSRs and their controls.

- Hole 997 A: 31°50.588'N, 75°28.118'W; water depth, 2770.1 m; 1995.

  Hole 997 B: 31°50.598'N, 75°28.110'W; water depth, 2770.1 m; 1995.

  Site 997 is located on the crest of the Blake Ridge, penetrating a strong BSR which represents the base of gas hydrate stability zone. Comparison of the three sites 994, 995 and 997 can help establish lateral variations in the gas hydrate distribution and refine our understanding of the lateral development of BSRs within similar sedimentary sequences.

Further drilling information on Leg 164 is available at (accessed 10/07/2013):

http://www-odp.tamu.edu/publications/164_IR/164TOC.HTM

Chapter 3: Gas migration below gas hydrates controlled by mass transport complexes, offshore Mauritania

Abstract

Interpretation of 3D seismic data from offshore Mauritania reveals many localized high amplitude anomalies (HAAs) above some mass transport complexes (MTCs). These HAAs are located at ~ 500-900 ms below the seabed and have circular or elongate shapes in map view. The reflections at the tops of these HAAs are of negative polarity. We divide these HAAs into two populations, aligned and non-aligned. The aligned HAAs comprise three linear groups above the structural lineaments of underlying MTCs, suggesting a genetic link. The aligned HAAs in the western group are often located in depressions, and are interpreted to be caused by both gas migration and coarser-grained sediments. The other two groups of aligned HAAs are interpreted to be caused by residual gas after gas migration fed along the margins of underlying MTCs. In contrast, the non-aligned HAAs are generally smaller, located above the MTC bodies. They are interpreted to be caused by gas which migrated from underlying MTC bodies rather than along the margins, without any evidence for lithology change. We propose that the locations of the HAAs, both aligned and non-aligned, indicate gas migration pathways up MTC margins or local faults associated with the underlying MTCs. One possible gas source could be from hydrate dissociation due to the upward resetting of the base of gas hydrates. Since buried MTCs and gas hydrates can coexist in marine environments, the model of buried MTCs channelling fluids upwards may occur widely which can supply gas to the hydrate systems.

3.1 Introduction

Gas hydrates, together with associated free gas sealed by hydrates, may represent a large capacitor of hydrocarbon gases within the global carbon cycle (e.g. Shipley et al., 1979; Dickens, 2001). Fluids can migrate below hydrates by diffusion and focused flow, with the latter being much easier to detect on seismic data and common in fine-grained sediments (e.g. Abrams, 1992; Gay et al., 2007). Faults are often thought to be fundamental pathways for focused fluid migration (e.g. Ingram et al., 2004). Other pathways include chimneys and intrusions (sand, mud, salt or igneous), as they represent or create conduits of higher permeability than surrounding sediments (Abrams, 1992; Berndt, 2005; Cartwright et al., 2007; Gay et al., 2007). In gas hydrate systems, free gas is often regarded to be located below the base of gas hydrates (Shipley et al., 1979; Haacke et al., 2007). However Liu and Flemings (2006) showed that free gas can vent through the gas hydrate stability zone (GHSZ) because of the elevated salinity of the pore water as a result of hydrate formation. Additionally an overpressured free gas zone (FGZ) may cause fault reactivation and allow gas to escape through the GHSZ (Hornbach et al., 2004).

Submarine mass transport complexes (MTCs) are a widespread geological phenomenon that may affect the evolution of continental margins (Hampton et al., 1996; Bünz et al., 2005). On seismic data MTCs are mainly characterized by a chaotic seismic facies that represents the failed mass, an upper bounding surface and an underlying basal failure surface (Lewis, 1971; Woodcock, 1979; Bünz et al., 2005; Bull et al., 2009). According to Orange and Breen (1992), fluid migration may cause MTCs when its seepage force can offset gravity and friction, and it is widely proposed that hydrate dissociation is one of the triggering mechanisms of slope instability due to the large volume of gas and water it releases (Carpenter, 1981; Foland et al., 1999; Sultan et al., 2004ab). However, the opposite scenario that MTCs control the process of gas migration has seldom been described before and is poorly understood.

Despite the importance of gas hydrates as a potential source of energy, possibly with a role in climate change and carbon cycle, the specific mechanisms of gas supply for hydrate formation are poorly defined (e.g. Haacke et al., 2007). Previous papers show that biogenic gas generated from in situ organic-rich sediments can be used to form hydrates

(Rice and Claypool, 1981; Vandré et al., 2007; Garziglia et al., 2008). Hyndman and Davis (1992) proposed a model for the formation of hydrates and bottom simulating reflection (BSR) through the removal of gas from upward moving pore fluids as they pass into the gas hydrate stability zone (GHSZ). The gas can be either dissolved gas from pore fluids or disseminated free gas carried upwards by pore fluids. Davies and Clarke (2010) interpreted chimneys as the gas migration pathways into the hydrate system. Yang and Davies (2013) recently proposed that faults caused by creep processes on passive continental margins could act as gas migration pathways after the upward resetting of the base of hydrates. In this chapter we consider the role of MTC systems and specifically the significance of their margins as a fundamental control on gas migration beneath the hydrates.

3.2 Seismic indicators of gas migration

Subsurface fluid migration on continental margins has also been the subject of many studies. Many indicators of fluid migration have been identified on seismic data, such as pockmarks on the seabed (Hovland and Judd, 1988), vertical chimneys (Gay et al., 2006), and amplitude anomalies located along structures such as channels and faults (Davies, 2003; Ligtenberg, 2005; Gay et al., 2006).

On seismic data, chimneys are characterized by vertically aligned reflection terminations which can extend for hundreds of metres, and pull-up or push-down features in the chimney conduits due to velocity effects caused by high or low velocity materials such as hydrates, carbonates or free gas (Cartwright, 2007; Plaza-Faverola et al., 2011). When the chimneys reach the seabed, morphological features like pockmarks (Hovland and Judd, 1988), mud or sand volcanos (Cartwright et al., 2007), or chemosynthetic communities (Roberts et al., 2000) may form. In addition to those direct indicators, some localized amplitude anomalies associated with deformational structures such as faults and channels are also indicative of fluid migration pathways (Abrams, 1992; Davies, 2003; Ligtenberg, 2005). These amplitude anomalies may be caused by the presence of gas or gas-related diagenetic carbonates and the tops may be marked by negative or positive polarity reflection events respectively, due to their different acoustic impedances (Hovland et al., 1987; Roberts et al., 2000; Ligtenberg, 2005).

3.3 Geological setting

The study area is located on the West African passive continental margin, and the succession is characterized by canyons, MTCs and hemipelagic deposition (Figs 3.1 and 3.2; Vear, 2005; Krastel et al., 2006). The continental margin offshore Mauritania has a relatively narrow shelf, only 30-40 km wide, and a moderately broad continental rise (Antobreh and Krastel, 2007). The opening of the North Atlantic Ocean during the Mid-Jurassic is believed to have been initiated by seafloor spreading outboard of the Mauritanian Basin (Vear, 2005; Antobreh and Krastel, 2007). The present continental slope is generally smooth, and the angle of the dip is ~ 1-3° (Henrich et al., 2008).

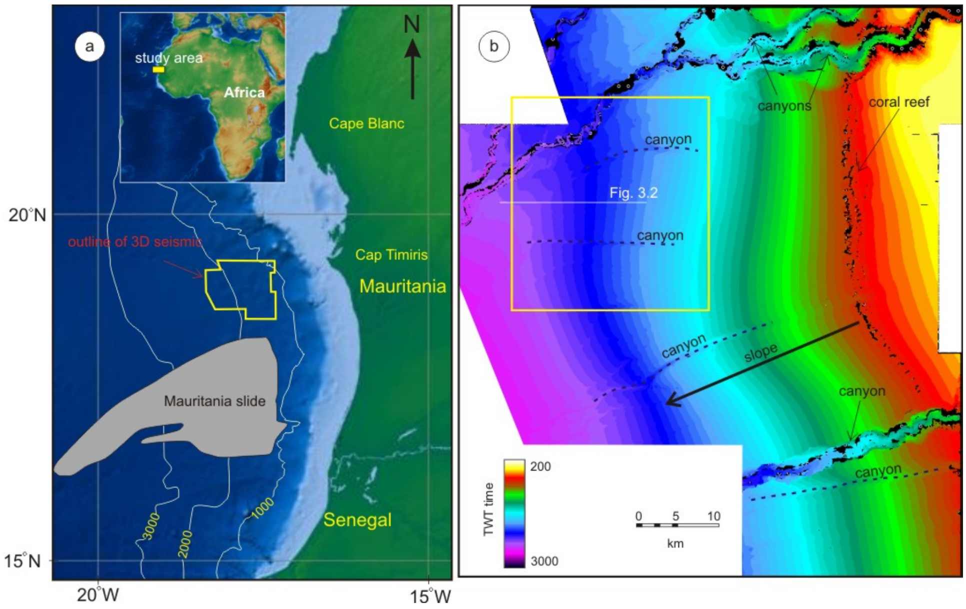

Fig. 3.1 (a): Location map showing the outline of the 3D seismic data and the Mauritania Slide (after Krastel et al., 2006). The bathymetry is contoured in metres. Inset: the position of Mauritania on the West African margin. (b): TWT map of the seabed from the 3D seismic survey, showing the position of the canyons and coral reef. The yellow box shows the location of the maps in figures 3.4, 3.5, and 3.10.

The continental margin is a potential petroleum province with the Miocene turbidite channels being the potential reservoirs, sealed by fine-grained channel abandonment facies or a hemipelagic shale drape (Vear, 2005). Possible source rocks include deep-marine mudstones deposited during the Cenomanian-Turonian, as well as other intervals such as the Albian and the Palaeocene (Vear, 2005). Although the Neogene is thin along most of the

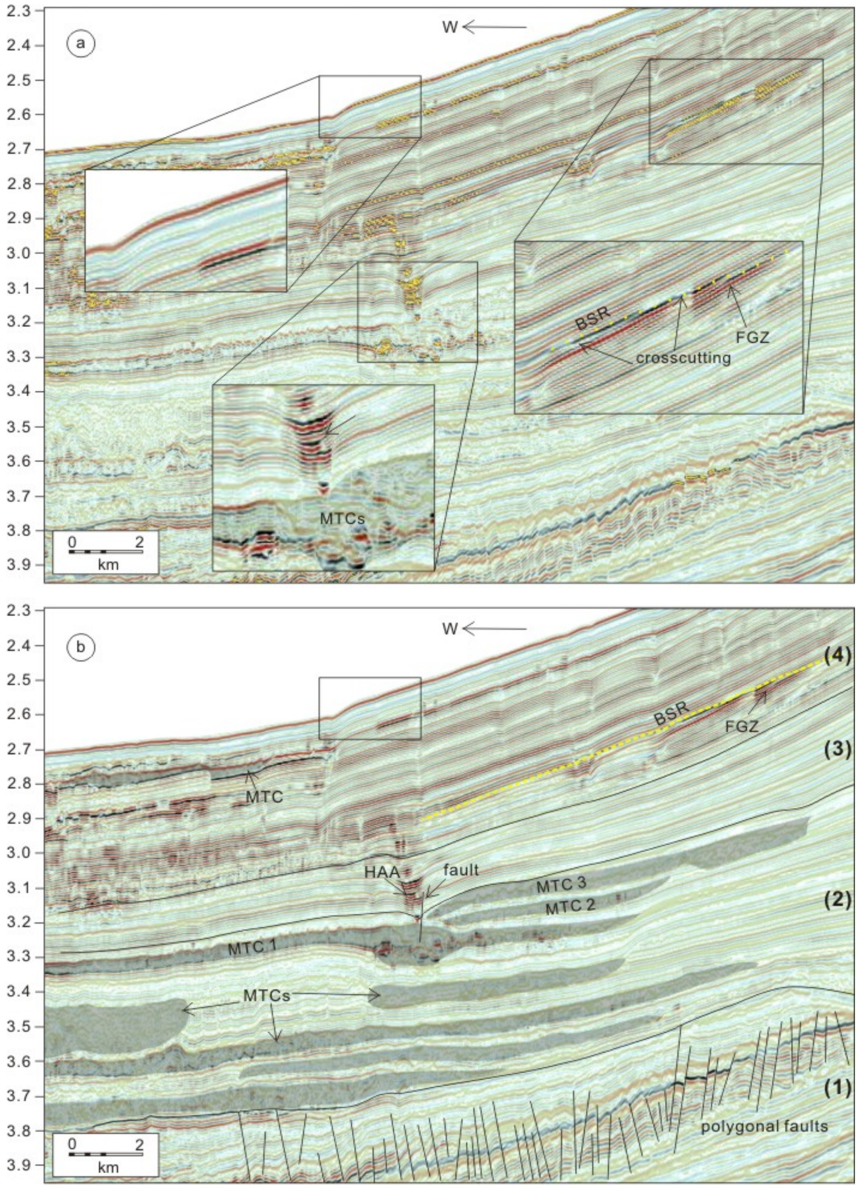

Fig. 3.2 (a): A seismic section (crossline: 25072) showing the general structural units and the HAAs. High reflection strength is indicated by yellow colour, suggesting a high contrast in acoustic impedance. The insets show details of projected sections. (b): Interpreted section showing MTCs, high amplitude depressions, BSR and FGZ. The vertical axis is TWT in seconds. See figure 3.1 for location.

West African margin, it is comparatively thick in Mauritania (Vear, 2005). There are a number of MTCs developed within the Neogene succession, probably formed due to the high sedimentation rates in a slope environment (Henrich et al., 2008; Antobreh and Krastel, 2007). For example, the Mauritania Slide complex is among the largest MTCs on the Northwest African continental margin, ~ 34,000 km^2, characterized by retrogressive sliding

(Fig. 3.1a; Krastel et al., 2006). Although the MTCs we report in this chapter are located to the north of the Mauritania Slide complex, they have similar features like retrogressive sliding and all formed during the Neogene (Vear, 2005; Ireland, 2011).

The interval we investigate is ~ 500 ms, with its base at ~900 ms below the seabed. Sediments in this succession are primarily characterized by fine-grained turbidites, debris flows and hemipelagic sediments, most of which are reworked aeolian sediments from the Sahara Desert (Vear, 2005; Krastel et al., 2006). For the studied interval, the sedimentation rate was high at ~ 80–160 m m.y.$^{-1}$, probably due to an ocean margin upwelling regime (Krastel et al., 2006; Henrich et al., 2008).

3.4 Seismic data and methodology

The 3D seismic dataset covers an area of ~ 4000 km^2, with water depth ranging from ~ 500 m to 2500 m. The seismic data have been processed by post-stack time migration and have a bin spacing of 25 m x 25 m. The processed seismic data have not been zero-phased, and no Automatic Gain Control (AGC) was applied.

On seismic sections a reflection event consisting of a red loop followed by a black loop indicates an increase in acoustic impedance downwards, representing a positive impedance contrast. A phase change can be recognized on seismic data as polarity reversal, with positive amplitude reflection becoming negative or vice versa. The dominant frequency of the 3D seismic data is ~ 50 Hz and the vertical resolution is ~ 8.5 m, calculated as one quarter of the wavelength at the dominant frequency and we assume a sediment velocity of 1700 m s^{-1} (Davies and Clarke, 2010). The vertical axis is in two-way-travel time (TWT) which can be converted to metres by assuming a seawater velocity of 1450 m s^{-1} and a sediment velocity of 1700 m s^{-1} (Davies and Clarke, 2010; Davies et al., 2012b). Distances and areas in map view can be measured in the seismic interpretation software.

To study the localized HAAs, we interpreted several representative reflections in this area and generated some seismic attribute maps based on the seismic interpretation. Apparent dip maps highlight structural features, and amplitude maps are useful for identifying amplitude anomalies which may be indicative of changes in lithology or pore fluid (e.g. Brown, 2010). We created a 3D discontinuity-along-dip volume to show the discontinuity attribute of the seismic data. Like standard discontinuity, discontinuity-along-dip values can highlight faults, channels, diapirs, and other seismic discontinuities (Hale, 2009). In this chapter, we examine cross-sections from the discontinuity-along-dip volume (discdip sections) to aid interpretation of selected seismic sections. See Appendix B for supporting figures.

3.5 Results

A representative regional seismic section shows ~ 1.6 s TWT below the seabed, displaying the amplitude and structural features in this area (Fig. 3.2). No age calibration can be made to the reflections due to the absence of well logs or other additional data, but according to previous studies the polygonal faults and MTCs lie within the Neogene strata (Vear, 2005; Antobreh and Krastel, 2007; Ireland, 2011). The entire studied interval is characterised by low amplitude continuous reflections which are interpreted to be hemipelagic sediments. Based on the characteristics of the seismic facies, the studied interval can be subdivided into several units based on the characteristics of the seismic facies. From bottom to top they are (Fig. 3.2):

(1) A polygonal fault system: located at ~ 1100 ms below the seabed, confined in an interval of ~ 300 ms. The faults are layer-bound normal faults with dips of ~ 40°, and they show varying fault patterns and dip distributions (Ireland, 2011).

(2) MTCs: several packages of discontinuous reflections in an interval of ~ 500 ms TWT. They are coincident with a period of overall increased mass wasting activity on the continental margin offshore Mauritania, which is thought to have been caused by the late glacial and post-glacial sea level rise (Henrich et al., 2008). Only the three MTCs at the shallower depth are studied which lie below some localized HAAs.

(3) Localized HAAs: vertically stacked above some MTCs in an interval of ~ 100 ms. These localized HAAs will be investigated in this chapter to understand their formation mechanisms and the role of underlying MTCs in the HAA formation.

(4) The gas hydrate system: indicated by the BSR and an underlying FGZ. A previous paper (Yang and Davies, 2013; chapter 4) described the gravity-driven faults below the BSR as recycling routes for the released gas from hydrate dissociation.

To study these localized HAAs above the MTCs, four representative reflections have been traced in the study area. They are termed TS, NA, MA, and TA from bottom to top (Fig. 3.3). Reflection TS is the top surface of the MTCs. NA is a reflection between TS and MA, interpreted for mapping the non-aligned HAAs. MA is a reflection in the middle of the HAA interval and TA is the top of the HAA interval. We also traced several reflections locally (reflections 1-3 and 1’-3’) to study related thickness changes. Next we will describe the MTCs and then the HAAs.

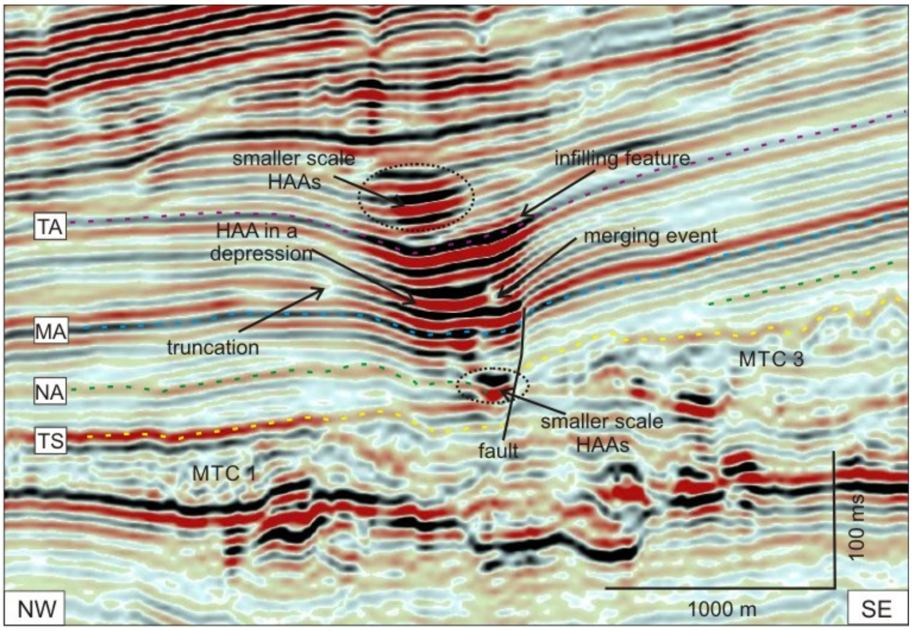

Fig. 3.3 A seismic section showing one HAA in the western group above the intersection point of three MTCs. The HAA is located in a depression, and we observe a local fault on the updip side at the bottom of the depression. See figure 3.4 for location.

3.5.1 Mass transport complexes (MTCs)

From 3.1 to 3.4 seconds (TWT) on cross sections there are three MTCs which have discontinuous chaotic internal structures and low reflection strength, separated by continuous reflections (Figs 3.2 and 3.4). The MTCs are bounded by upper and lower reflections which were called upper surface and basal failure surface in the following description. There are obvious upper surfaces for MTCs 1 and 3, which are of positive polarity and relatively continuous (Fig. 3.3). They were tracked as one reflection, TS (Fig. 3.3). On the upslope margin of MTC 3 the upper surface curves downwards towards its basal failure surface, truncating reflections and defining the upslope termination of this MTC (Fig. 3.4c). From bottom to top, the three MTCs stepped progressively updip, indicating a retrogressive failure style. Every MTC is wedge-shaped along its length between the two bounding surfaces (Figs 3.2 and 3.4c). Additionally on the upper slope there are two sub-vertical headwall scarps at different depths, without chaotic reflection nearby (Fig. 3.4c).

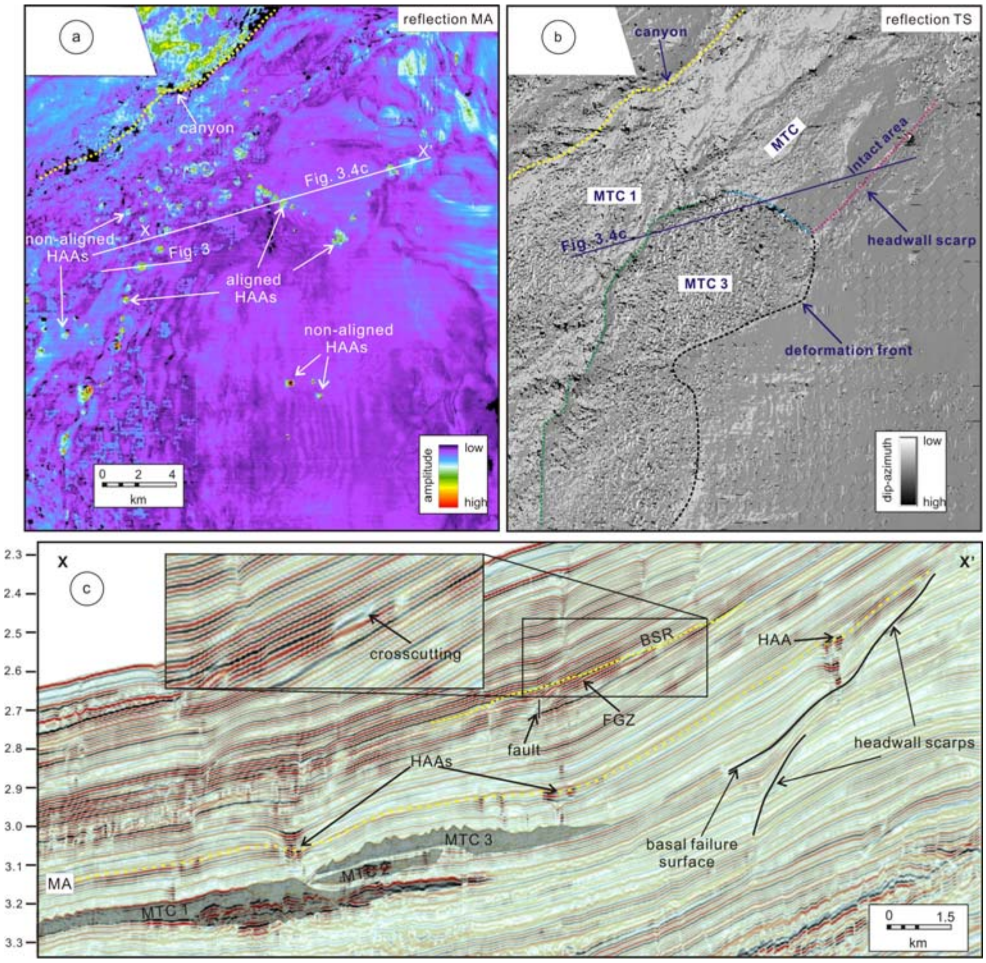

Fig. 3.4 (a): Amplitude map of reflection MA, showing the distribution of the HAAs and a canyon. (b): Apparent dip-azimuth map of reflection TS, showing the MTC distribution, related scarps and deformation front. (c): A seismic section through the three main groups of HAAs at reflection MA. The vertical axis is TWT in seconds.

On the apparent dip-azimuth map of reflection TS we measured the total areal extent of the MTCs, ~ 400 km^2, showing two MTCs in map view, 1 and 3 (Fig. 3.4b). The green line separating the two MTCs is spatially consistent with the MTC intersection on cross sections (Fig. 3.4). The blue line represents the upslope boundary of MTC 3 and the pink one shows the location of the shallower headwall scarp. On the apparent dip map we see that the chaotic MTC associated with the shallower headwall scarp is located ~ 1500-3000 m away, and the space in between has been infilled by post-slide deposits which give rise to coherent reflections (Fig. 3.4b).

3.5.2 High amplitude anomalies (HAAs)

On the amplitude map of reflection MA (Fig. 3.4a) there are many localized HAAs with variable sizes ranging from 0.05 to 0.8 km^2. They occur singularly, have circular or elongate shapes in map view, and most show evidence for spatial organization. Similar features can also be observed on the RMS amplitude extraction map generated within a window between reflections TA and TS (Fig. 3.5). We divide the HAAs into two populations, aligned and non-aligned. The aligned anomalies are subdivided into three linear arrays based on their spatial characteristics (Fig. 3.5): (1) the western group of circular HAAs; (2) the middle group of elongate HAAs; and (3) the eastern group of sub-circular HAAs. To study the aligned HAAs in detail, we mapped the thickness changes for the HAA interval across two rectangular areas (Fig. 3.5). Rectangle A covers four circular HAAs in the western group, and rectangle B contains all HAAs in the middle and eastern groups. The non-aligned anomalies are irregularly distributed in map view and do not have discernible spatial relationships with each other (Figs 3.4a and 3.5).

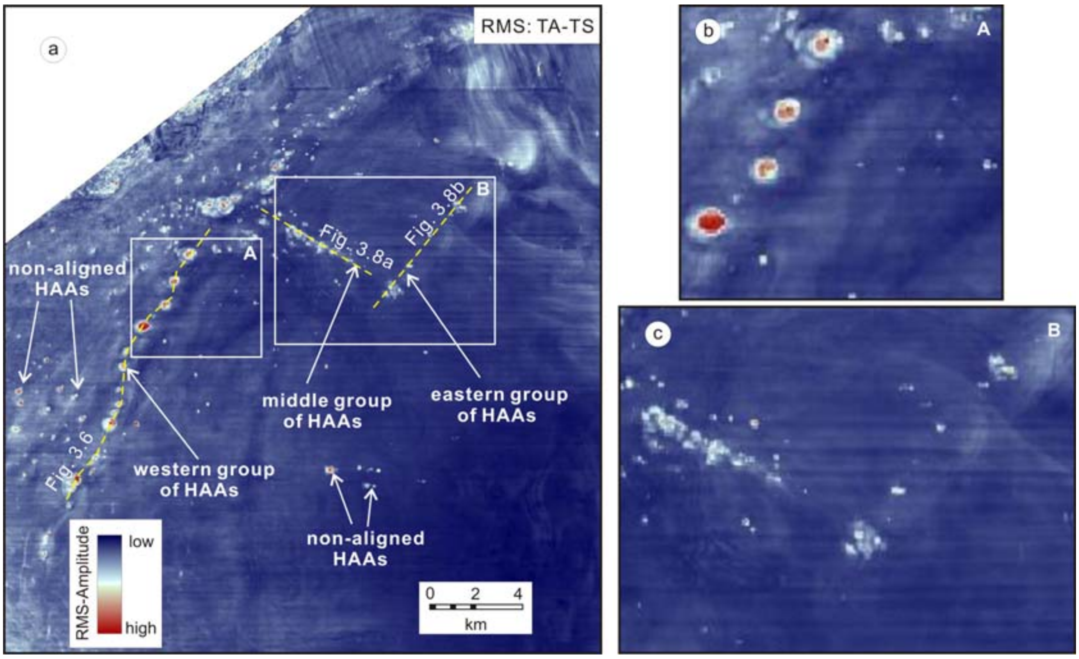

Fig. 3.5 (a): RMS amplitude extraction map generated within a window between reflections TA and TS, showing the distribution of the HAAs. (b, c): Zoom-in images of the two rectangles A and B.

3.5.2.1 Aligned HAAs

The HAAs in the western group have circular or sub-circular shapes in map view on the amplitude maps (Figs 3.4a and 3.5), with diameters of a few hundred metres. They are spaced ~2.5 km apart in a NE-SW alignment, above the lineament of MTC intersection. Seismic sections (Figs 3.2-3.4 and 3.6-3.7) show that these HAAs in the western group are located in depressions above the intersection line of three MTCs, ~ 100 ms. The polarity of these HAAs cannot be measured because the high amplitudes are not restricted to a single reflection. But the tops of these HAAs have comparatively negative polarity, opposite to the seabed and the upper surfaces of the MTCs. At the bottoms of these HAAs there are local normal faults with small throws of less than 10 ms, most on the updip sides of the depressions (Figs 3.3, 3.6 and 3.7). Most of the faults do not cut through the whole HAA intervals, but connect the bottoms of the HAA intervals with underlying MTCs. In the middle of most of the HAA intervals we observed reflection truncations on the downdip side, and on the updip side there are merging events with two red loops becoming one towards the middle of the depressions, possibly caused by faulting (Fig. 3.3). Above reflection TA, which is the top of the depressions where the amplitudes of the depressions are largest, there are some infilling features. Smaller-scale HAAs are observed within the infilled interval, some of which show negative polarity. Between the main HAA interval and the MTCs there are other smaller-scale HAAs whose tops are of negative polarity as well (Figs 3.3 and 3.6). To estimate the thickness change associated with the HAAs, we interpreted three local reflections in rectangle A (reflections 1-3) (Fig. 3.7a) which bound two units (the HAA interval, denoted as unit 1; the infilling layer above the HAAs, denoted as unit 2). At these four HAA locations, the isochron maps show a decreased interval for unit 1 and an increased interval for unit 2 (Fig. 3.7cd).

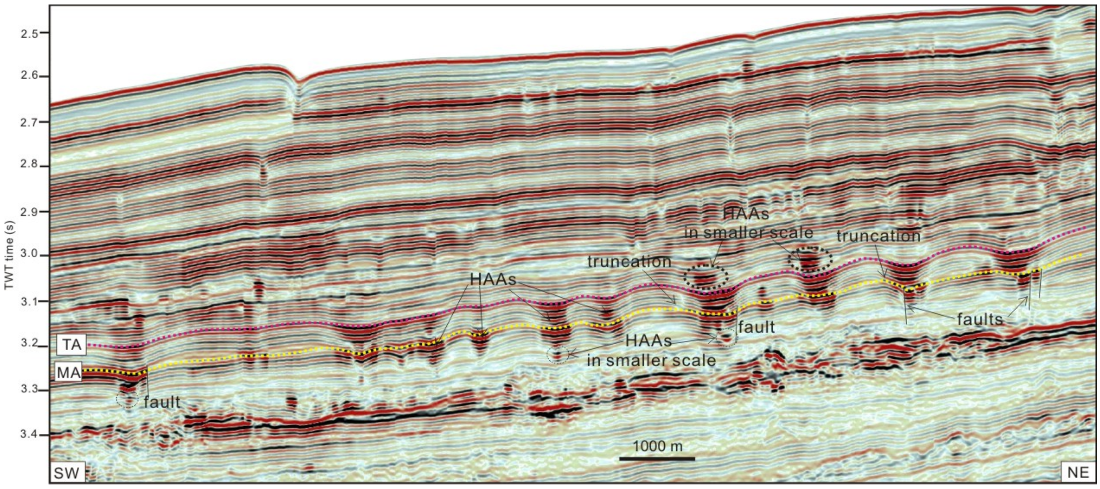

Fig. 3.6 A seismic section through the western group of HAAs, showing the high amplitudes in depressions, underlying MTCs and other features like smaller-scale HAAs and local faults. See figure 3.5 for location.

The HAAs in the middle group have elongate shapes with their long axes in the direction of the alignment of this group, NW-SE (Fig. 3.4a). The average length of their long axes is ~ 400 m. On seismic sections (Figs 3.4c, 3.8a and 3.9a), the HAAs in the middle group have negative polarity, opposite to the seabed and the upper surface of MTCs, and are located in a thin interval of ~ 50 ms above the head region of a single MTC. On a seismic section (Fig. 3.9a), the HAA terminates laterally and we do not observe obvious fault linking the HAAs to underlying MTCs. However the corresponding discdip section (Fig. 3.9b) shows vertical linear discontinuous features that link the HAAs to the underlying MTC. Below the main HAAs in the middle group there are smaller-scale HAAs and polarity reversal features (Fig. 3.8a). We interpreted another three local reflections in rectangle B (reflections 1’-3’) (Fig. 3.9ac) to study the thickness changes of unit 1’, a layer below the HAAs, and unit 2’, the

HAA interval, for the middle and eastern groups (Figs 3.8 and 3.9). The isochron maps show decreased interval for unit 1’ and increased interval for unit 2’ for both groups.

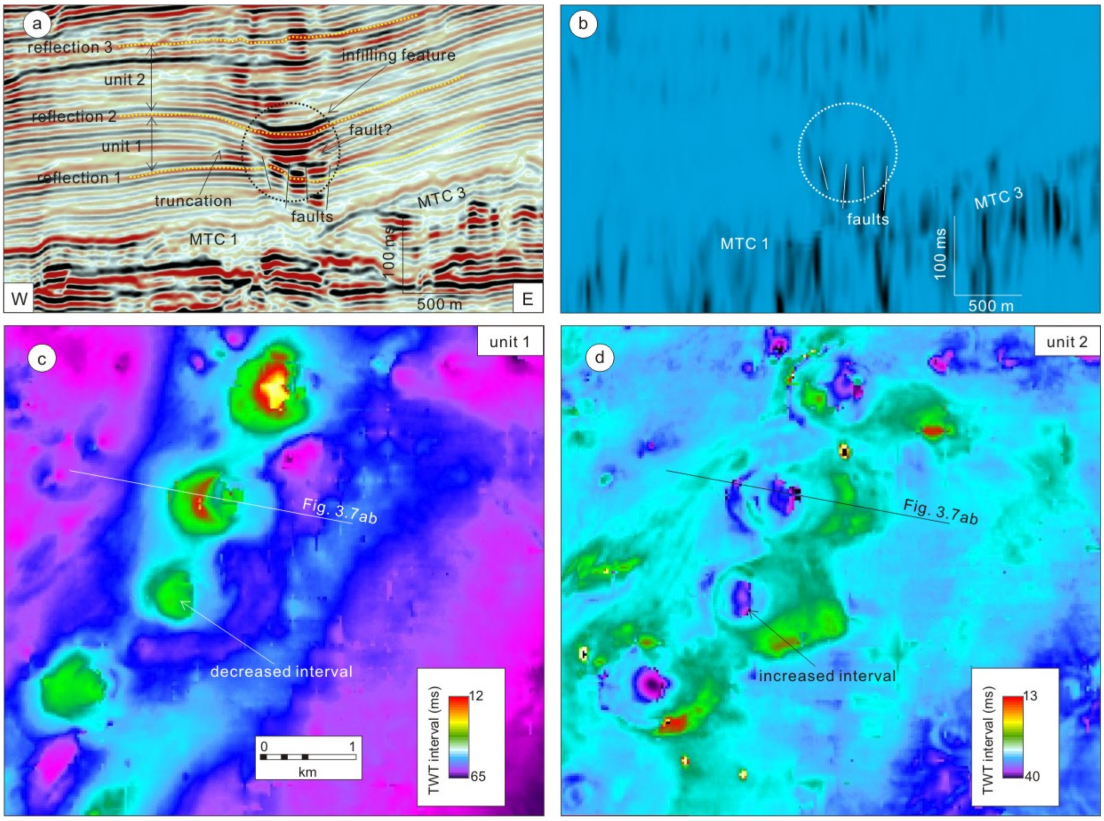

Fig. 3.7 (a): A seismic section through one anomaly in the western group of HAAs. (b): The corresponding discdip section showing the structural discontinuities. The circle shows the location of the HAA interval. (c): Isochron map of unit 1, showing decreased interval. (d): Isochron map of unit 2, showing increased interval . Location of this map is shown in figure 3.5, where it is termed rectangle A.

The HAAs in the eastern group are much more variable in size than the HAAs in the other two groups (Figs 3.4a and 3.5). There are four sub-circular anomalies, including the one at the intersection point with the middle group, located in an interval of ~ 40 ms. The diameters of these four HAAs are 0.85, 0.2, 0.25, and 0.5 km, and they are distributed along the headwall scarp of a MTC. The dip map of reflection TS (Fig. 3.4b) shows that the MTC body related to this headwall scarp is located ~ 1500-3000 m downslope, leaving an intact area in between. The HAAs are located on the downslope side of the headwall scarp, without any chaotic reflections nearby (Figs 3.4c and 3.9c). Below these HAAs there are some discrete small-scale HAAs with negative reflection coefficients, and some show polarity reversal features (Fig. 3.8b). For the HAA shown in figure 3.9c, we observe two local normal faults at the bottom of related smaller-scale HAA. The corresponding discdip section (Fig. 3.9d) shows that this HAA is not linked directly to the headwall scarp, but connected to the basal failure surface. The isochron maps (Fig. 3.9ef) show the same change as in the middle group, decreased interval in the lower unit and increased interval in the upper unit, with the main HAAs located in the upper unit. However there is interval decrease for both units to the east of the eastern group which is spatially consistent with the location of the headwall scarp.

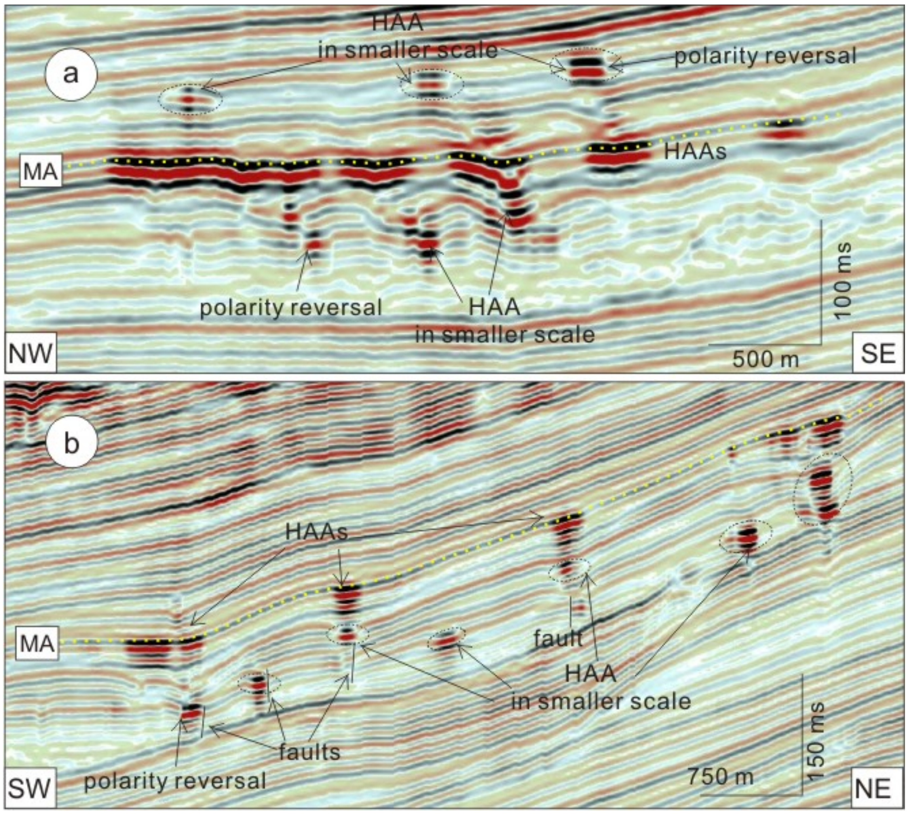

Fig. 3.8 Seismic sections through (a) the middle, and (b) the eastern groups of HAAs, showing the HAAs and underlying structures related to MTCs. See figure 3.5 for location.

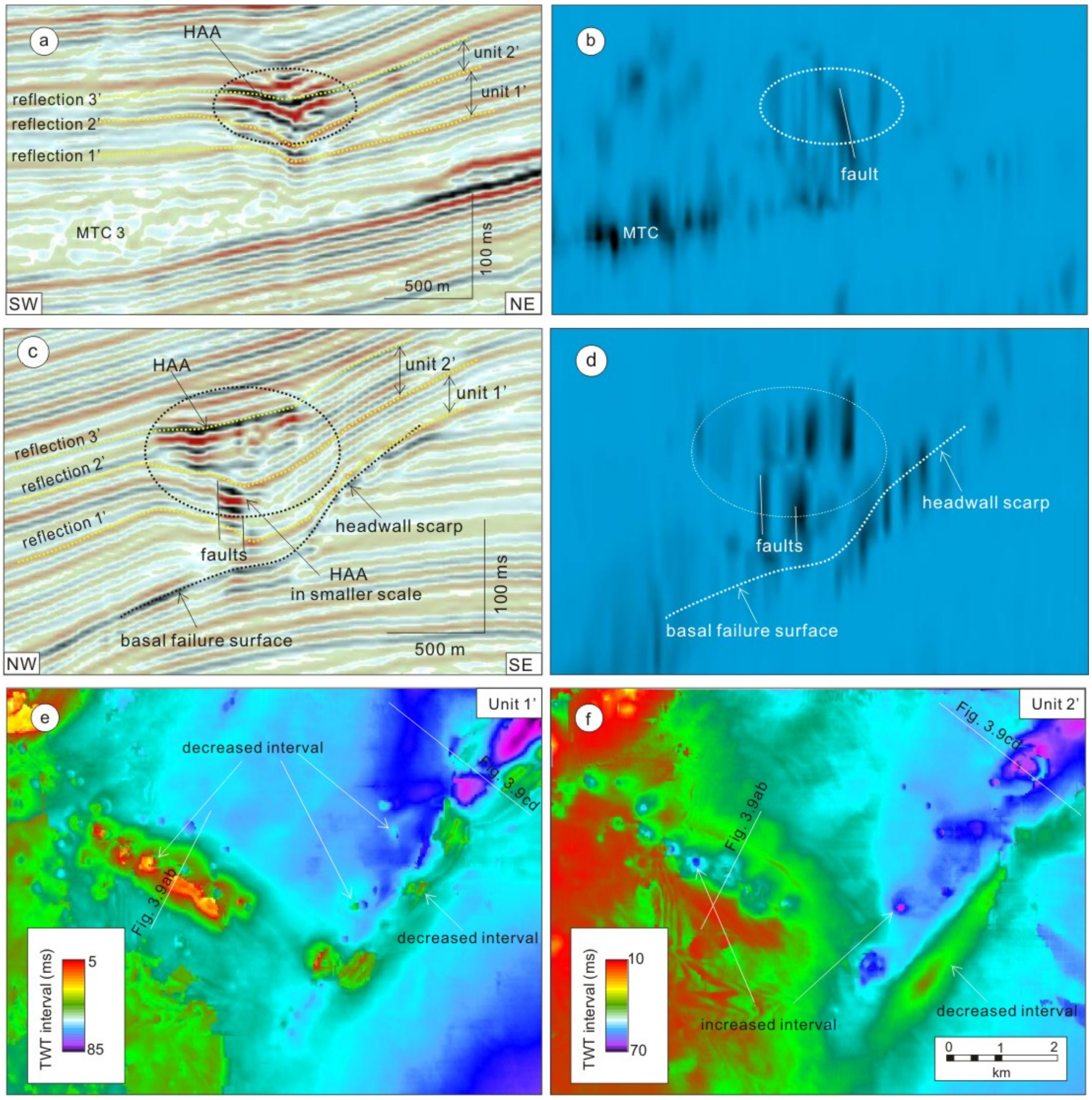

Fig. 3.9 (a): A seismic section through one anomaly in the middle group. (b): The corresponding discdip section of a, showing structural information. (c): A representative seismic section through one anomaly in the eastern group, showing the spatial relationship between the HAA and the headwall scarp. (d): The corresponding discdip section of c, showing the structural information. (e): Isochron map of unit 1', showing decreased interval along the middle and eastern groups. (f): Isochron map of unit 2', showing the increased interval along the middle and eastern groups. Location of these two maps is shown in figure 3.5, rectangle B.

3.5.2.2 Non-aligned HAAs

In addition to the aligned HAAs, there are some non-aligned HAAs shown on the amplitude maps (Figs 3.4a and 3.5). On the amplitude map of reflection NA, the non-aligned HAAs are much more densely developed than at reflection MA (Fig. 3.10). Comparison of the amplitude maps (Figs 3.4a and 3.10a) and the apparent dip-azimuth map of reflection TS (Fig. 3.4b) shows that most of the non-aligned HAAs are located above the MTC bodies. The non-aligned HAAs are mainly sub-circular in map view, and there are some elongate ones as well. Their average size is smaller than the aligned ones, ~ 0.05 km^2. Seismic sections show that these non-aligned HAAs have negative polarity, and the HAA intervals are ~ 35 ms (Fig. 3.10). On the updip sides of some of the non-aligned HAAs, we observe sub-vertical normal faults rooted at the tops of the MTCs. For other non-aligned HAAs, we do not observe obvious structures.

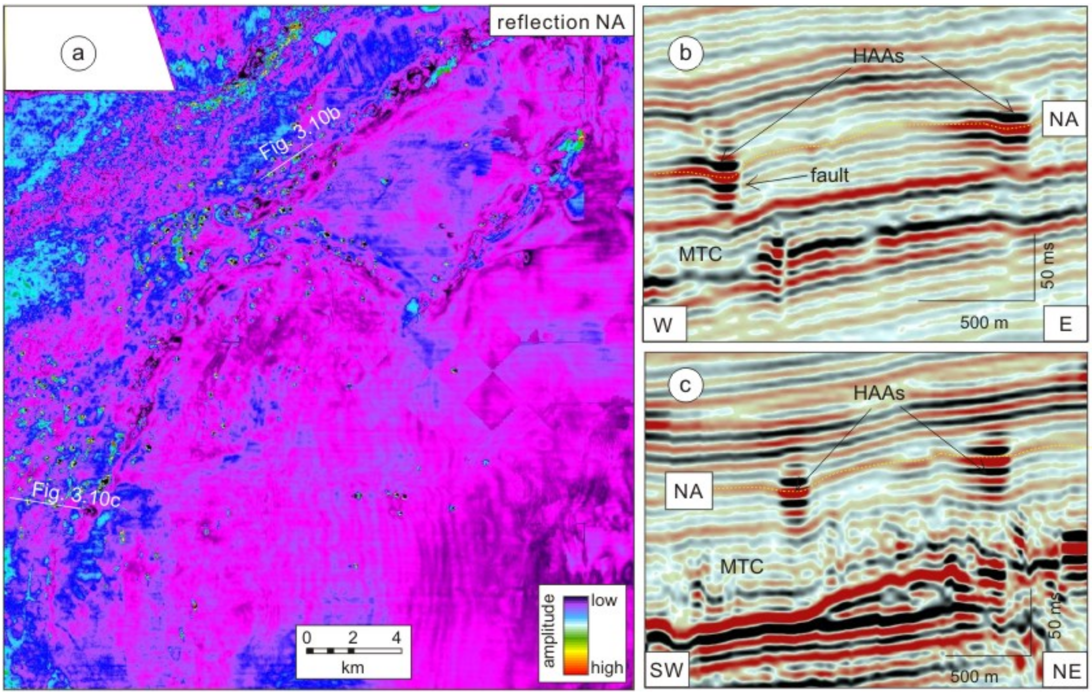

Fig. 3.10 (a): Amplitude map of reflection NA, showing the distribution of the non-aligned HAAs. (b, c): Seismic sections cutting through the non-aligned HAAs, which are located above the MTCs.

3.6 Formation mechanisms

3.6.1 Aligned HAAs

The aligned HAAs at reflection MA closely follow the structural lineaments of the MTCs, suggesting a genetic link. It has been widely presented that deformational structures of high permeability can act as fluid migration conduits, and case studies from offshore West Africa (Ligtenberg, 2005; Pilcher and Argent, 2007), Pearl River Mouth Basin (Sun et al., 2012), Faeroe-Shetland Basin (Davies et al., 2008) and Lower Congo Basin (Gay et al., 2007) have explained the roles of slump faults, normal faults, diapirism, chimneys and erosional unconformities as pathways for gas migration which was interpreted to be primarily responsible for the formation of HAAs. In addition to gas, there are other factors that can cause high amplitudes on seismic data such as tuning effect, lithological change, mineral precipitation, or hydrocarbon-related diagenetic zones (HRDZs; O'Brien and Woods, 1995; Ligtenberg, 2005; Brown, 2010).

Another interesting phenomenon is the shape of these HAAs. Previous studies show that the geometries of amplitude anomalies are variable from linear (e.g. along fault) to circular (e.g. at fault intersections), depending on the shapes of fluid leakage conduits (Davies, 2003; Ligtenberg, 2005). Here the western group of circular HAAs is located in buried pockmarks above the intersection of three MTCs; the elongate HAAs in the middle group are located along the local faults above the head region of a single MTC; the sub-circular HAAs in the eastern group are located on the downslope side of the headwall scarp of a single MTC; and the non-aligned HAAs in sub-circular or elongate shapes are located above MTC bodies, along small-scale faults or without obvious structures. So we propose that the shapes of these HAAs are probably controlled by related fluid migration structures.

3.6.1.1 Western group of HAAs

Circular depression trains have been observed widely on continental margins, for example in the Niger Delta (Davies, 2003), the Congo Basin (Gay et al., 2003), offshore Gabon (Pilcher and Argent, 2007), and the Espirito Santo Basin (Heiniö and Davies, 2009). These depressions were caused by fluid escape, bottom currents or turbidity currents, often related to faults, buried channels, diapirs, slumps, or other topographical irregularities. Normally depressions formed mainly by seafloor currents have a variable morphology that develop from asymmetric scour-shaped or horseshoe-shaped depressions upwards into more rounded and symmetric ones (Andresen, et al., 2008; Heiniö and Davies, 2009; Ho et al., 2012).

Here the circular HAAs in the western group are located in depressions above the intersection lineament of three MTCs, and there are local faults at the bottoms of the depressions linking the HAAs to the underlying MTCs (Figs 3.3, 3.6 and 3.7). These depressions are interpreted to be buried pockmarks on the palaeoseabed probably caused by upward fluid venting. Subsequently they started to be infilled at reflection TA. The localized faults at the bottoms of depressions are proposed to be probably caused by gravity collapse, down-warping into the depressions created by differential compaction of the unevenly deposited sediments lying immediately above the MTCs, and also possibly by the removal of sediments entrained in the expelled fluid (Davies, 2003). These faults may act as potential conduits, capable of channelling fluids upwards. The deeper and smaller-scale discrete HAAs are interpreted to be caused by gas, suggesting the route of upward fluid escape (Figs 3.3, 3.6 and 3.7). There are other smaller-scale HAAs above the main HAA interval (Figs 3.3 and 3.6) and they are interpreted to be caused by gas because of their negative polarity, possibly indicating another stage of gas migration after the pockmarks were buried. No additional data are available here to study the source of the gas such as geochemistry data, but a few factors are discussed to consider their roles in supplying gas to form these HAAs: (a) gas from greater depth, which may be inhibited here by the polygonally faulted layer below the MTCs because the layer of polygonal faults can act as a seal of low permeability when the polygonal faults are not active (Fig. 3.2; Cartwright and Lonergan, 1996; Cartwright and Dewhurst, 1998; Stuevold et al., 2003; Cartwright, 2007; Sun et al., 2012); (b) released gas from hydrate dissociation which would have occurred in this area due to the upward resetting of the base of the hydrates and this has been demonstrated by Davies et al. (2012a) who traced the relict bases of gas hydrates using their intersections with stratigraphic reflections; and (c) biogenic gas generated from the in situ organic-rich sediments in the MTCs (Rice and Claypool, 1981; Vandré et al., 2007; Garziglia et al., 2008). Based on the seismic study of the palaeo-BSRs in this area (Davies et al., 2012a) we propose that dissociated gas from hydrates may cause the formation of these HAAs, but we cannot rule out other sources of fluid due to the absence of additional data, such as in situ generation of biogenic gas, squeezed pore fluids from compaction or deep thermogenic gas.

The formation of pockmarks can be episodic or continuous, and both mechanisms may disperse sediments up into the water column and finer-grained sediments may be taken away by bottom currents (winnowing process; Hovland and Judd, 1988; Hovland et al., 2002; Pilcher and Argent, 2007). According to Hovland et al. (2002), the acoustically high reflections in pockmarks may be caused by coarser sediments remaining after winnowing process, by biological activity such as skeleton remains or dead shells, or by authigenic carbonate precipitation. Davies (2003) proposed that sand intrusion (injectite) may cause high amplitudes in depressions. Additionally, local topographic lows such as channels, faulting or venting-related seabed depressions are capable of capturing bottom currents, leading to the deposition of coarser sediments (Anderson et al., 2000; Ho et al., 2012). As a result, we propose that the HAAs in the western group which are located in depressions are probably caused by gas relict after upward gas migration as well as coarser sediments deposited by bottom currents or fluid venting-related winnowing process. We cannot determine which plays the main role in the HAA formation due to the lack of evidence. But coarser sediments deposited by bottom currents is also indirectly linked to fluid migration because the depressions where coarser sediments are prone to deposit were probably formed by fluid venting (Anderson et al., 2000). Additionally the presence of carbonates cannot be ruled out although the top of the HAAs are of negative polarity. Carbonates may occur in the central part of the depressions, and the HAAs may be controlled by a mixture of several factors (Hovland et al., 2002; Pilcher and Argent, 2007). The gas stored in these depressions does not migrate laterally to the updip because the gas is preferentially held in the coarser sediments in the pockmark column. The surrounding fine-grained sediments have lower permeability and higher capillary entry pressure which inhibits the lateral escape of gas (e.g. Sylta, 2005).

We suggest a model to explain the formation of the western HAA group (Fig. 3.11a). Stage 1 represents the formation of a pockmark above the intersection of MTCs, caused by fluid expulsion at the palaeo-seabed and removal of entrained fine-grained sediments by bottom currents. Coarser sediments in pockmarks may also form by bottom current deposition. Stage 2 is intended to represent a variant of Stage 1, and a local gravity fault may form on the updip side of the pockmark due to differential compaction of the unevenly deposited sediments lying immediately above the MTCs and even the removal of sediments entrained in the expelled fluid. Stage 3 shows sedimentary infilling of the pockmark probably by following reduction in the rate of fluid expulsion which was responsible for pockmark

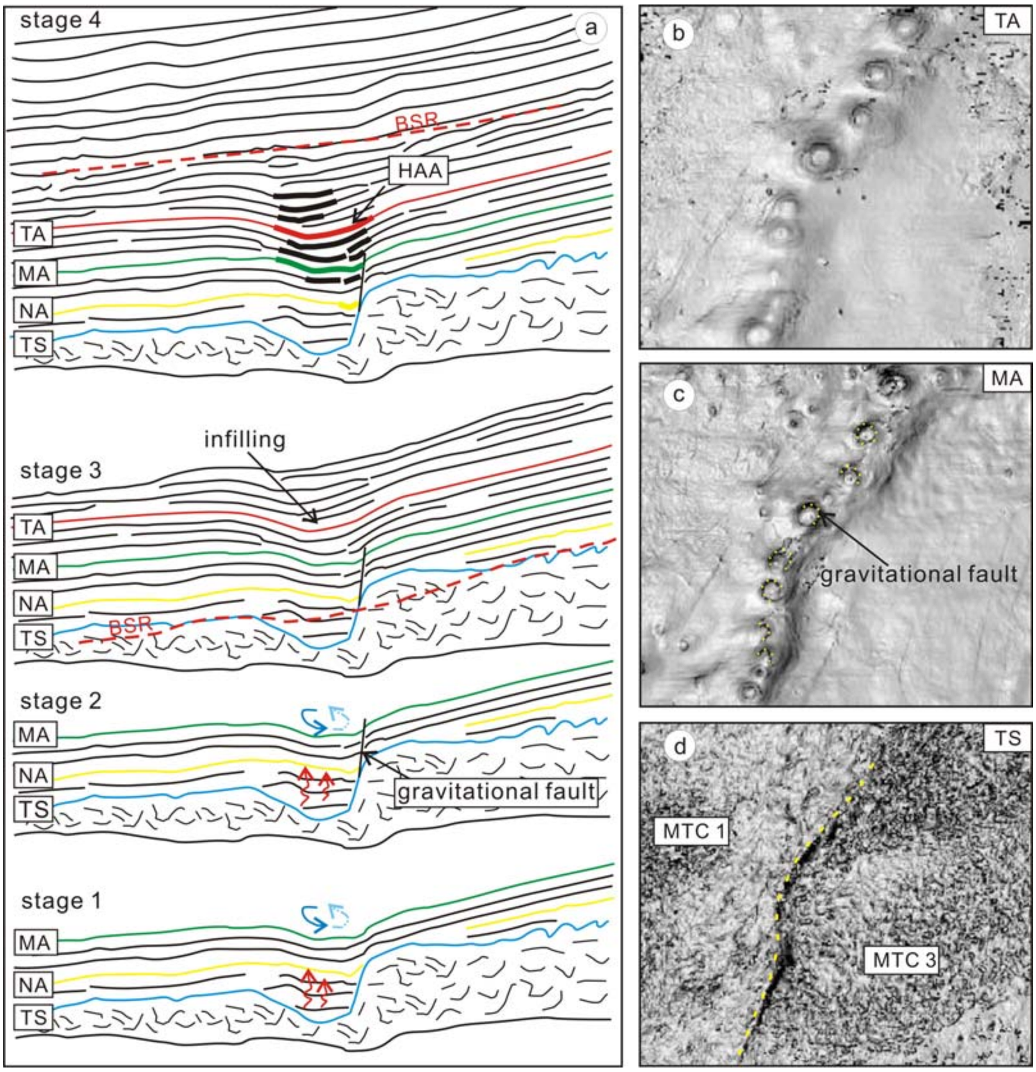

Fig. 3.11 (a): Model for the formation mechanism of the western group of aligned HAAs. The diagrams show four stages of the depression evolution. (b-d): Dip maps of reflections TA, MA, and TS, showing the structural features.

formation. Stage 4 represents a later fluid migration event, possibly triggered by hydrate dissociation due to the upward resetting of the base of gas hydrates, or other factors such as in situ biogenic gas, squeezed pore fluids from compaction or deep thermogenic gas. The fluid was transported upwards through the buried pockmark column and leaving relict gas pockets in the pore space on its way. As a result, the reflection amplitude in these buried pockmarks is higher than in the surrounding sediments because of the presence of gas (left from gas migration) and coarser sediments (deposited by bottom currents or by winnowing process).

3.6.1.2 Middle and eastern groups of HAAs

There is a close spatial relationship between the HAAs in the middle group and the upslope boundary of MTC 3 (Fig. 3.4). Due to their negative reflection polarity and nearby polarity reversal features, the HAAs in the middle group are interpreted to be caused by gas. The underlying discrete smaller-scale HAAs, which also have negative reflection polarity at the top, are interpreted to be relict gas accumulations left after upward fluid migration, suggesting the gas migration route. Although there is no obvious fault on the seismic section probably due to resolution limitation, the corresponding discdip (‘discontinuity along dip’ attribute) section shows a vertical linear discontinuous feature that links the HAAs to the underlying MTC which is interpreted to be a local fault (Fig. 3.9ab). Fluid may have migrated laterally along the basal failure surface to the updip because of the low-permeability of the MTC body and enhanced permeability of the basal failure surface (Bangs and Westbrook, 1991; Sultan, 2004a; Berndt et al., 2012). When the fluid arrived at the head region of the MTC where the permeable basal failure surface terminated, it migrated upwards along the local faults which have higher permeability than surrounding sediments. The locations of the smaller-scale HAAs support this hypothesis.

The HAAs in the eastern group are also interpreted to be caused by gas due to their negative polarity and nearby polarity reversal features, suggesting that there was fluid migration from below (Figs 3.8b and 3.9cd). In the offshore Eel River Basin pockmarks have been observed at the headwall scarp of a submarine slide, indicating the route of upward fluid expulsion (Foland et al., 1999). However the HAAs here are not along the headwall scarp but on its downslope side. Previous studies showed that pockmarks have been observed offset from the faults (e.g. slump faults, extensional faults) on the hanging wall sides (Ligtenberg, 2005; Pilcher and Argent, 2007; and referecnes therein). The reduction of the overburden pressure at the fault enables vertical leakage of fluid when the effective stress at the footwall cut-off reduces to zero because of overburden pressure decrease and pore pressure increase (Pilcher and Argent, 2007). That may also explain the location of the gas migration here indicated by the HAAs of the eastern group, in the hanging wall of the MTC-related fault (the headwall scarp).

3.6.2 Non-aligned HAAs

The non-aligned HAAs are interpreted to be caused by gas due to the strength of the reflections and the negative reflection polarity at the top of each HAA. Most of the non-aligned HAAs are located above MTC bodies and some occur along small-scale faults observed on seismic data. According to Osborne and Swarbrick (1997) when the overpressure is close to the lithostatic pressure, a small increase of pore pressure will cause hydraulic fracturing, providing pathways for fluid escape. Therefore here we propose that hydraulic fracturing occurred at the top of the MTC bodies which provided conduits for the influx of gas migration to the overlying sediments and caused the formation of the non-aligned HAAs (Cox et al., 2001; Hilgers et al., 2006). Some of the fractures can be observed on seismic data as faults of small offset, while others are probably too small to be observed on seismic data. We hypothesize that the overpressure could be generated by released gas and water from hydrate dissociation, as well as caused by the rapid sediment loading and the low permeability of the MTC sediments (Osborne and Swarbrick, 1997; Cox et al., 2001; Sultan, 2004a). The gas could be released from gas hydrates or generated within the in situ sediments, which needs further study using additional data.

Generally the spatial relationship of these HAAs and the buried MTCs is strong evidence for upward gas migration along margins or local faults associated with underlying MTCs. For the HAAs in the western group, the high amplitudes may be caused by two factors, gas (relict from passing fluid migration) and coarser sediments (deposited by bottom currents or by fluid venting-related winnowing process). Both factors are related to upward fluid migration. Other HAAs are interpreted to be mainly caused by gas due to upward fluid migration along margins or local faults associated with underlying MTCs. The smaller-scale HAAs below and above the main HAA interval indicate the possible fluid migration route, like the gas flags along fault planes (Pilcher and Argent, 2007). So we propose that the upward fluid migration controlled by MTCs may have played a significant role in the formation of these HAAs.

3.7 Relationship with the gas hydrate system

In this area the BSR is regionally distributed, suggesting a widespread hydrate formation. Submarine gas hydrates may dissociate spontaneously when the hydrate stability conditions change (e.g. Dickens et al., 1995; Sloan, 1998; Berndt et al., 2002). That will probably have an effect on overpressure because of the large volume of gas and water it releases (Sultan et al., 2004ab; Bünz et al., 2005). It is said that the stability of the GHSZs can be rebuilt in hundreds of years after the MTC events (e.g. Berndt et al., 2002). The vertically stacked depressions in the western HAA group are located in an interval of ~ 130 m above the MTCs, and it may have taken 0.8-1.6 m.y. to form because the sedimentation rate in this area is ~ 80-160 m m.y.$^{-1}$ (Krastel et al., 2006; Henrich et al., 2008).

Structures associated with MTCs (e.g. slumping scarps) can promote fluid migration due to their comparatively higher permeability (Foland et al., 1999; Pilcher and Argent, 2007). Based on the analysis of the HAAs and related underneath MTCs, we propose that there was gas migration along margins or local faults associated with MTCs which caused the formation of the HAAs. Davies et al. (2012) described the multiple shifts of the BSR in this area, probably caused by pulsed sedimentation during repeated glacial-interglacial cycles. So we propose that the fluid flow which caused the formation of the HAAs here was probably caused by the dissociation of gas hydrates due to the upward resetting of the base of gas hydrates. However it is also possible that the fluid was from in situ biogenic gas, squeezed pore fluids from compaction or deep thermogenic gas, which needs further study using additional data such as geochemistry data.

The fluid migration indicated by the HAAs may play a role in transporting gas to the above gas hydrate system. Shallower than these HAAs, the faults with small offsets are interpreted as efficient fluid migration pathways through which the released gas from hydrate dissociation can be recycled back to the new gas hydrate system at shallower depth (Yang and Davies, 2013). As a result these two stages of fluid migration associated with MTCs and faults in this area may represent the gas migrating history between free gas traps and the gas hydrate system. In most cases the in-situ biogenic gas in the host sediments is considered to be insufficient to form gas hydrates, so this focused fluid migration mechanism may be significant for the hydrate formation (Hyndman and Davis, 1992; Haacke et al., 2007).

3.8 Conclusions

Detailed mapping of 3D seismic data from offshore Mauritania reveals many localized HAAs above some MTCs. These HAAs were divided into two populations. One includes three aligned linear groups of HAAs while the other population indicates the HAAs that are non-aligned. The HAAs in the western group are located in depressions above the intersection line of three MTCs, and they are interpreted to be caused by gas left after upward gas migration and coarser sediments deposited by bottom currents or fluid venting-related winnowing process, both related to fluid migration. The HAAs in the other two groups are interpreted to be caused by gas which was transported upwards along the margins or faults associated with MTCs. The non-aligned HAAs are also interpreted to be caused by gas which was probably transported upwards from underlying MTC bodies where the overpressured fluid may have caused hydraulic fracturing at the tops of the MTCs, allowing gas migration to the overlying sediments.

The fluid which caused the formation of these HAAs may be released from the dissociation of gas hydrates due to the upward resetting of the BSR, but it may also be from other sources such as the in situ biogenic gas, squeezed pore fluids from compaction or deep thermogenic gas. Together with the shallower faults which act as recycling routes for released gas from hydrate dissociation (demonstrated in next chapter), they may represent the gas migrating history in this area. Since buried MTCs and gas hydrates can coexist in marine environments, revaluation of the role of MTCs in transporting fluid flow is of great importance to understand the fluid migration history on continental margins and the mechanisms of gas supply to the gas hydrate system.

Chapter 4: Gravity-driven faults: migration pathways for recycling gas after the dissociation of marine gas hydrates

Abstract

High resolution three dimensional seismic data from offshore of Mauritania (West Africa) reveal tiers of normal and tear faults that are approximately parallel to the strike and dip of the slope respectively. They formed as a result of multiple episodes of down-slope creep and have propagated through 70-160 ms of sediments. Some intersect the seabed while others are buried and formed during earlier down-slope translation. Gas hydrates, the base of which is evidenced by aligned amplitude terminations or a bottom simulating reflection, form within the faulted succession. There are spatial relationships among the fault locations, breached gas accumulations and the location of shallower free gas sealed by hydrates. These are consistent with the upward-resetting of the base of the hydrates, the migration of dissociated gas up the faults to either become trapped below its reset base in a new free gas zone or potentially recycled back into a hydrate phase. There is little evidence for venting of dissociated gas at the seabed. Gravity-driven faulting is common on continental and island slopes, where gas hydrates are expected to occur, therefore this model for the utilization of gravitationally driven faults for the migration and recycling of gas should be generally applicable.

4.1 Introduction

Gas hydrates are crystalline compounds with gas molecules held in cages of water molecules, and are only stable in the gas hydrate stability zones (GHSZs) under specific pressure-temperature (P-T) conditions in marine environments or permafrost (Brown et al., 1996; Bünz et al., 2003). There are many factors affecting the stability of hydrates, such as deposition and erosion, slope failure, bottom water temperature change, sea level change, gas composition and pore-water salinity (e.g. Bünz et al., 2003). The presence of hydrates reduces the permeability of sediments, making the hydrate-bearing sediments a seal which can trap free gas below (Berndt et al., 2004; Hustoft et al., 2007). In seismic data, the base of gas hydrate stability zone (BHSZ) is marked by either a bottom simulating reflection (BSR) which often has high amplitude and opposite polarity to the seabed or aligned terminations of high amplitude reflections caused by the low velocity gas-charged sediments below the BHSZ (Andreassen et al., 1997). The presence of hydrates offshore Mauritania is marked in most areas by aligned amplitude terminations rather than BSRs. Since the BHSZ represents the transition from gas hydrates to free gas (Bünz et al., 2003), the resetting of BHSZ due to a change in hydrate stability condition (e.g. P-T) will cause hydrate dissociation (upward resetting) or hydrate formation (downward resetting; Davies and Clarke, 2010).

Gas in the gas hydrate systems can be recycled between the GHSZ, FGZ and other free gas traps due to the resetting of BHSZ (Pecher et al., 1996, 2001; Taylor et al., 2000; Davies and Clarke, 2010). Although it has been recognized that there is gas recycling in the gas hydrate systems, the specific mechanisms or migration pathways are not well explained (Pecher et al., 1996; Haacke et al., 2007). Hornbach et al. (2004) proposed that the overpressure of the FGZ may cause fault reactivation and gas escape through the hydrates. Davies and Clarke (2010) proposed that chimneys can act as the pathways for repetitious gas leaking from stratigraphic traps to the gas hydrate system.

Sliding, slumping and creep are common on deep-water slopes where gas hydrates are expected to coexist (e.g. Ferentinos et al., 1981). In these settings, faults caused by downslope movement of sediments are common which may act as fluid migration conduits due to their higher-permeability than surrounding sediments (e.g. the Storegga Slide (Brown et al., 2006); the Niger Delta (Leduc et al., 2012); the lower Congo Basin (Gay et al., 2007).

Here we use 3D seismic data from offshore Mauritania to consider the role of gravitationally-driven faults in the shallow subsurface as routes for the migration and recycling of free gas which is released from hydrate dissociation as a result of the upward resetting of the BHSZ.

4.2 Gas migration in hydrate systems

Pecher et al. (1996 and 2001) proposed three processes that supply free gas to the hydrate systems, biogenic gas generation, hydrate dissociation and gas migration from below. The first process indicates a biogenic breakdown of organic material (Pecher et al., 1996). It mainly occurs in sediments of high organic carbon content because of the low efficiency of biogenic gas generation. The second one, hydrate dissociation, occurs when the BHSZ resets upward due to temperature increase (e.g. caused by sedimentation; bottom water warming) or pressure decrease (e.g. caused by tectonic uplift), converting hydrates to gas and water (Pecher et al., 2001; Haacke et al., 2007; Davies and Clarke, 2010). The third process involves focused fluid flow through subsurface structures (e.g. faults, chimneys), and we may observe authigenic carbonates at cold vents with gas supplied from below (Pecher et al., 2001).

Fluid migration supplies gas and water to the shallower hydrate systems, contributing to the formation of hydrates, FGZ and BSRs (Miller et al., 2012). There are two main mechanisms of gas migration which could have a role in gas recycling in the hydrate system, diffusion and advection (Liu and Flemings, 2006; Haacke et al., 2007). Diffusion occurs at a molecular scale where gas is dissolved in pore water and it is driven by a concentration gradient (Miller et al., 2012). Advection is a transport mechanism of gas by fluid flow or free gas in a certain direction which occurs in focused pathways (Berndt, 2005). The focused migration pathways include faults, chimneys and faulted anticlines, which are much more effective for gas migration than diffusion in tectonically active margins (Abrams, 1992; Gay et al., 2007; Haacke et al., 2007). Many samples of hydrate-charged sediments have been recovered near to faults, diapirs, or vents and therefore these deformational structures have been interpreted to have played a role in determining pathways for gas migration to the hydrate systems, providing gas for the hydrate formation (Laberg and Andreassen, 1996). These structures can also act as pathways providing higher permeability routes for gas to move out of FGZ even through the GHSZ to the seabed, causing instability on slopes or even affecting global climate change (Pecher et al., 1996; Hornbach et al., 2004).

Gas recycling is common in gas hydrate systems, between the GHSZ, FGZ and other free gas traps (Pecher et al., 1996; Davies and Clarke, 2010). Hydrate dissociation due to upward resetting of BHSZ will release large volumes of free gas, stored in FGZs or stratigraphic traps. When the BHSZ resets downward due to temperature and pressure change (e.g. caused by tectonic subsidence, non-sedimentation or seafloor erosion), the free gas below will be absorbed into the hydrate system, forming new hydrates. Davies and Clarke (2010) studied the mehcanism of gas recycling between hydrates and stratigraphic traps. They proposed that the free gas dissociated from hydrates can be trapped in stratigraphic traps. When these traps are critically pressured, the seal capacity will be exceeded and free gas will migrate upward along the hydraulic fracturing to shallower stratigraphic traps or even to the base of hydrates. When the dissociated gas hits the base of hydrates, it can stay in the new FGZ or form new hydrates. Offshore Mauritania there are many gravitational faults formed during processes like creep, which have higher vertical permeability than surrounding sediments.

4.3 Geological setting

The offshore Mauritania Basin on the West African passive continental margin was initiated during Middle to Late Jurassic times with the opening of the Atlantic Ocean (Vear, 2005; Antobreh and Krastel, 2007). The present dip of the continental slope is 1°- 3°, and the TWT time of the seabed in the study area varies from 200 to 3000 ms. At 3000 ms, the slope is ~ 1° (Henrich et al., 2008). The seabed is characterised by two major canyon systems running in an east-west direction. On the western side of the study area there are several tear faults (small displacement faults with strike-slip motion) which are parallel or oblique to the slope dip (Fig. 4.1).

For the last ~ 20, 000 years, wind-blown sediments from Sahara Desert have been the main source of sediment input into this area and to the north of the Cap Timiris area there were even periods of fluvial sedimentation during the Early Holocene period

(Antobreh and Krastel, 2007; Henrich et al., 2008). The succession we study here is characterised by fine-grained turbidites, debris flows and hemipelagic sediments (Vear, 2005; Krastel et al., 2006). Based upon Ocean Drilling Program (ODP) well data (Ruddiman et al., 1988), the offshore of Mauritania has had a variable sedimentation rate, ranging from several to hundreds of m m.y.$^{-1}$ (e.g. 2.5 at site 657 at around 8.4 Ma; 146 at site 658 between 0.7 to 1.5 Ma), depending on the climate, sediment supply and tectonic setting at that time. The host strata we investigate are located between the seabed and 600 ms below, and deposited since the Neogene (Vear, 2005). During this period the sedimentation rate was high due to an ocean margin upwelling regime, averaging 80-160 m m.y.$^{-1}$ (Krastel et al., 2006; Henrich et al., 2008).

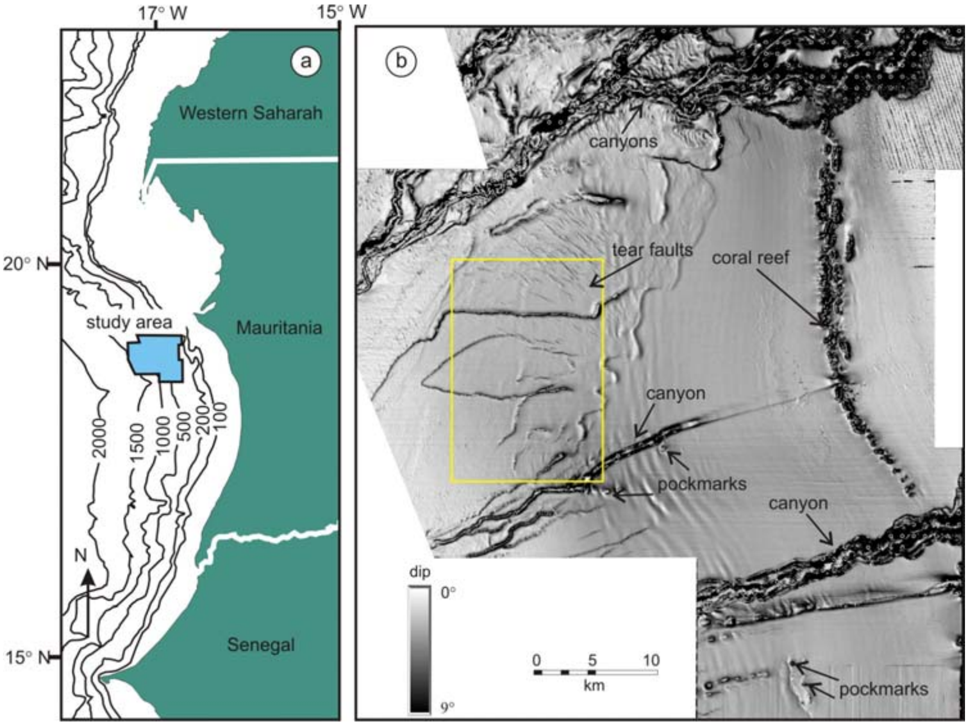

Fig. 4.1 (a): Location of study area with bathymetry contoured in metres. (b): Apparent dip magnitude map of the seabed offshore Mauritania showing structural and sedimentary features such as tear faults, canyons, pockmarks and coral reef. The yellow box shows the location of the plan-view maps in figures 4.2-4.6.

4.4 Seismic data and methodology

The 3D seismic dataset covers an area of ~ 4000 km^2. They were time-migrated and processed by several steps through multiple suppression and post-stack time migration. The main frequency of the 3D seismic data is 50 Hz, yielding a vertical resolution of ~ 8.5 m which equals one quarter of the wavelength at the dominant frequency, assuming a sediment velocity of 1700 m s^{-1} (Davies and Clarke, 2010). The final bin spacing of the seismic grid is 25 m x 25 m. In the seismic cross sections, a reflection event consisting of a red loop followed by a black loop represents an increase of acoustic impedance. The vertical axis is in two-way-travel (TWT) time, and we assume a seawater velocity of 1450 m s^{-1} and a sediment velocity of 1700 m s^{-1} to convert time to depth (Davies and Clarke, 2010; Davies et al., 2012b).

Several key reflections were interpreted, including four representative stratigraphic reflections and the BHSZ. They were used to generate seismic attribute maps such as apparent dip magnitude maps and reflection amplitude maps which provide structural and stratigraphic information (see Brown, 2010) and help analyse local interval changes. Apparent dip magnitude maps show the values which highlight the structural features. Amplitude maps using the peak or trough amplitude of a reflection are useful for identifying gas and fluid migration, lithology and unconformities (e.g. Brown, 2010). We also generated a horizon for windowed amplitude extractions. Root-mean-square (RMS) amplitude maps between horizons are used to detect the anomalous amplitudes. The RMS amplitude is calculated as the square root of the average of the squares of the amplitudes in an analysis window, therefore it is very sensitive to extreme amplitude values, which may be related to lithological changes, diagenetic changes or fluids (e.g. gas or oil). See Appendix C for supporting figures.

4.5 Observations

The four representative reflections we interpreted are named I-IV from top to bottom respectively, and the BHSZ was also interpreted (Figs 4.2-4.6). Reflection I is the present seabed and reflections II and III are located at ~ 200 and 300 ms below the seabed separately (Fig. 4.2d). Reflection IV is located at ~ 50 ms below reflection III (Fig. 4.3a). In addition, we interpreted three reflections locally (V, VI and VII) to study the faults and high amplitudes. In the following sections we describe a number of troughs (numbered 1-19) and associated amplitude anomalies. Some of the troughs are parallel and oblique to the slope dip while others are parallel to the slope strike.

4.5.1 Troughs

Apparent dip magnitude maps of reflections I and II (Fig. 4.2ab) show that the troughs are either parallel or oblique to the slope dip and have elongate en echelon planforms. They have variable lengths ranging from 0.5 km to 10 km. In the two representative seismic cross sections (Fig. 4.2de) we observe that these troughs are vertically aligned, ~ 70 to 160 ms in TWT time. These troughs have narrow bases and broad tops with and without discernible offsets.

Apparent dip magnitude maps of reflections III and IV (Figs 4.2c and 4.3bc) show an extensive strike-parallel linear trough which is ~ 420 m wide and ~ 21 km long. Half way along the linear trough, there is a change in orientation, from strike-parallel to dip-parallel (Figs 4.2-4.6). There are also several linear troughs parallel or oblique to the dip of the slope to the west of the linear trough (e.g. trough number 10, Figs 4.2c and 4.3bc). A seismic cross section (Fig. 4.3a) shows that the vertical stack of the strike-parallel trough starts at reflection IV with a small offset at this reflection and terminates at approximately the level of reflection III. This trough occurs over an interval of ~ 100 ms (inset, Fig. 4.3a). Through comparing T1 with T2 (inset, Fig. 4.3a), we see an interval change of the interval between reflection IV and V on the two sides of this trough, ~ 10 ms.

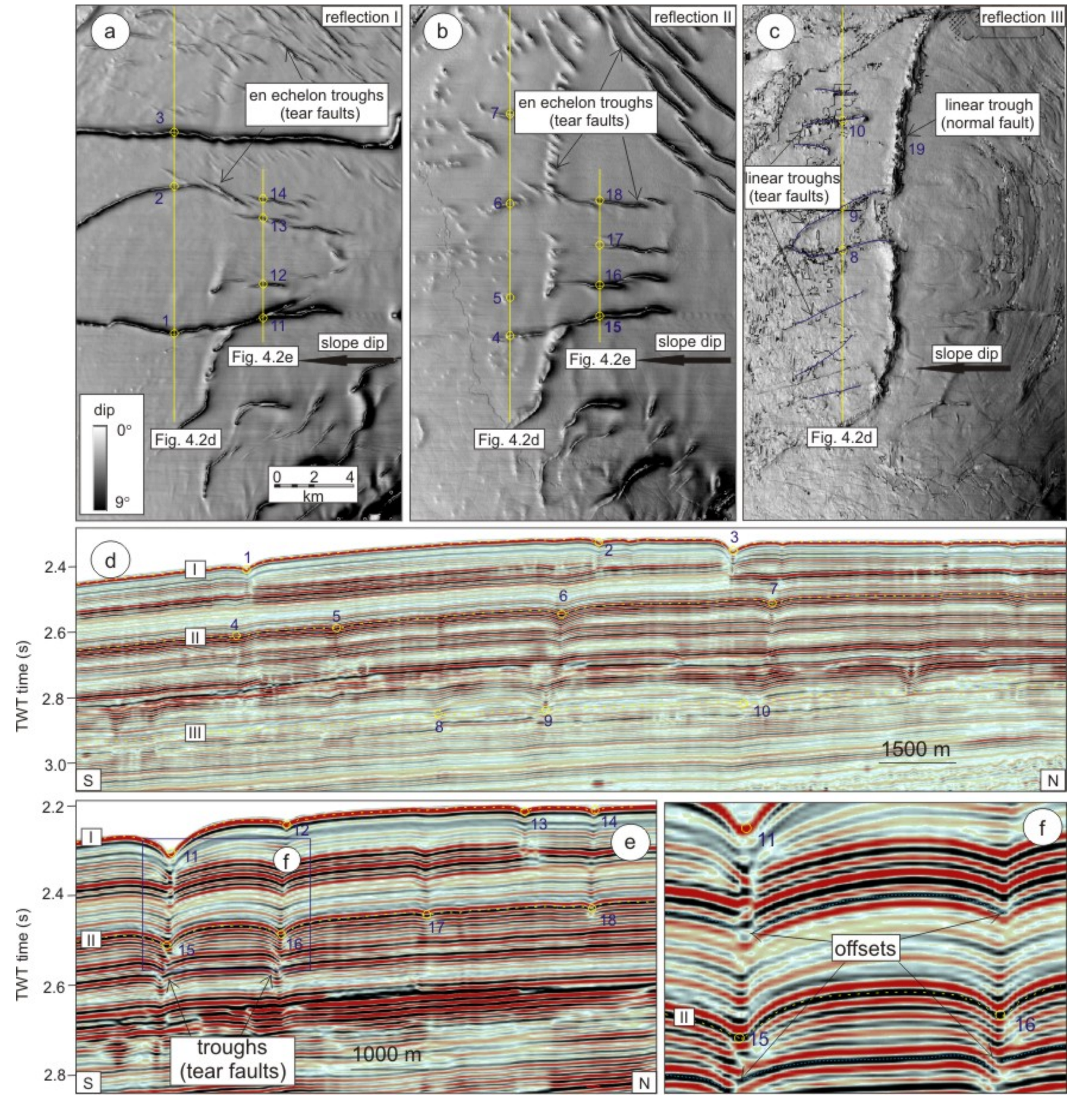

Fig. 4.2 (a-c): Apparent dip magnitude maps of horizons I, II and III, showing en echelon and linear troughs. The troughs are parallel/oblique to the slope dip or parallel to the slope strike. (d): A seismic cross section (inline: 10980) showing the vertical characteristic of the troughs. (e): Another seismic cross section (inline: 11298) showing the vertical troughs which are interpreted to be tear faults, some of which have discernible offsets. (f): Zoomed in image of the blue box in e, showing the offsets. The blue dotted lines help show the small offsets. Location of the seismic sections is shown in a-c. Numbers 1-19 allow for specific troughs to be located on both seismic sections and apparent dip magnitude maps.

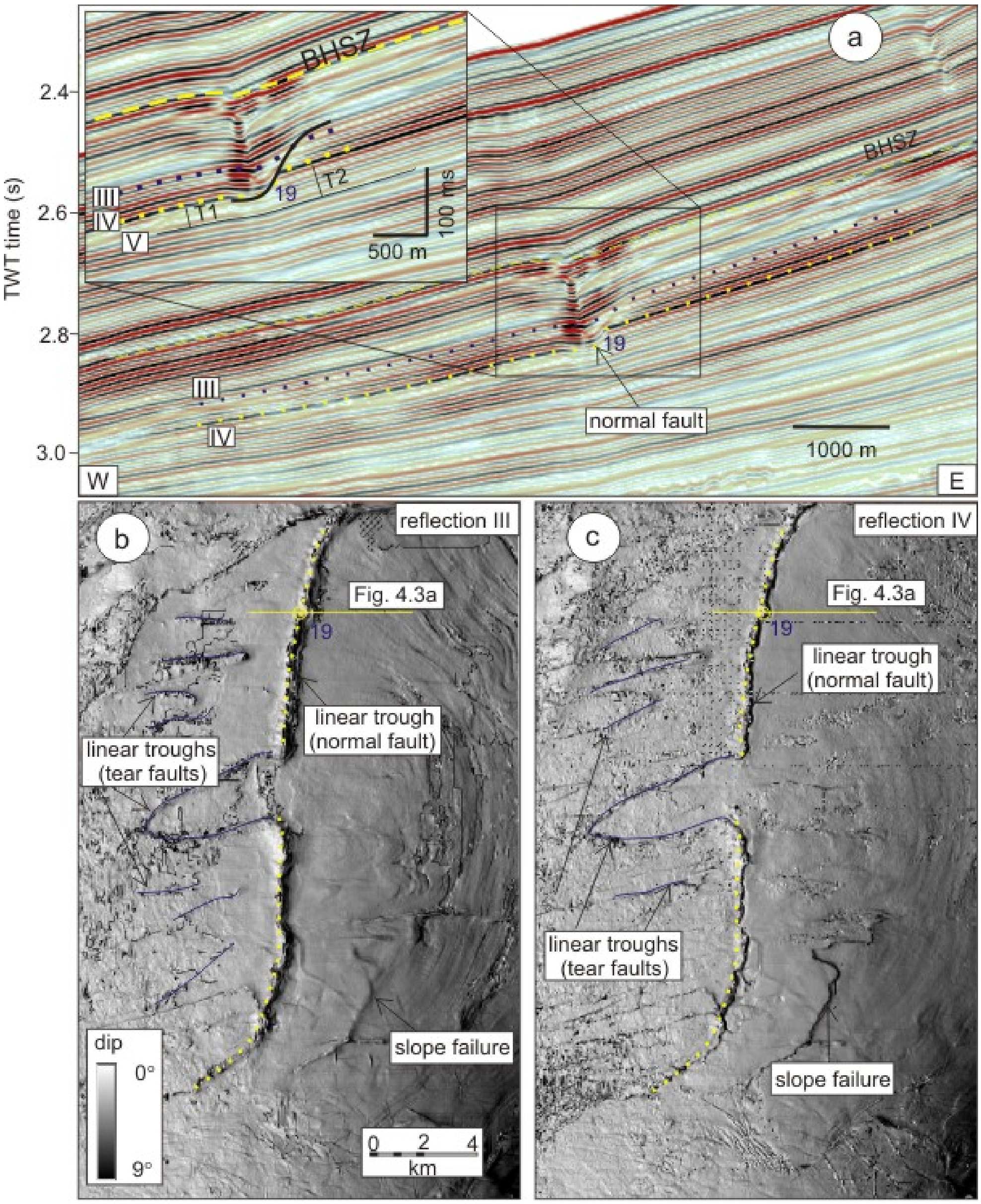

Fig. 4.3 (a): A seismic section showing the gravitational normal fault indicated by the arrow. The offset is ~ 10 ms. At reflection III, there is a section of high amplitude anomaly, ~ 250 m long, and terminate updip at the fault plane. Inset: zoom-in image of the black box, showing the normal fault. Comparing T1 with T2, there is an obvious thickness change of the interval across this fault. Location of this seismic section is shown in b. (b, c): Apparent dip magnitude maps of reflection III and IV showing the linear trough in the middle which is interpreted to be a normal fault and some linear troughs to the west of the normal fault which are interpreted to be tear faults.

4.5.2 Amplitude anomalies

4.5.2.1 Widespread high amplitudes

There are widespread high amplitudes at two levels in this study area (Figs 4.4 and 4.5). The deeper one starts at reflection VI and the shallower one is located immediately below the BHSZ. We start by describing the deeper one.

The amplitude map of reflection IV (Fig. 4.4a) shows that the high amplitudes mainly occur to the east of the strike-parallel linear trough (number 19), while the reflection to the west of this linear trough is of consistently low amplitude. The eastern high amplitude zone is split into northern and southern regions by an area of low amplitude (Fig. 4.4a). Three representative cross sections perpendicular and parallel to the linear trough (Fig. 4.4b-d) were chosen to study the vertical features of the high amplitudes. It shows that the updip of the linear trough at reflection IV has high amplitude. In contrast the downdip of the linear trough has low amplitude and an uncertain polarity. The western termination of the high amplitude zone is at the strike-parallel trough while the position of the eastern termination is variable and does not abut any deformational structures (Fig. 4.4a-c). The seismic cross section which is parallel to the linear trough (number 19) (Fig. 4.4d) shows that the low amplitude area at reflection IV is spatially coincident with the shallower high amplitude reflections above it.

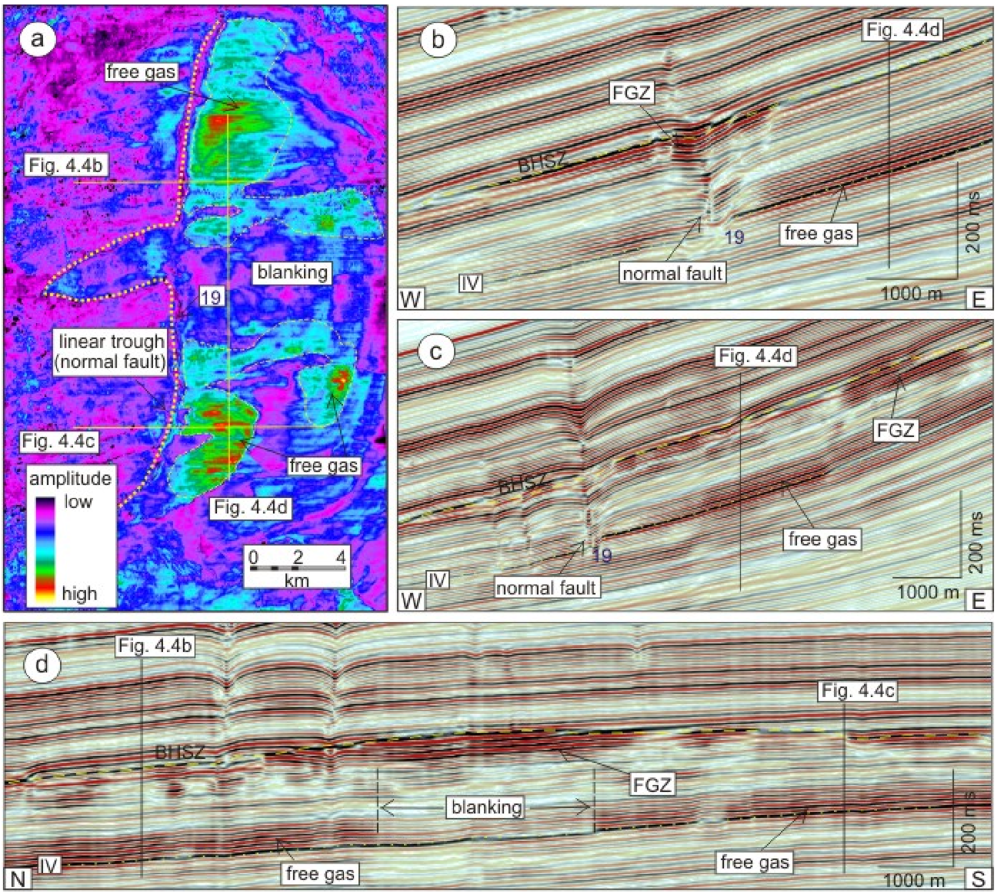

Fig. 4.4 (a): Amplitude map of reflection IV, showing the normal fault, free gas accumulations and amplitude blanking. (b, c): Seismic cross sections perpendicular to the direction of the linear structure, showing the distribution of free gas at reflection IV and the free gas zone above sealed by hydrates. (d): Seismic cross section parallel to the direction of the normal fault showing amplitude blanking. Locations of these seismic sections are shown in a.

A RMS amplitude map (Fig. 4.5a) was produced within a window between BHSZ and VII (50 ms below the BHSZ) to study the shallower high amplitude anomalies below the BHSZ. It shows a curvilinear planform to the east of the strike-parallel linear trough (number 19). Seismic cross sections (Fig. 4.5bc) show that these high amplitude reflections which terminate updip against the BHSZ mainly exist above the linear trough and in the updip position. Comparing this RMS amplitude map (Fig. 4.5a) with the amplitude map of reflection IV (Fig. 4.4a), we note that the curvilinear high amplitude zone sealed by the BHSZ is spatially coincident with the underneath low amplitude area at reflection IV which splits the eastern high amplitude zone into two regions.

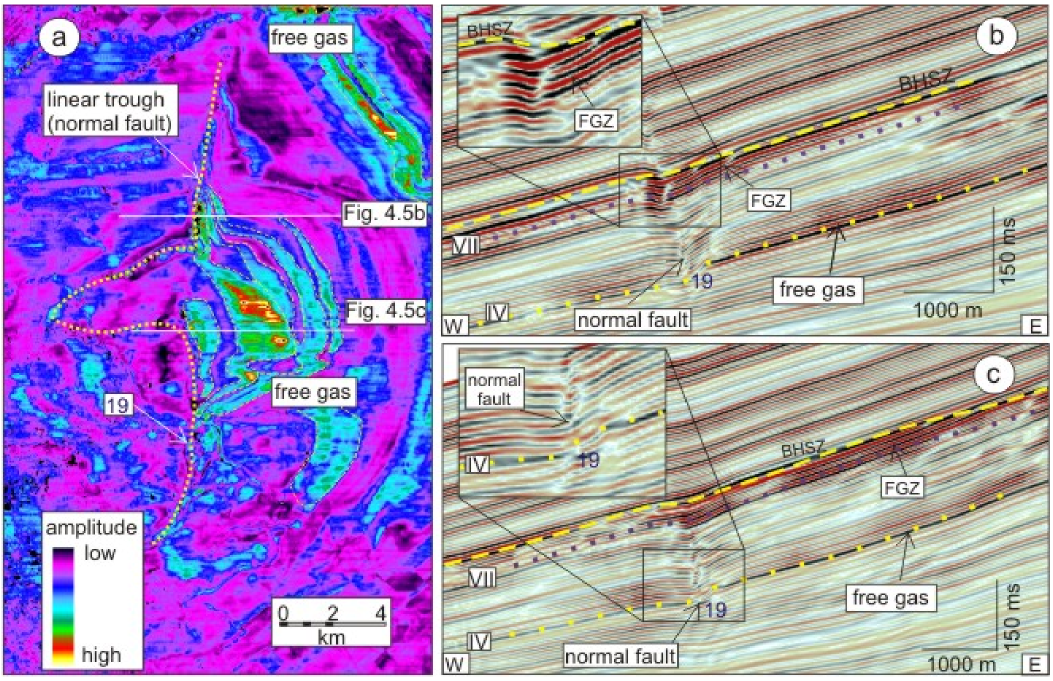

Fig. 4.5 (a): RMS amplitude map which is produced within a window between the BHSZ and reflection VII (50 ms bellow the BHSZ), showing the distribution of FGZs which mainly exist on the eastern side of the normal fault (updip). The N-S oriented yellow dotted line in this map is taken from figure 4.3, showing the fault structure underneath this reflection. (b, c): Seismic cross sections showing the distribution of FGZs above the normal fault, on the updip eastern side of the fault. Locations of seismic sections are shown in a.

4.5.2.2 Localized high amplitudes

The amplitude map of reflection III (Fig. 4.6a) shows that the amplitude is comparatively low on both sides of the linear troughs (number 8, 9 and 19). Along the troughs there are many examples of localised high-reflection amplitudes which have variable geometries (Fig. 4.6a-c). They are elongate along the strike-parallel trough and sub-circular along the dip-parallel troughs (Fig. 4.6bc). In seismic cross sections the localized high amplitudes mainly occur on the downdip side of the strike-parallel linear trough (number 19), ~ 250 m long and terminates updip at the trough (Fig. 4.3a), while for the dip-parallel linear troughs (number 8 and 9) (Fig. 4.6d) the high amplitudes are ~ 150 m long and occur within the troughs. We see an increase in reflection strength in these troughs, but there is no evidence for polarity changes or erosional processes such as reflection truncation (e.g. at the level of reflection VI, Fig. 4.6).

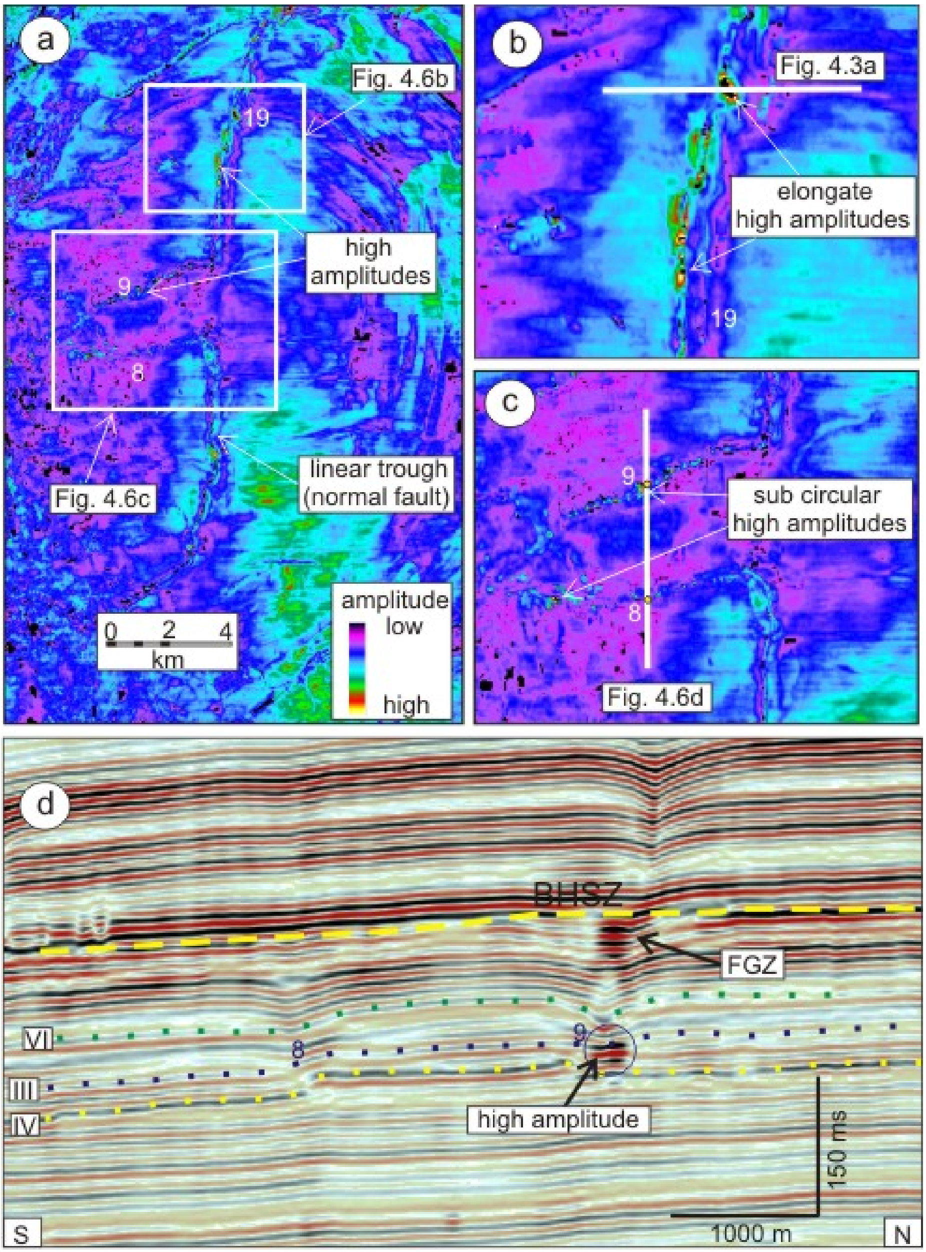

Fig. 4.6 (a): Amplitude map of reflection III, showing the high amplitudes along the faults. (b): Zoomed-in image of the northern white box in a, showing the elongate high amplitude anomalies. A seismic cross section through one anomaly is shown in Fig. 4. 3a. (c): Zoomed-in image of the southern white box in a, showing the sub circular high amplitude anomalies. (d): A seismic cross section showing the high amplitude anomalies of ~150 m within the tear faults (number 8 and 9) and the FGZ above it. Location of this seismic section is shown in b.

4.6 Interpretations

4.6.1 Tear and normal faults

The troughs that are parallel and oblique to the slope dip have elongate, en echelon or linear geometries and some have discernible offsets which indicate small-scale faults. These features are consistent with them being the earliest stages in tear fault development which was caused by the low-velocity movement of sediments during down-slope creep (Ferentinos et al., 1981). Creep is a slow gravitational deformation process which occurs where the shear stress is too low to trigger rapid slope failures (Rutter and Green, 2011). Normally there are lateral offsets across strike-slip faults, but the tear faults here do not show any obvious lateral offsets which may be caused by the lack of suitable markers (e.g., depositional features). We propose that these tear faults have higher permeability than surrounding sediments and can act as conduits for gas migration, transporting gas upwards to shallower traps. Similar arguments have been made for the polygonal faults in the Norwegian margin which are located in fine grained sediments and also have very small offsets (Gay and Berndt, 2007). Once reactivated, these polygonal faults can act as fluid migration conduits.

The strike-parallel linear trough (Fig. 4.3) that has a small-scale offset of ~ 10 ms is interpreted to be a gravity-driven normal fault. Although this N-S orientated fault has a small downslope translation (indicated by the 10 ms offset), its length (~ 21 km) shows that an extensive section of the margin has moved downslope. The presence of this fault is consistent with it being a higher-permeability route than surrounding strata for gas migration.

Normally the shear strength of hydrate-charged sediments is increased due to the effect of hydrate cementation, increasing slope stability (Sultan et al., 2004ab). But it is not possible to detect the top of the hydrate zone. Therefore we do not know if the gravitational faults on the slope are located in the hydrate zone or not.

4.6.2 Free gas accumulations and migration

4.6.2.1 Accumulations

We start by interpreting the deeper high-amplitude reflections then the shallower ones. In seismic data, these reflections of high amplitude are interpreted to be free gas accumulations (Berndt et al., 2004). The amplitude map of reflection IV (Fig. 4.4a) shows that the free gas mainly accumulates to the east of the normal fault. This free gas accumulation is bounded by the normal fault on its western side. On the eastern side it is regarded to be bounded by low-permeability sediments because there is no deformational structure. Therefore this free gas accumulation is structurally sealed (fault-bound) downdip and stratigraphically sealed updip. The free gas stored in this accumulation could be either from the deep sources (e.g. thermogenic gas origin) or from the hydrate dissociation (Davies and Clarke, 2010).

The shallower curvilinear zones of high amplitude which are sealed by the BHSZ are interpreted to be FGZs (Fig. 4.5). These FGZs are located on the updip side of the linear normal fault. The free gas in the FGZs may be from either gas sources below or the hydrate dissociation, or a mixture of the two origins. There is a spatial relationship between the low amplitude area which separates the eastern high amplitude zone at reflection IV and the FGZ above (Figs 4.4 and 4.5). Therefore we interpret the low amplitude area (Fig. 4.4ad) to be the result of amplitude blanking, caused by the FGZ above (Fig. 4.5). The homogeneity between the FGZ and the stratigraphic free gas accumulation below (Fig. 4.4d) reduced the contrast of acoustic impedance and causes the amplitude blanking.

4.6.2.2 Migration

The faulting at reflection VI where the faults terminate (Fig. 4.6d) shows a depression caused by subsidence rather than erosion, suggesting that reflection VI was not the seabed at the time of faulting. The localized high amplitudes along the faults (Fig. 4.6) are interpreted to be indicators of gas migration, suggesting there is gas migration from the deeper stratigraphic trap to the shallower FGZs. These localized high amplitudes may be caused by either free gas or gas-related diagenesis which cannot be pinpointed without more geophysical or core analysis. Similar phenomena have also been reported in the

Mediterranean Sea (Ligtenberg, 2005) and the Lower Congo Basin (Gay et al., 2007) where the local high amplitude zones associated with the faults were interpreted as free gas (subsurface) and pockmarks (seabed) separately, both of which indicate upward fluid migration. In the Vulcan Sub-basin, a high amplitude reflection with positive polarity was interpreted to be a carbonate-related diagenetic zone which is also one of the seismic indicators for gas migration (O'Brien and Woods, 1995).

In summary, we see a clear spatial relationship among the deeper stratigraphic gas accumulation, the normal fault, the localized gas migration indicators and the shallower FGZs above this fault. They provide the evidence to trace the gas which breached part of the deeper stratigraphic trap, then migrated upward along the fault and finally it reached the BHSZ and was resealed in FGZs.

4.7 Model

The deeper stratigraphic free gas accumulation is only a few hundred metres below the present BHSZ. Davies et al. (2012a) documented that the BHSZ in this area has reset upward due to sedimentation. Therefore although we cannot rule out a thermogenic gas origin, we propose that the free gas in the deeper stratigraphic trap is probably the released gas from hydrate dissociation. When the base of the hydrates reset to shallower levels, the hydrates dissociated due to the related temperature change (Davies and Clarke, 2010). Then the released free gas followed higher-permeability pathways and migrated to new traps.

The combined analysis of the faults, the free gas and the gas migration indicators allow us to propose a synoptic model to explain the gas migration along faults which occurs below the hydrates (Fig. 4.7). Down-slope creep causes gravitational normal faults and tear faults to form, and gas hydrates form within this faulted succession (Fig. 4.7a). As the BHSZ resets upwards due to the sedimentation at the seabed, the hydrates dissociate and free gas is released (Fig. 4.7b). The faults which have higher permeability than surrounding un-faulted sediments therefore act as the routes for the dissociated gas to migrate upwards until it reaches the new position of the hydrate stability zone (Fig. 4.7c). The free gas can accumulate there, stored in a FGZ sealed by the BHSZ. It can also form new hydrates and be recycled back into a hydrate phase. In this study, only the free gas on the western downdip side of the faults migrated upward along the faults and was recycled into the hydrate system. The dissociated gas on the eastern side of the faults was transported updip until it met the fine-grained sediments which acted as a seal and the gas was stored in a stratigraphic trap.

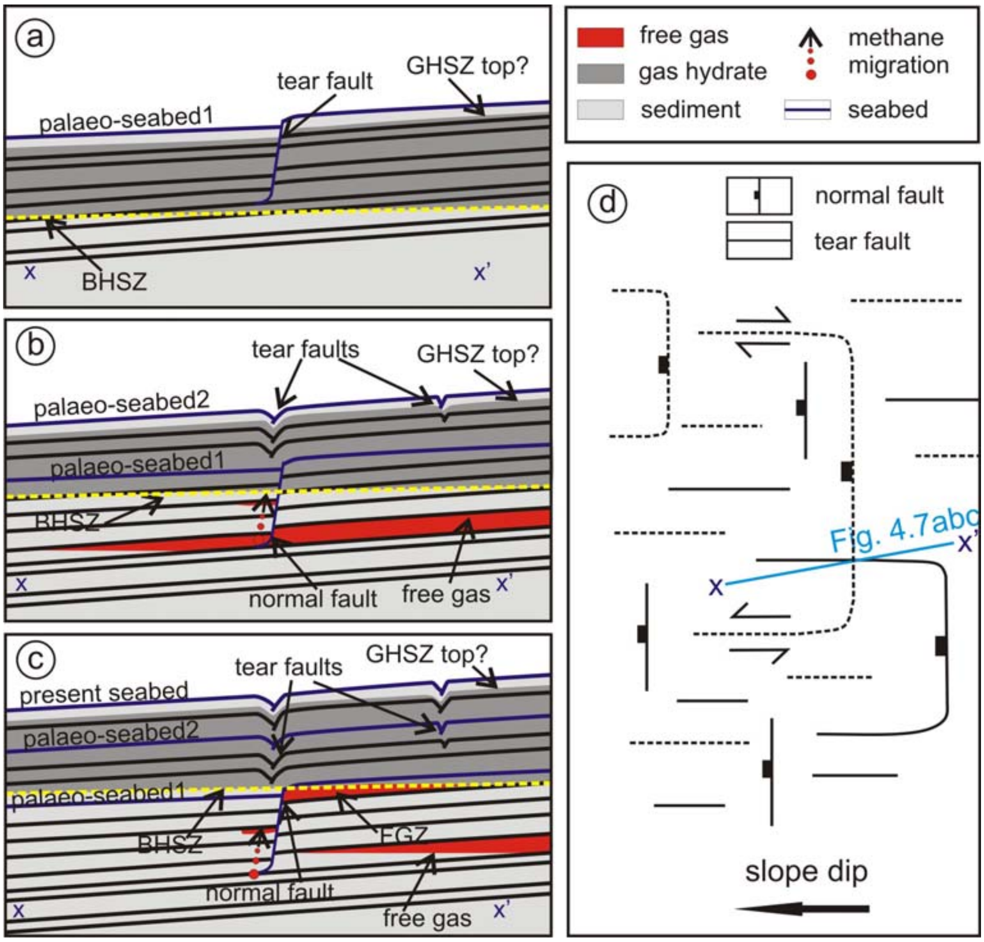

Fig. 4.7 Synoptic model for role of gravitational faults in gas migration on continental and island slopes. (a): Gravitational faults penetrating the first few hundred metres of stratigraphy in a slope setting, gas hydrates formed in this faulted succession. (b): Upward resetting of the BHSZ due to sedimentation, causing hydrates to dissociate. The fault of higher permeability than surrounding strata acted as a migration pathway, allowing the dissociated gas to migrate upwards. (c): As the BHSZ reset upward further, the released free gas from hydrate dissociation migrated upwards through the network of faults until it reached the new BHSZ. The dissociated gas on the higher side of the fault transported updip to a higher position until it reached a new seal. (d): Idealised map showing present and past normal and tear faults and the location of the cross sections in figure 4.7abc. The dashed lines indicate the fault distribution in stage a and b; the solid lines suggest the present faults in stage c. The normal faults are parallel to the slope strike and the tear faults are parallel to the slope dip.

A low saturation of free gas (3-5%) can cause a strong decrease of P-wave velocity, and the BSR is thought to be mainly caused by free gas rather than hydrates (Berndt et al., 2004). To test the existence of hydrates and free gas which are the basis of our model, we need further data like a velocity model or well-log data.

4.8 Conclusions

Gravity-driven faulting is common on continental and island slopes where gas hydrates are expected to occur. Here we observe two types of gravitational faults, tear faults and normal faults. These relatively higher-permeability gravitational faults can provide favourable pathways for gas migration, allowing gas migration to the shallower layers or gas recycling in the gas hydrate system.

There is a close spatial relationship between the faults and the free gas distribution, based on which a synoptic model is proposed. As the BHSZ resets upwards due to sedimentation, the faults with higher permeability than surrounding sediments act as pathways, channelling the released gas from hydrate dissociation upwards until it reaches the new position of the BHSZ. The free gas then can be stored in a FGZ or form new hydrates. Rather than migrate up the faults, the dissociated gas on the updip side of the fault would transport laterally in the same layer until it meets a seal. In summary there is a dynamic interplay among the hydrate dissociation, gas migration up along pre-existing faults and gas re-sealing at higher levels below the hydrates. To test this model, we need further information like a velocity model or well-log data.

The tear faults at shallower depth are also of high permeability and could be utilized as the gas migration pathways when the hydrate dissociation occurs there. Due to the common co-location of gravity faulting and hydrates in other continental and island slopes, this model should have general applicability and examination of other datasets may be productive.

Chapter 5: Controls on the base of gas hydrates offshore Mauritania: determined by 3D seismic imaging of the bottom simulating reflection

Abstract

High-resolution 3D seismic data from offshore Mauritania provide accurate information on seismic amplitude characteristics and the distribution of a bottom simulating reflection (BSR). On seismic sections the BSR is discontinuous, comprised of alternating bands of high and low seismic amplitude. On the amplitude map of the BSR, the amplitude bands are curvilinear and they dip towards different directions. The high amplitude bands are interpreted to be mostly caused by the presence of gas trapped below the base of gas hydrates, potentially in regularly spaced beds of coarser sediments. The changes in the planform geometry of the bands provide evidence of lateral changes in the ambient conditions that control the depth of the BSR. These changes occur due to variable water depth of the slope, impingement of salt diapir and mud diapir, and canyon cutting at the seabed. This chapter exemplifies that mapping the BSR on 3D seismic data can provide a wealth of information on lateral changes in the position of the base of the gas hydrate stability zone (BHSZ).

5.1 Introduction

Gas hydrates have been recovered globally in permafrost, marine and lake environments (Shipley et al., 1979; Vanneste et al., 2001). In marine environments, the gas hydrate stability zones (GHSZs) are controlled by many factors such as pressure and temperature (P-T), salinity, gas composition, heat flow and gas supply (e.g. Cooper and Hart, 2002). The base of gas hydrates is often indicated by a bottom simulating reflection (BSR) on seismic data, representing a phase boundary between the hydrate-bearing sediments above and free gas-charged sediments below (e.g. Bünz et al., 2003; Berndt et al., 2004). Most of the BSR amplitude is interpreted to be caused by the velocity reduction due to underlying free gas zones (FGZs; Singh et al., 1993; Haacke et al., 2007). As a result the hydrate-related BSRs often have negative polarity which is opposite to the seabed, crosscutting stratigraphy (Shipley et al., 1979; Bünz et al., 2003).

Seismic study of gas hydrates is mainly based on tracking the BSR and stratal reflections, focusing on the position of the BSR, hydrate-related fluid migration processes or the distribution of FGZs (Berndt et al., 2004; Davies et al., 2012a). Plan-view maps used in hydrate study are often generated by mapping stratal reflections crosscut by the BSR, and one map only shows the BSR characteristics at one single time (Bünz et al., 2003; Davies et al., 2012a). In this chapter we map the BSR, which follows a thermobaric surface, rather than stratal reflections. Compared with the maps of stratal reflections, the amplitude map of the BSR displays the characteristics of the whole BSR surface, at different times. This map is the result of the 3D intersection of the BSR and stratal reflections, providing a wealth of information on lateral changes in the position of the base of gas hydrates.

5.2 Geological setting and data

The study area is located on the passive continental margin offshore Mauritania which covers an area of ~4000 km^2 (Fig. 5.1). The sediment type in the study area is characterized by inter-bedded coarser sediments formed by turbidites or debris flows in a background of finer-grained hemipelagic sediments (Vear, 2005; Henrich et al., 2010). The high-resolution 3D seismic data allow for detailed mapping of the BSR which is widely spread in this area. The BSR is mainly characterized by aligned terminations of high amplitude reflections, crosscutting stratigraphy (Fig. 5.2a). In this chapter we discuss the BSR characteristics, describe the location of FGZs, and study their geological controls.

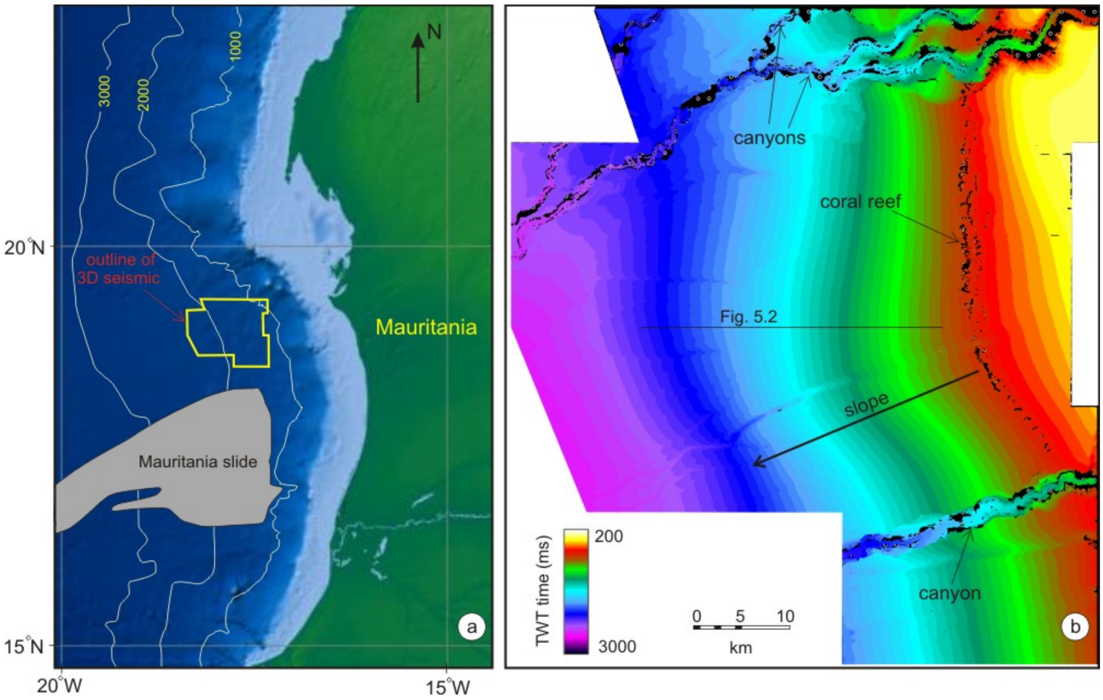

Fig. 5.1 (a): Location map of the 3D seismic data set offshore Mauritania. (b): TWT-structure map of the seabed in the study area, showing the slope direction and the distribution of canyons and coral reef.

The 3D seismic data have been processed by post-stack time-migration and have a 50 Hz main frequency (Fig. 5.1; Ireland et al., 2011). The seismic data have not been zero-phased, and no Automatic Gain Control (AGC) was applied. This seismic survey has a bin size of 25 m x 25 m. The vertical resolution is ~ 8.5 m which equals one quarter of the wavelength at the dominant frequency, assuming a sediment velocity of 1700 m s^{-1} (Davies and Clarke, 2010). On seismic sections, a reflection event consisting of a red loop followed by a black loop represents an increase in acoustic impedance downwards. The BSR in this chapter is featured by a black loop followed by a red loop, suggesting a negative polarity. We traced the BSR in the study area and generated the amplitude map of the BSR which is useful for identifying amplitude anomalies, providing information on lithology or fluids (Brown, 2010). See Appendix D for supporting figures.

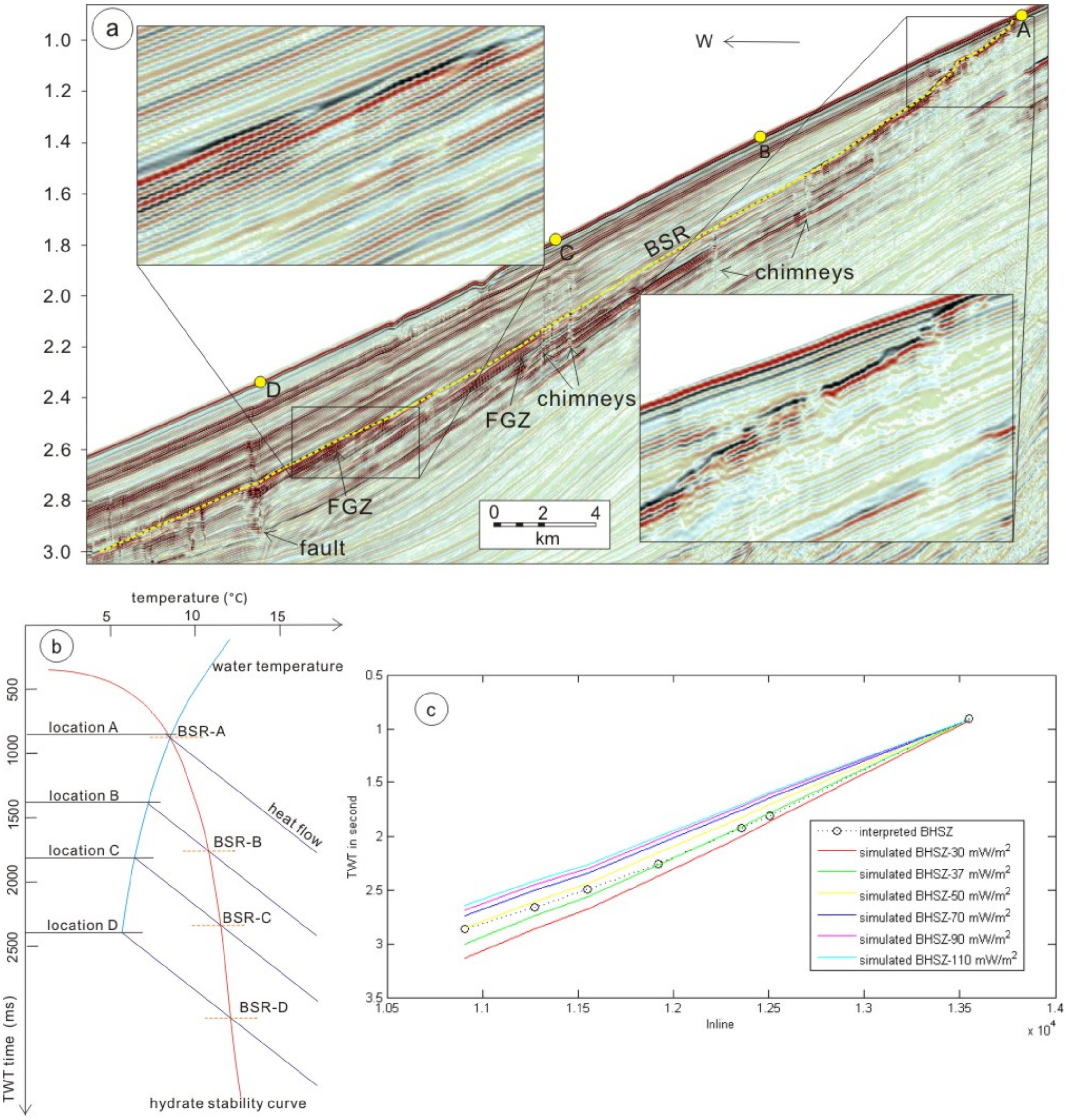

Fig. 5.2 (a): A regional seismic section (crossline: 24192) showing the BSR, FGZ, chimneys and a normal fault. Zoom in images show the specific seismic characters of the BSR. Vertical axis: Two-way-travel time (TWT) in seconds. See figures 5.1 for location. (b): A phase diagram showing the effect of seabed depth on BSR location. The BSR gets shallower as the seabed depth decreases. (c): Comparison of the modelled BSR (with different heat flow values) with the interpreted BSR (discussed in section 5.4).

5.3 Seismic Observations

5.3.1 The Bottom simulating reflection (BSR)

On seismic sections, the BSR is recognized as the aligned terminations of high amplitude reflections, composed of alternating sections of high and low amplitude (Fig. 5.2).

It has negative polarity, and crosscuts stratigraphy. The BSR is widely spread in this area, ~ 45 km long from west to east. On the upper slope, the BSR intersects seabed at ~ 880 ms in TWT time and the burial depth of the BSR decreases as the seabed depth gets shallower from west to east (Fig. 5.2a). Below the BSR there are high amplitude reflections, as well as focused fluid migration conduits such as chimneys and faults (Fig. 5.2a). On the amplitude map of the BSR (Fig. 5.3) we observe curvilinear bands of alternating high and low amplitude which bend to different directions. In the following sections we focus on five sub areas to study the BSR in detail.

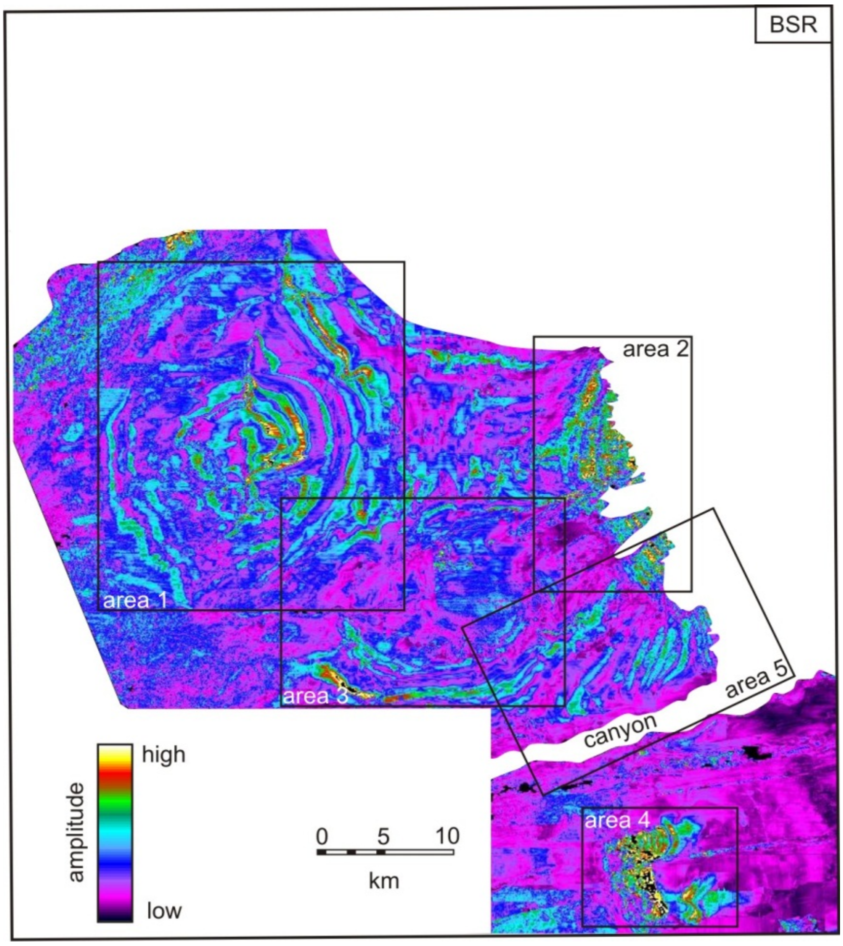

Fig. 5.3 The amplitude map of the BSR in the study area, showing the alternating bands of low and high amplitude. Five sub areas are confined by five rectangles to study the BSR characters. There is no BSR developed in the white zone on the eastern and southern sides.

5.3.1.1 Area 1

On the amplitude map of the BSR in area 1 (Fig. 5.4a), we observe curvilinear bands of high and low amplitude, bending to two opposite directions. The bands on the eastern side bend landward to the shallower eastern side while the bands on the western side bend seaward to the western side. On seismic sections the BSR is composed of alternating sections of high and low amplitude (pink and yellow lines) (Fig. 5.4b) which is consistent with the amplitude bands on the BSR amplitude map (Fig. 5.4a). The BSR on the eastern side is of lower apparent dip than stratigraphy (e.g. reflection a) and there are reflections of high amplitude sealed below the BSR (Fig. 5.4b). The geometry of the BSR on this side is discontinuous with high amplitude sections stepping downwards as corresponding seabed gets shallower from west to east, and this is defined as BSR type 1. The BSR on the western side is steeper than the stratigraphy (e.g. reflection b), and there is no high amplitude reflection sealed below the BSR (Fig. 5.4c). The geometry of the BSR here is also discontinuous, with high amplitude sections stepping upwards as corresponding seabed gets shallower from west to east, defined as BSR type 2.

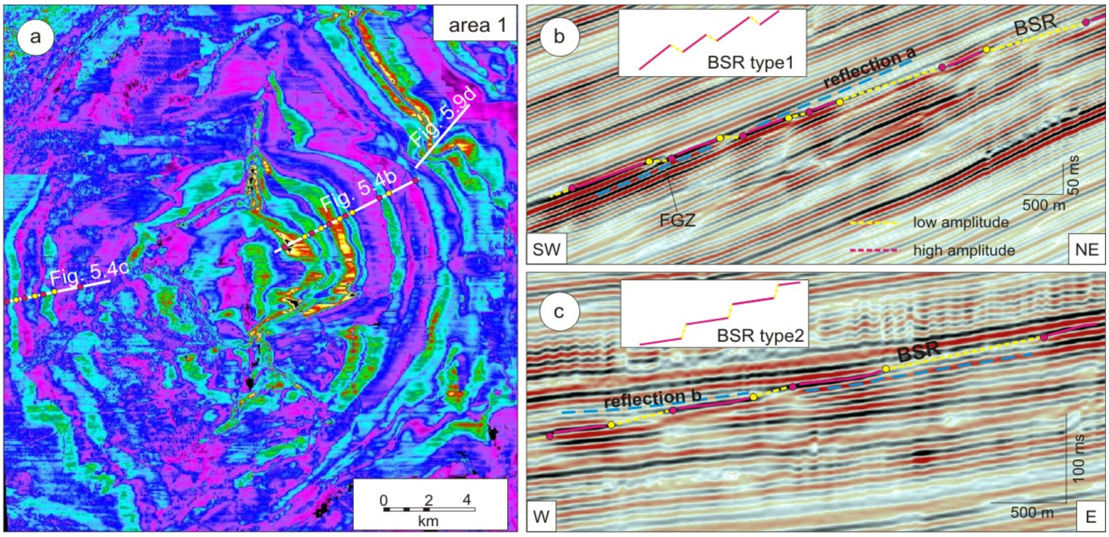

Fig. 5.4 (a): The amplitude map of the BSR in area 1. See figure 5.3 for location. (b): A seismic section cutting through the eastern side where the BSR is of lower apparent dip than the stratigraphy. (c): A seismic section cutting through the western side where the BSR is of steeper apparent dip than the stratigraphy.

5.3.1.2 Area 2

The amplitude map of the BSR in area 2 (Fig. 5.5a) shows curvilinear bands of high and low amplitude which bend seaward. There is no BSR developed in the white zone on the eastern side. The BSR intersects the seabed at ~ 880 ms in TWT time, and the amplitude bands of the BSR in area 2 generally follow the seabed contours (Figs 5.1b and 5.3). On seismic sections (Fig. 5.5bce) we observe an obvious BSR type 2, crosscutting stratigraphy of lower apparent dip. On sections b and e there are 3 and 7 high amplitude bands respectively (Fig. 5.5be). On seismic section c (Fig. 5.5c) the BSR does not form in the middle part where the reflections have very low amplitude, and no BSR can be observed on seismic section d (Fig. 5.5d). In this area the high amplitude reflections below the BSR are not obvious and

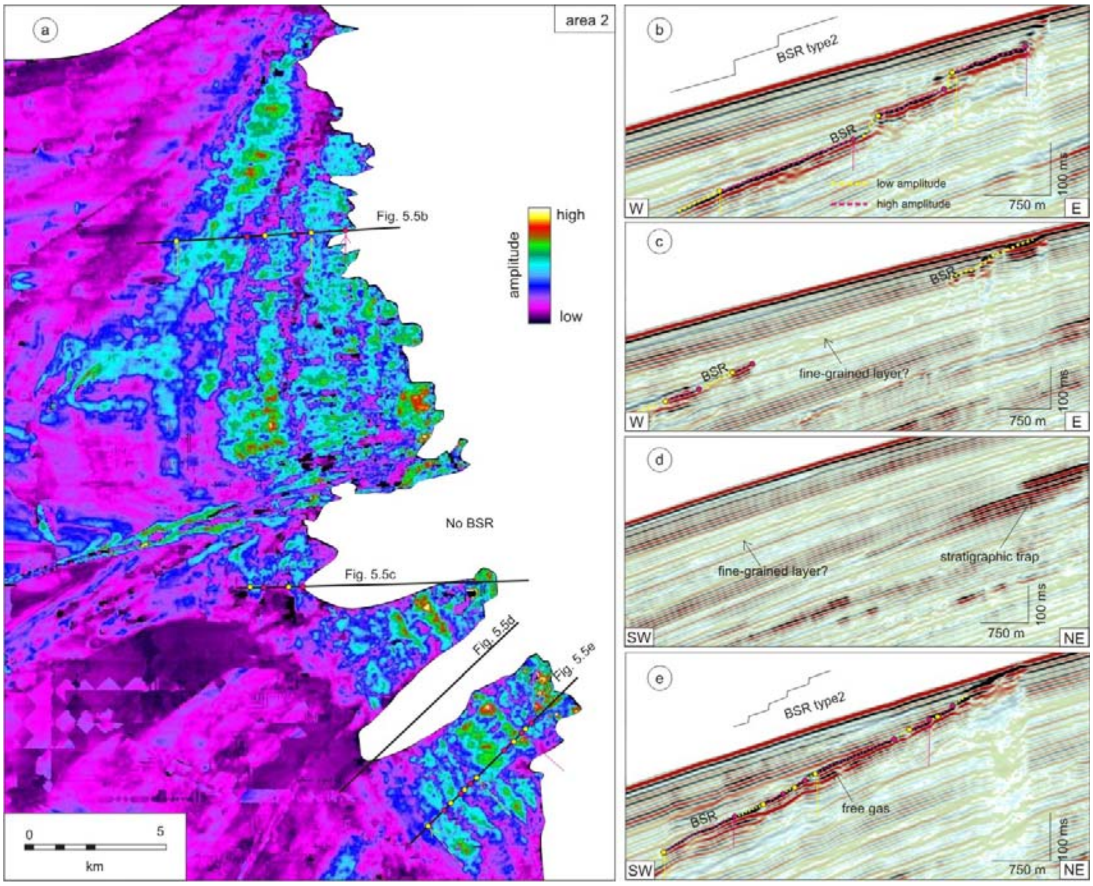

Fig. 5.5 (a): The amplitude map of the BSR in area 2. See figure 5.3 for location. The eastern boundary of the amplitude map is the intersection line of the BSR and the seabed, showing the landward limit of the GHSZ on the offshore Mauritanian continental margin. There is no BSR developed in the blank area in white. (b-e): Seismic sections showing the relationship between the BSR and stratigraphy.

often located in very thin zones, confined by low amplitude reflections on the updip sides (Fig. 5.5).

5.3.1.3 Area 3

The curvilinear amplitude bands in area 3 (Fig. 5.6a) are different from those in areas 1 and 2 for their locations and bending directions. These amplitude bands are mainly located

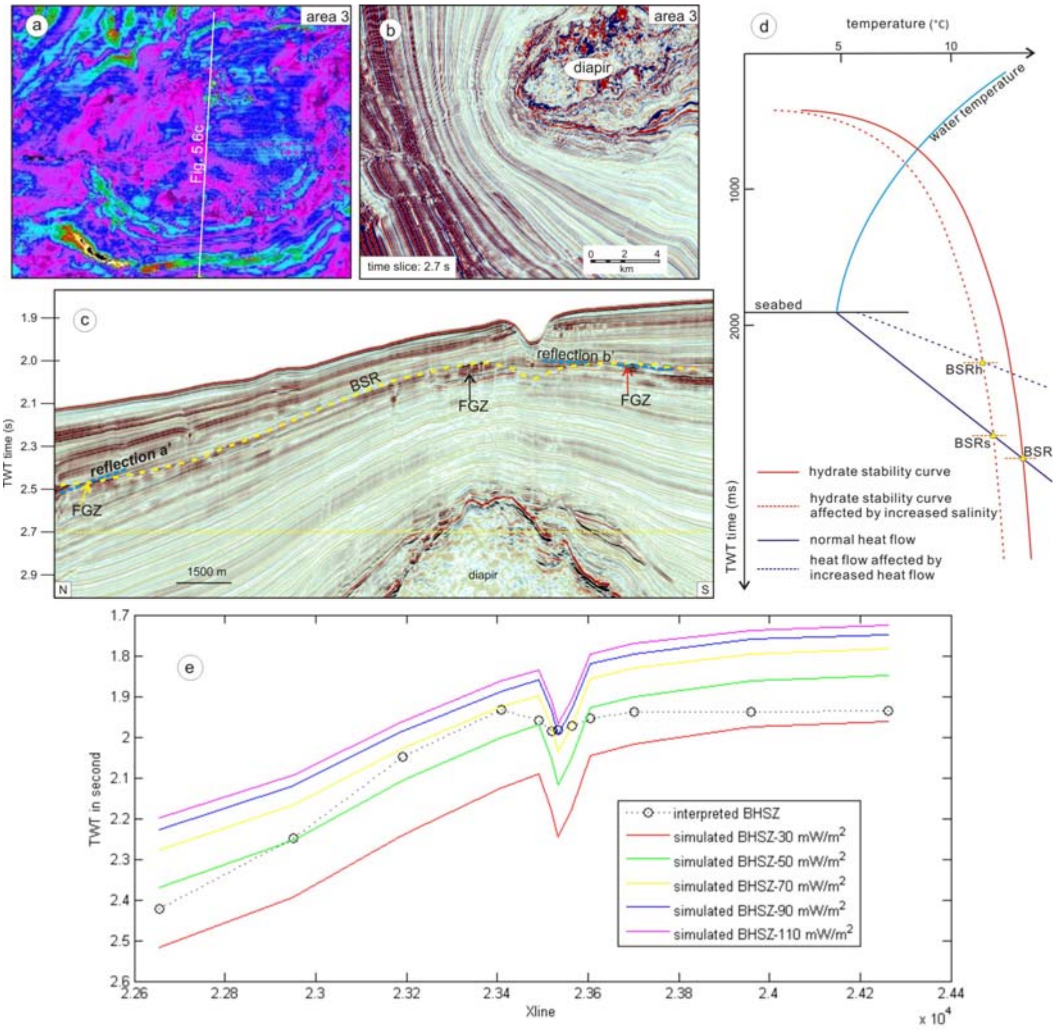

Fig. 5.6 (a): The amplitude map of the BSR in area 3. See figure 5.3 for location. There are alternating bands of low and high amplitude surrounding this diapir. (b): A time slice (2.7 s) was taken from the 3D seismic amplitude volume, showing the location of the diapir. (c): A seismic section (inline: 12340) showing the relationship among the BSR, stratigraphy and the diapir. (d): A phase diagram showing the effect of salinity on BSR location. The BSR gets shallower as the salinity increases or the heat flow increases. (e): Comparison of the modelled BSR (with different heat flow values) with the interpreted BSR (discussed in section 5.4).

in the south of area 3, surrounding a circular area of low amplitude. A time slice (Fig. 5.6b) taken at 2.7 seconds from the 3D seismic amplitude volume shows the location of a diapir, suggesting that the amplitude bands of the BSR surround this circular diapir. The seismic section (Fig. 5.6c) shows a up-domed BSR above a diapir and we observe three zones of high amplitude reflections sealed below the BSR. The BSR on the two wings of the diapir is of lower apparent dip than the up-domed strata (reflections a' and b'; BSR type 1), and the BSR in the south of this area is located much deeper, ~ 2.5 s (the yellow arrow) (Fig. 5.6c).

5.3.1.4 Area 4

In area 4 there is another diapiric structure (Fig. 5.7) located at a shallower depth than the salt diapir in area 3. It is a mud diapir characterized by low amplitude and typical 'Christmas tree' features related to the mud flow deposits (Milkov, 2000; Kopf, 2002). On seismic sections we observe that the BSR is much more up-domed along the short axis of the mud diapir, in W-E direction (Fig. 5.7bc). Below the BSR there are high amplitude reflections, especially beneath the crest of the up-domed BSR. The amplitude map shows that a linear feature in the middle separates the high amplitude into two zones (Fig. 5.7a). On a seismic section we observe that this linear structure is a buried canyon running from east to west (yellow triangle) (Fig. 5.7b). In the northern zone, we observe clear amplitude bands on the eastern side where the BSR is of steeper apparent dip than the stratal reflections and these amplitude bands bend away from the crest (BSR type 2) (Fig. 5.7ac). In the southern zone, there is no obvious amplitude band (Fig. 5.7a).

In the south eastern corner of area 4 there is a small zone of comparatively high amplitude (Figs 5.7a and 5.8a). The amplitude bands are twisted along a curvilinear line (yellow line) (Fig. 5.8a). On a seismic section cutting through this axis we observe a deeply rooted normal fault below the BSR (Fig. 5.8b). To study the location of this fault, we interpreted a reflection locally (reflection 1) (Fig. 5.8b). The apparent dip map of this reflection shows that this fault is spatially consistent with the yellow curvilinear line on the amplitude map (Fig. 5.8ac).

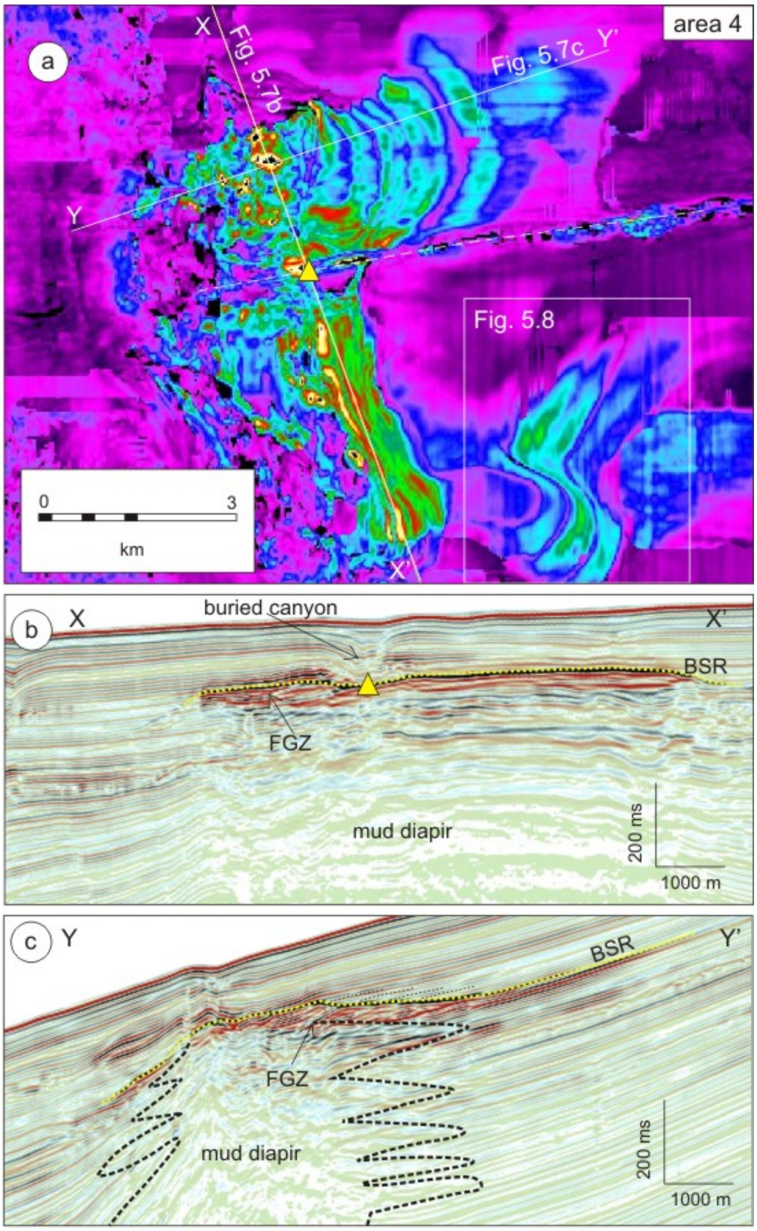

Fig. 5.7 (a): The amplitude map of the BSR in area 4, separated into two parts by a linear structure. There are alternating bands of low and high amplitude on the updip side of the mud diapir on the northern side. See figure 5.3 for location. (b): A seismic section along the long axis of the mud diapir, showing the relations of the BSR, FGZ, and the mud diapir. The location of the buried canyon is indicated by a yellow triangle. (c): A seismic section across the short axis of the mud diapir.

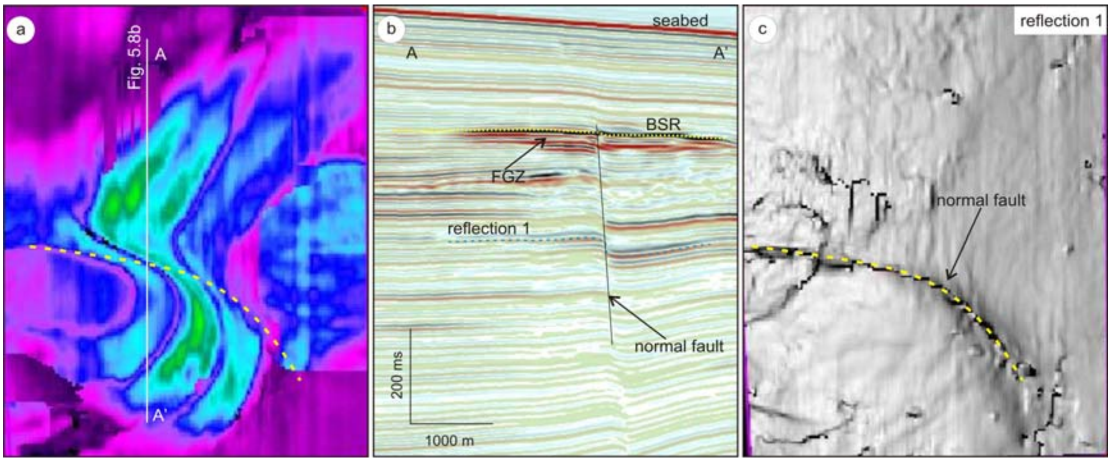

Fig. 5.8 (a): Zoom in image of part of the BSR amplitude map in area 4. The high amplitude bands are twisted along a curvilinear axis in the middle. See figure 5.7 for location. (b): A seismic section cutting through the high amplitude bands, showing the BSR, FGZ, and a normal fault. (c): Apparent dip map of reflection 1, showing the location of the normal fault.

5.3.1.5 Area 5

In area 5 the amplitude map (Fig. 5.9a) shows that the amplitude bands of the BSR shift seaward at a deep-water canyon. On a seismic section cutting through this canyon we observe that the BSR deepens significantly when it gets close to the canyon wall (Fig. 5.9b). There are a number of high amplitude reflections which terminate ~ 500 m from the canyon margin, confined laterally by the deepening BSR. Another seismic section parallel to the canyon shows a BSR type 2 of alternating high and low amplitude (Fig. 5.9c). Another similar phenomenon has also been observed on the north eastern side of area 1 where the BSR bands have an along-strike deflection and convergence (Fig. 5.4a; Davies et al., 2012a). A seismic section shows that the BSR shifts downward below the canyon and there are high amplitude reflections below the BSR (Fig. 5.9d).

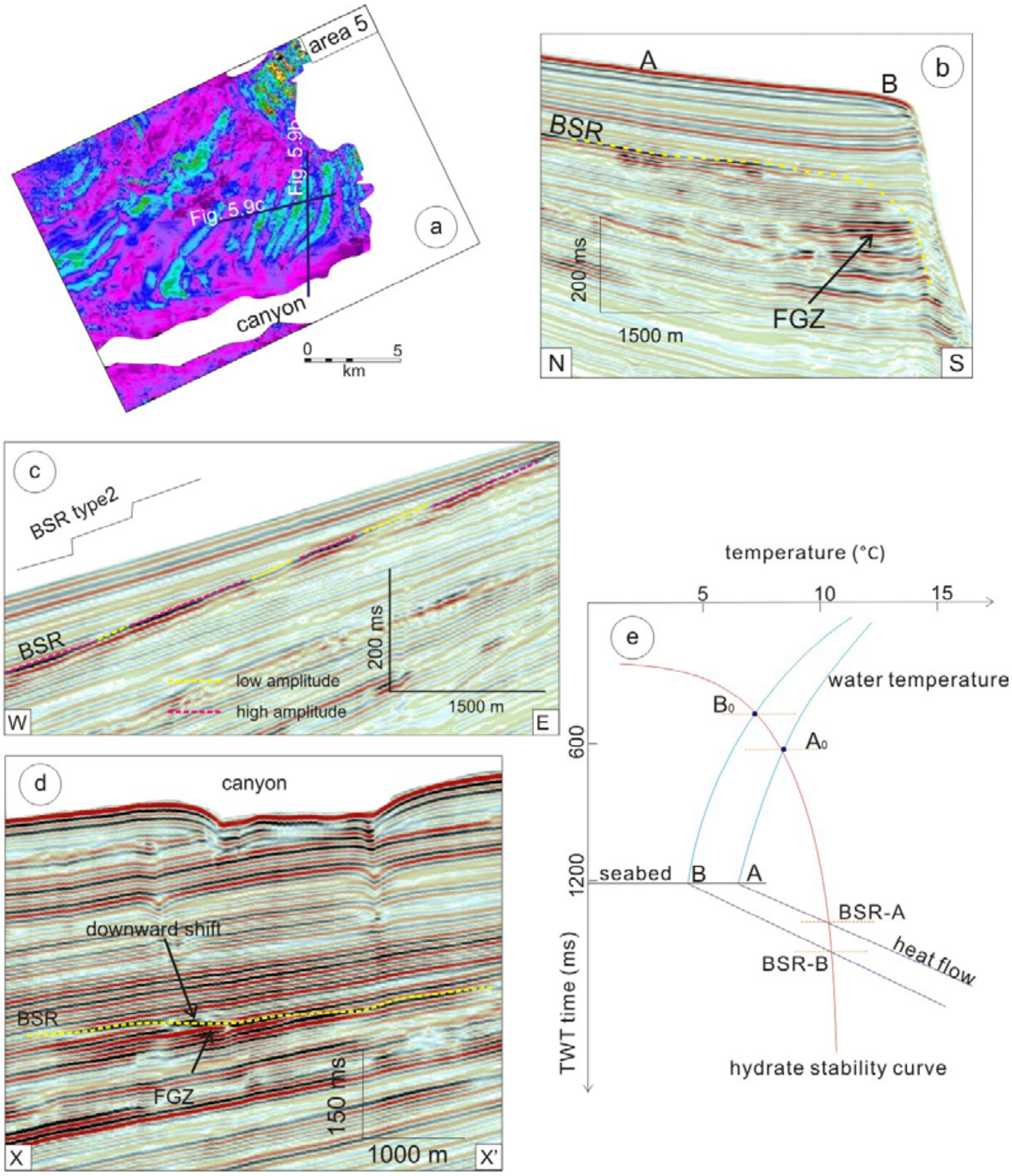

Fig. 5.9 (a): The amplitude map of the BSR in area 5, showing alternating bands of low and high amplitude. See figure 5.3 for location. (b): A seismic section from north to south, showing the downward shift of the BSR around a canyon. (c): A seismic section cutting through the amplitude bands and parallel to the canyon, showing a normal stair-like BSR type. (d): A seismic section from area 1, showing the downward deflection of the BSR below a canyon. See figure 5.4a for location. (e): A phase diagram showing the cooling effect of a canyon on surrounding sediments, causing downward shift of the BSR.

In addition to these five areas, we study another high amplitude band on the northern side of the amplitude map between areas 1 and 2 (Fig. 5.10a). This high amplitude band is ~ 10 km long, in W-E direction. Two seismic sections through this band (Fig. 5.10bc) show a downward shift of the BSR which is consistent with the northern boundary of the high amplitude band in map view (Fig. 5.10a). Below the seabed there is interval decreasing above the shifting points of the BSR, probably due to slope failure or reduction of sedimentation (Fig. 5.10bc).

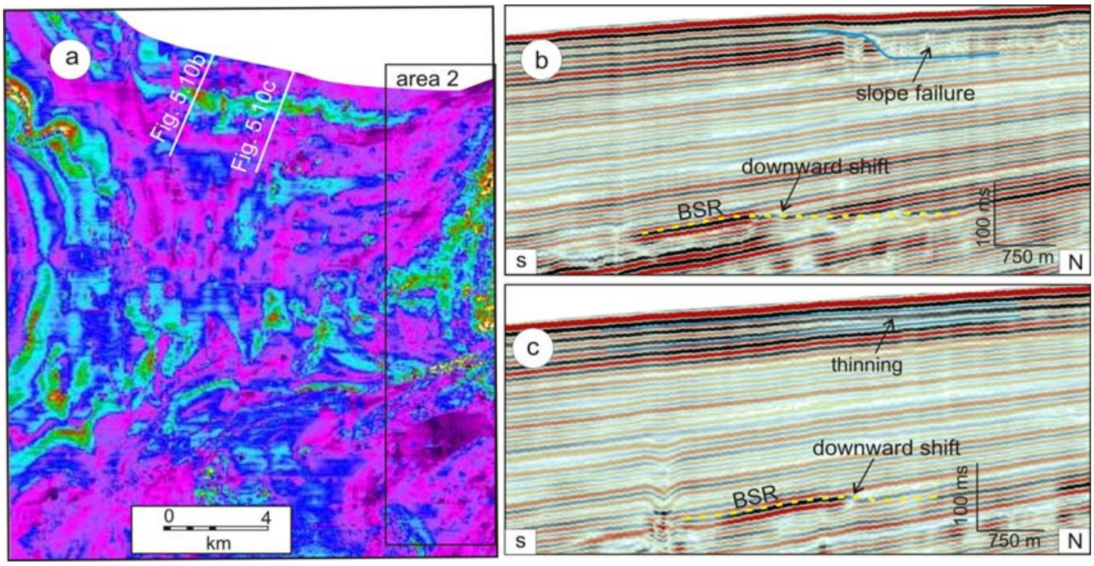

Fig. 5.10 (a): Part of the BSR amplitude map showing a high amplitude band on the northern side, in an East-West alignment. See figure 5.3 for location. (b): A seismic section showing the downward shift of BSR and above slope failure body. (c): A seismic section showing the downward shift of BSR and related decreased interval below the seabed.

5.3.2 High amplitudes below the BSR

To study the high amplitude reflections below the BSR, we generated a root-mean-square (RMS) amplitude extraction map within a window between the BSR and 50 ms below (Fig. 5.11a). This RMS map shows that high amplitude mainly occurs on the eastern side of area 1 and area 4, while in other areas the RMS amplitude map is featured by middle or low amplitude. In area 2, seismic sections also show some high amplitude reflections below the BSR, often in a thin zone (Figs 5.5be and 5.11b). And on the updip side of these high amplitudes are reflections of very low amplitude. In area 5, there are also zones of high amplitude reflections which terminate at the deepening BSR (Fig. 5.9b). But because the mapping window is narrow, only from the BSR to 50 ms below, the high amplitude reflections are not located within this window. Therefore the RMS amplitude map does not show these high amplitude reflections near the canyon wall in area 5.

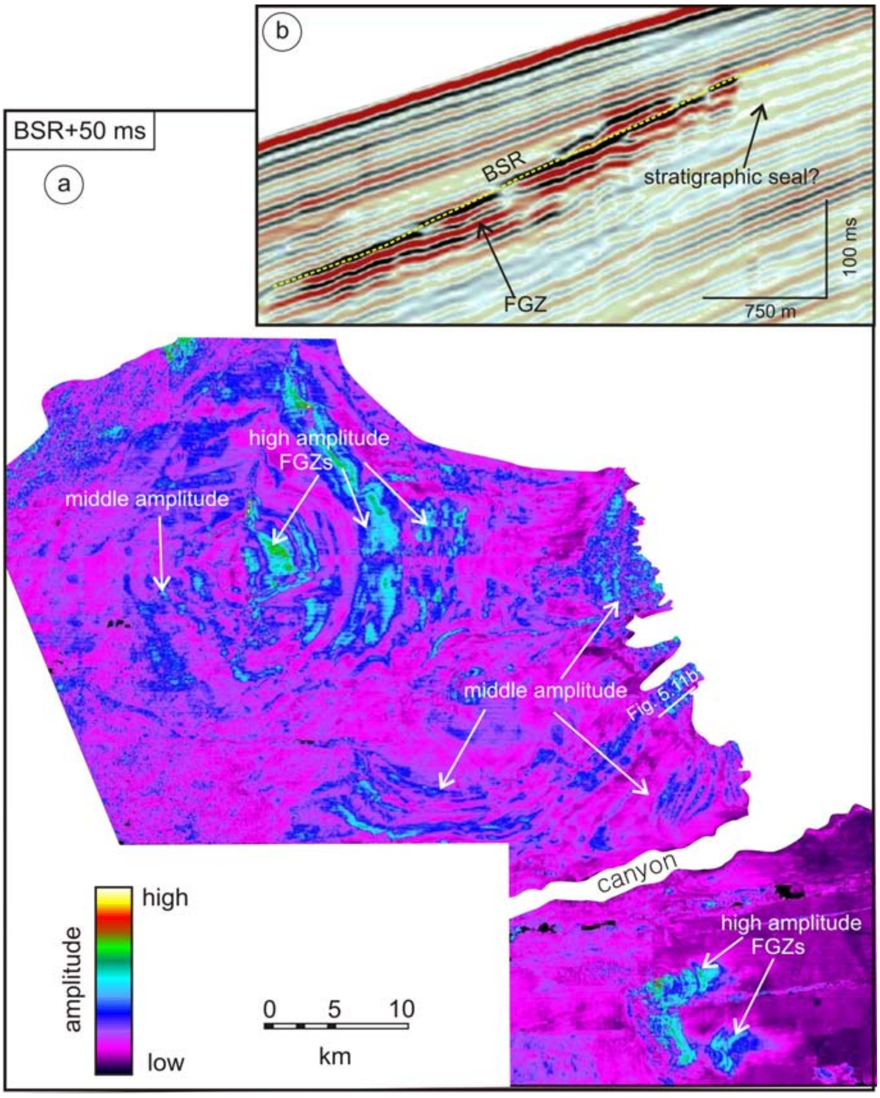

Fig. 5.11 (a): The RMS amplitude extraction map which is generated within a window between the BSR and 50 ms below, showing the location of high amplitude FGZs. (b): A seismic section showing the location of the BSR and a FGZ, and this FGZ is interpreted to be stratigrahpicly sealed on the updip side by impermeable layers.

5.4 Modelling

The location of BSR below the seabed is mainly caused by pressure and temperature conditions (Field and Kvenvolden, 1985; Brown et al., 1996). To estimate the heat flow in this area, we model the BSR locations under different heat flow values and compare with our observation. According to Makogon (1997), the relation between equilibrium temperature (T_e) and pressure (P_e) is:

$$\mathrm{Log}_{10} P_e = aT_e^2 + bT_e + c \qquad \text{Eq. 5.1}$$

where P_e is in Pa and T_e is in °C, and a, b and c are empirical constants that depend on hydrate composition. Here hydrate stability curve of pure methane is used and the following values are obtained to fit to the equilibrium P-T data:

$a = 0.000309\ °C^{-2}$, $b = 0.040094\ °C^{-1}$ and $c = 0.478626$.

Since the BSR is located shallow below the seabed, the pore pressure in the sediments at the BSR is assumed to be hydrostatic and equilibrium pressure at the BSR can be calculated as (Makogon, 1997; Sloan, 1998):

$$P_e = \rho_{sw}\ g\ h_{bsr} \qquad \text{Eq. 5.2}$$

where seawater density $\rho_{sw} = 1028$ kg m^{-3}, gravitational acceleration $g = 9.81$ m s^{-2} and h_{bsr} is the depth of the BSR below the sea level in m.

The temperature of the seabed (T_{sb}) can be derived from the World Ocean Database, and the temperature at the BSR (T_e) can be calculated as (Makogon, 1997; Sloan, 1998):

$$T_e = T_{sb} + q\ (h_{bsr} - h_{sb})\ k \qquad \text{Eq. 5.3}$$

where q is heat flow in mW m^{-2}, k is the thermal conductivity, ~ 10^{-3} m °C mW^{-1}, and h_{sb} is the seabed depth of the seabed in m which can be calculated from the TWT time using the average seismic velocity of sea water, ~ 1450 m s^{-1} (Davies et al., 2012b). Based on the three equations above, the depth of the BSR (h_{bsr}) under different heat flow values can be calculated and converted back to TWT time.

The heat flow can be estimated by fitting the model to the observed BSR. The heat flow in areas 1 and 2 is estimated to be 37 mW m^{-2}, which increases to 50 mW m^{-2} as the seabed gets deeper (Fig. 5.2c). In area 3 the heat flow value increases towards the salt diapir, especially on the southern side, changing from 50 mW m^{-2} to 70 mW m^{-2} (Fig. 5.6e). Salinity is not considered here. Above the crest of the diapir, there is a canyon which seems to have affected the BSR probably due to the cooling effect (Fig. 5.6ce).

5.5 Interpretation

Based on the strong reflection and negative polarity, we interpret the BSR to be hydrate-related, representing a phase transition from the hydrate-bearing sediments above the BSR to the underlying free gas-charged sediments (Field and Kvenvolden, 1985; Berndt et al., 2004). The alternating high- and low-amplitude sections of the BSR on seismic sections are consistent with the alternating bands of high and low amplitude on the amplitude map. The amplitude of the BSR is probably determined by the presence or absence of free gas trapped below the base of gas hydrates, controlled by the regularly spaced beds of coarser and finer sediments.

The high amplitude reflections below the BSR are interpreted to be caused by free gas in FGZs due to their locations and the negative polarity of the BSR. The RMS amplitude map shows the distribution of the FGZs which mainly occur on the eastern side of area 1 and in area 4 (Fig. 5.11a). The middle or low amplitude on the RMS map is probably caused by thin FGZs or the absence of FGZ.

5.6 Discussion

5.6.1 Distribution of the BSR

The BSR depth below the seabed is controlled by the hydrate stability conditions such as P-T, salinity, gas composition, or subsurface heat flow (Shipley et al., 1979; Sloan, 1998; Bünz et al., 2003). Seabed depth (pressure) and temperature are two basic parameters often used in the phase diagram to model the location of the BSR which is defined by the intersection of the heat flow profile and hydrate stability curve (Fig. 5.2b; Tucholke et al., 1977; Bünz et al., 2003). It is widely accepted that BSRs are mostly caused by the underlying free gas in FGZs which can cause the reduction of velocity, forming a higher acoustic impedance contrast (Taylor et al., 2000; Berndt et al., 2004). However sometimes there is no FGZ below the BSR, such as on the western side of area 1. That is probably related to the angle relationship between the BSR and stratal reflections. The BSR is steeper than the stratal reflections here, so the gas below the BSR will migrate laterally to the updip if there is no seal inhibiting the lateral escape of gas. Since a low saturation of free gas may cause the formation of BSR (Berndt et al., 2004; Yang and Davies, 2013), it is possible that this BSR is caused by some relict free gas below the BSR which has not escaped yet. However we cannot rule out the possibility that the BSR in this conditon is caused by diagenesis due to the existence of hydrates (Matsumoto,1989; Posewang and Mienert, 1999; Davies et al., 2012a).

On a regional seismic section through areas 1 and 2 (Fig. 5.2), the BSR depth gets shallower as the seabed depth decreases. From D to A, water temperature increases as the seabed depth decreases and the heat flow does not change (Fig. 5.2). As a result the BSR depth decreases from D to A, determined by the intersection of the heat flow profile and gas hydrate stability curve (Fig. 5.2b). On the phase diagram we see that the intersection depth of the BSR and the seabed (point A) is independent of the heat flow, but controlled by intersection of the water temperature profile and hydrate stability curve (Fig. 5.2b). Here the BSR offshore Mauritania intersects the seabed at ~ 880 ms in TWT time, which is ~ 640 m in depth assuming a water velocity of 1450 m s^{-1} (point A) (Fig. 5.2; Davies et al., 2012b). Studies in Gulf of Mexico (Cooper and Hart, 2002) and the Yaquina Basin off Peru (Hübscher and Kukowski, 2003) show that the BSRs in both areas intersect related seabeds at ~ 600 m. However on the West Spitsbergen continental margin the BSR intersects the seabed at a depth of ~ 400 m (Westbrook et al., 2009), which is much shallower than the intersection depths we introduce above. That is probably because of its high latitude, ~ 78° N, where the water temperature should be colder, which leads to a comparatively shallower intersection depth of the water temperature profile and the hydrate stability curve (from A_0 to B_0) (Fig. 5.9d; Mark et al., 1995).

There are two diapiric structures (salt and mud) in the study area (areas 3 and 4), above which the BSR is up-domed (Figs 5.6 and 5.7; Vear, 2005). Comparison of the two diapirs shows that the BSR is much more affected by the shallower one probably due to the distance between BSR and diapir. Although only seismic reflection data are available here, some factors associated with diapirism have been proposed previously which may affect the location of the BSR, such as diapir-related faults, increased pore water salinity (salt diapir), and increased heat flow above the diapirs (Schmuck and Paull, 1993; Taylor et al., 2000). The faults caused by diapirs can act as fluid pathways which allow upward gas migration to hydrate systems, and the gas may even vent to the seabed along active fault planes (Schmuck and Paull, 1993). Theoretically the pore water salinity increases above salt diapirs which may inhibit the formation of gas hydrates and shifts the gas hydrate stability to lower temperatures (Fig. 5.6d; Sloan, 1998; Taylor et al., 2000). The heat flow also increases due to high thermal conductivity or advective heat transport (Fig. 5.6d; Taylor et al., 2000). As a result changes in both salinity and heat flow caused by diapirs can cause the up-domed shape of the BSR (Fig. 5.6). Additionally gas composition may be contaminated by heavier hydrocarbons or carbon dioxide transported by diapir-related conduits from below, causing the deepening of the BSR (Tucholke et al., 1977; Clayton et al., 1997). However we observe up-domed BSRs above both diapirs here, probably indicating that compared to the combined effect of salinity and heat flow, the role of heavier gas in shifting the BSR may be negligible (e.g. Schmuck and Paull, 1993). However we cannot decide whether salinity or heat flow is the dominate factor in causing the up-domed BSR due to the lack of the heat flow measurements and pore water composition data.

In area 5, the BSR deepens significantly when it gets close to the canyon wall, probably caused by the incision of canyon which has a cooling effect on surrounding sediments (Hickey, 1997; Davies et al., 2012b). The seabed temperatures at different localities near this canyon are different due to their related distances to the canyon, colder at site B than site A. Providing the heat flow does not change, the BSR deepens from site A to B as shown in the phase diagram (Fig. 5.9d). Similar phenomena have also been observed at Dnieper Canyon of north western Black Sea and offshore southwestern Japan where the downward shift of BSR is probably the result of both erosion (seabed decrease) and cooling effect of the depression incision (Lüdmann et al., 2004; Bangs et al., 2010).

Outside these 5 areas, there is a band of high amplitude in the north part between areas 1 and 2, in W-E direction (Fig. 5.10). The BSR shifts downward below a layer thinned by a slope failure or sedimentation reduction, which confines the northern boundary of the amplitude band (Fig. 5.10bc). The decrease of the interval is approximately equivalent to seabed deepening and canyon incision, shifting the BSR downwards (Figs 5.2d and 5.9d). The southern boundary of the amplitude band is probably related to the distribution of a gas accumulation which may be transported from below by fluid migration conduits like chimneys (Fig. 5.10c).

Generally any changes in hydrate stability conditions, such as P-T, salinity, and gas composition, may affect the distribution of gas hydrates, shifting the BSR downward or upward. These changes mainly occur during processes like sedimentation, diapirism, or bottom water temperature change. However the hydrate stability conditions are not responsible for the specific geometry of the BSR, and the detailed controlling factors of the BSR geometry will be discussed in the following section.

5.6.2 Geometry of the BSR

Successful seismic imaging of the BSR is a function of frequency matching of the thickness of the FGZ and the dominant wavelength of the seismic data (Vanneste et al., 2001; Mosher, 2011). Continuous BSRs of strong amplitude and negative polarity can be interpreted primarily on low frequency data from areas with homogeneous sediments and pervasive and diffusive gas flux (Vanneste et al., 2001; Shedd et al., 2012). Discontinuous BSRs, which have also been termed as segmented BSRs or shingled BSRs, mainly occur on medium to high frequency data because the amplitude and continuity of the BSR are determined by the vertical and horizontal resolutions of the seismic data (Vanneste et al., 2001; Navalpakam et al., 2012; Shedd et al., 2012). The discontinuous high amplitude sections of the BSRs are expressed as the updip termination of the FGZ, probably caused by the patchy distribution of the free gas below the BSR (Vanneste et al., 2001; Navalpakam et al., 2012). According to Mosher (2011), industry seismic data are ideal to recognize BSRs, especially when they crosscut stratal reflections at an acute angle. So in this chapter we rely on the high resolution 3D seismic data offshore Mauritania to investigate the geometry of the BSR.

Here the interpreted BSR consists of segmented sections of high amplitude and it has a discontinuous shape when we connect the high amplitude sections during seismic interpretation. High amplitude sections along the BSR represent higher acoustic impedance contrasts, probably due to the presence of free gas (Berndt et al., 2004; Laird and Morley,2011). The low amplitude sections along the BSR are picked by the interpreter or auto-picking to connect the high amplitude sections. They do not represent a phase boundary but indicate lower or zero acoustic impedance contrasts probably due to the in situ fluid and lithology characteristics (Laird and Morley,2011). According to previous studies, lithology is a major factor controlling the distribution of gas hydrates and gas (Henry et al., 1999; Bünz et al., 2003; Rodrigo et al., 2009; Malinverno, 2010). Case studies of gas hydrates occurring in porous coarse-grained sediments have been observed on the Cascadia margin (Weinberger et al., 2005; Malinverno, 2010) and offshore India (Collett et al., 2008). Gas hydrates mainly occur in porous coarse-grained sediments where hydrates grow within the pores and cement the grains, changing the physical properties of the sediments (Pearson, 1983; Clennell et al., 1999). In fine-grained sediments, hydrate formation is inhibited due to the reduced pore water activity in the vicinity of hydrophilic mineral surfaces and the excess internal energy of small crystals confined in pores (Ginsburg, 1998; Clennell et al., 1999). Additionally gas is also inhibited to enter fine-grained sediments due to the high capillary entry stress caused by the small pore size (Sylta, 2005). So although no well information is available here, we propose that the alternating amplitude change of the BSR here is probably caused by presence or absence of free gas trapped below the base of gas hydrates, which is probably controlled by the regularly spaced beds of coarser and finer sediments (Vear, 2005; Krastel et al., 2006).

In map view the amplitude bands bend toward different directions, probably due to the 3D intersection of the BSR and stratal reflections (Fig. 5.3). The amplitude bands are confined by many intersection lines of the BSR crosscutting different sedimentary layers of coarser and finer sediments (Davies et al., 2012a). In areas 1 and 2, both stratigraphy and the BSR dip seawards, and the amplitude bands of the BSR bend to two opposite directions (Figs 5.4 and 5.5). For BSR type 1, the amplitude bands bend landward to the updip side (e.g. on the eastern side of area 1) (Fig. 5.4). For BSR type 2, the amplitude bands bend seaward to the downdip side (e.g. on the western side of area 1 and in area2) (Figs 5.4 and 5.5). In area 2, we observe more high amplitude bands on section e than on section b (Fig. 5.5abe), which is probably caused by the different thicknesses and frequency of the sedimentary layers crosscut by the BSR. In diapiric areas the amplitude bands are semi-circular surrounding the diapirs, also controlled by the intersection of the BSR and stratal reflections (areas 3 and 4) (Figs 5.6 and 5.7). In area 5 where a canyon develops, the amplitude bands deflect downslope to lower temperature zones due to the cooling effect of the canyon (Davies et al., 2012b). So the amplitude bands in these five areas are all controlled by the 3D intersection of the BSR and stratigraphy.

5.6.3 Free gas zones (FGZs)

According to Tucholke et al. (1977), structural peculiarities of the BSR and stratigraphy are prerequisites to the formation of FGZs. When the BSR is of lower apparent dip than the stratigraphy, free gas can be trapped below the BSR, forming a FGZ (the eastern side of area 1) (Fig. 5.4b; Tucholke et al., 1977; Laird and Morley, 2011). When the BSR and stratigraphy both dip towards the same direction and the BSR is steeper than the stratigraphy, updip gas migration is unhindered and no FGZ can form below the BSR (the western side of area 1) (Fig. 5.4c; Tucholke et al., 1977). However in area 2 where the BSR is steeper than stratigraphy, we also observe some thin FGZs (Figs 5.5 and 5.11). They are probably trapped in combination traps, hydrate-sealed vertically and stratigraphy-sealed on the updip side by fine-grained sediments, indicated by the weak seismic reflections. In the two diapiric areas, FGZs can form under the up-domed BSR regardless of the angle relationship between BSR and stratigraphy (Figs 5.6 and 5.7). At the canyon wall in area 5, the BSR shifts downwards and the FGZ can be sealed by the base of gas hydrates both vertically and laterally (Fig. 5.9). The RMS amplitude extraction map (Fig. 5.11a) shows that FGZs are not uniformly distributed below the BSR, but also characterized by amplitude bands (Fig. 5.3). That is probably because of the 3D distribution of the FGZs which is controlled by the sediment lithology.

5.7 Controls on the base of gas hydrates

The schematic diagram (Fig. 5.12) explains the roles of sediment lithology and angle relationship between the BSR and stratigraphy in controlling the amplitude characteristics of the BSR and FGZ location. On seismic sections the predicted BSR is a continuous reflection which crosscuts the stratigraphy (orange line) (Fig. 5.12ab). The interpreted BSR is composed of a number of sections of high amplitude, when connected, forming a discontinuous geometry of alternating high and low amplitude. Here we assume a seismic-scale sequence of alternating sedimentary layers of higher and lower porosities. However, at core scale the layers in this diagram can be divided into more layers of only a few metres thick (inset core records) (Fig. 5.12). The high amplitude sections of the BSR represent higher acoustic impedance contrasts which are controlled by the presence of free gas at the depth of the predicted BSR (Fig. 5.12ab). It is proposed that the high amplitude sections of the BSR mainly occur in coarser sedimentary layers such as the turbidite deposits, indicating a transition from hydrate- to free gas-charged coarser sediments or from finer sediments to free gas-charged coarser sediments (Fig. 5.12ab; Henrich et al., 2010). The low amplitude sections are used to connect the high amplitude sections, representing lower or zero acoustic impedance contrasts. They are proposed to be mainly located in sedimentary layers of lower porosity where the occurrence of gas hydrates and free gas is inhibited (Fig. 5.12ab; Clennell et al., 1999; Henrich et al., 2010).

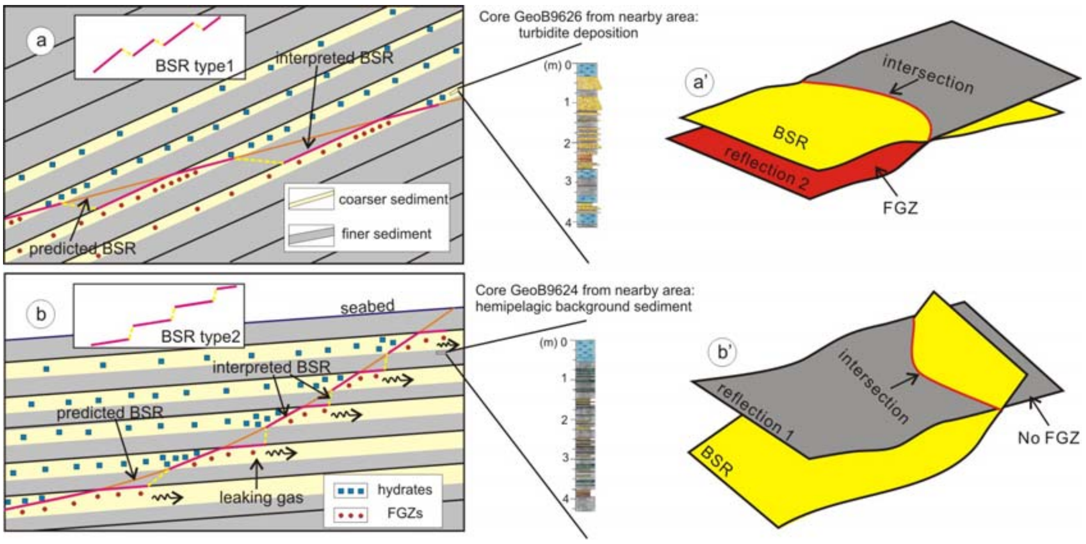

Fig. 5.12 (a, b): Formation mechanisms of the two types of stair-like BSRs on cross sections. Pale yellow colour indicates coarser-grained sediment while grey colour indicates finer-grained sediment. Blue rectangles represent hydrates and red circles represent free gas. Cores GeoB 1926 and 9624 are from nearby Timiris Canyon area which display turbidite deposition and hemipelagic background sediment (from Henrich et al., 2010). (a', b'): A 3D model showing the intersection of the BSR and stratigraphy which controls the bending directions of BSR amplitude bands and the location of FGZs. Yellow colour represents the BSR surface; grey colour represents a stratigraphic surface; red colour represents a FGZ.

The angle relationship between the BSR and stratigraphy also affects the BSR characteristics and FGZ location, based on which the BSR is divided into two types (Figs 5.12 and 5.13). Type 1 indicate the BSR which has a lower apparent dip than the stratal reflections, and the high amplitude sections of the BSR step downwards as corresponding seabed gets shallower (Fig. 5.12a). FGZs can form below the BSR and the plan-view amplitude bands of the BSR bend upslope (Fig. 5.12aa'). Type 2 occurs where the BSR has a steeper apparent dip than the stratal reflections with the high amplitude sections stepping upwards as corresponding seabed gets shallower (Fig. 5.12b). In this condition the free gas below the BSR will escape laterally to the updip side due to buoyancy and there is no FGZ formation. In map view the amplitude bands of the BSR bend downslope (Fig. 5.12b'). In this chapter it is exemplified that mapping the BSR can provide a wealth of information on lateral changes of the BSR at different depths from only one map (Fig. 5.13). It enables us to investigate the BSR characteristics and FGZ locations in different areas, and understand their specific controls.

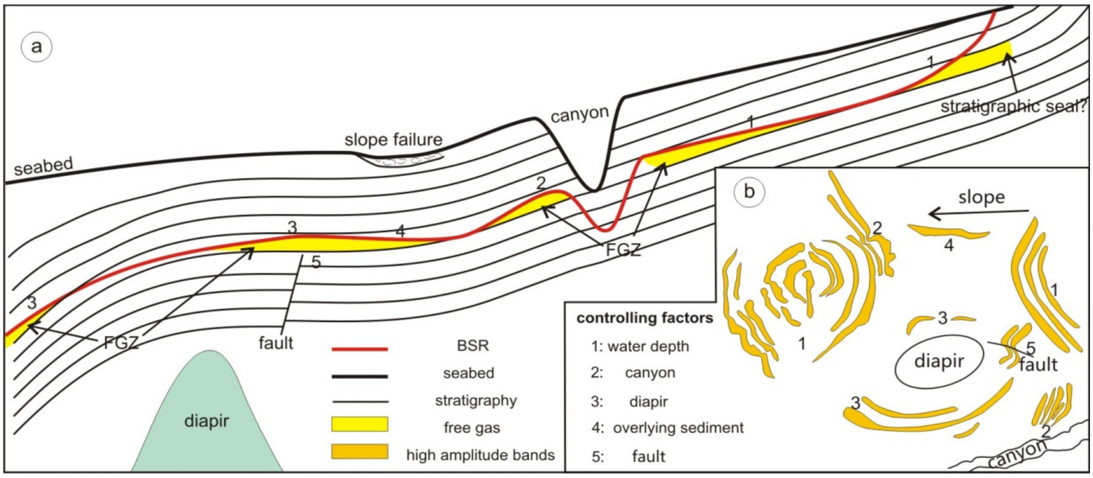

Fig. 5.13 (a): Illustration of a cross section from this area, showing the relationship between the BSR and stratigraphy, as well as the locations of FGZs. (b): Schematic BSR amplitude map of high amplitude bands in the study area, controlled by different factors.

5.8 Conclusions

In this chapter we studied the BSR characteristics and FGZ locations offshore Mauritania, where the hydrate stability is controlled by geological features such as water depth of the seabed, salt diapir, mud diapir and canyons. The BSR depth decreases as the seabed gets shallower in areas 1 and 2, vaults upwards above the crests of the two diapirs in areas 3 and 4 because of the changes in salinity and heat flow, and shifts downwards near the canyon in area 5 due to its cooling effect on surrounding sediments. The amplitude characteristics of the BSR are proposed to be related to sediment lithology because free gas which can cause the high amplitude of the BSR is preferentially held in coarser sediments. The bending directions of the amplitude bands of the BSR in map view are interpreted to be the result of 3D intersection of the BSR and stratigraphy, which may also affect the FGZ locations.

Previous seismic imaging of BSRs is mainly based on mapping stratal reflections crosscut by BSRs, through which one map can only display the BSR characteristics at one single depth. In this chapter we map the BSR rather than the stratal reflections, and the amplitude map of the BSR provides a wealth of information on lateral changes in the position of the base of gas hydrates. So mapping the BSR probably represents an efficient way to study gas hydrate systems, which should be applicable in other areas that have widespread BSRs and high-resolution 3D seismic data.

Chapter 6: Discussion and conclusions

This chapter summarizes the principal findings, introduces the uncertainties and presents some interesting topics for future work.

6.1 Principal findings

The 3D seismic dataset offshore Mauritania is of high quality, allowing for detailed mapping of the gas hydrate system. This thesis (Fig. 1.5) mainly focuses on hydrate-related gas migration processes (chapters 3 and 4) and investigates the geological controls on the bottom simulating reflection (BSR) distribution, BSR geometry and free gas zone (FGZ) locations (chapter 5).

Chapter 3 describes many localized high amplitude anomalies (HAAs) above some mass transport complexes (MTCs). These HAAs are divided into two populations, aligned and non-aligned, and both indicate gas migration up margin alignments or local faults associated with underlying MTCs. The upward fluid migration indicated by the HAAs was possibly caused by hydrate dissociation due to the upward resetting of the base of gas hydrates which would have occurred in response to sedimentation. However it is also possible that the fluid was from other sources such as the in situ generated biogenic gas, squeezed pore fluids from compaction or deep thermogenic gas, which needs further study using additional data.

Chapter 4 builds a model for gas recycling between gas hydrates and other gas traps, with gravity-driven faults as migration conduits for the released gas from hydrates dissociation. There are spatial relationships among the fault location, a breached gas accumulation and the location of a shallower FGZ sealed by hydrates. These are consistent with the upward-resetting of the base of gas hydrates. The released gas from hydrates migrated up the faults to either become trapped in a new FGZ or potentially recycled back into a hydrate phase.

The processes of upward gas migration described in chapters 3 and 4 indicate the dynamics of gas recycling between gas hydrates and other free gas traps on continental margins. The gas recycling process has seldom been described before and is poorly understood, which may also indicate a significant mechanism of gas supply to the shallower gas hydrates (Pecher et al., 1996; Haacke et al., 2007). Due to pulsed sedimentation or other processes, the gas hydrate zone resets upwards and the hydrates at the base of gas hydrate stability zone (BHSZ) dissociate, releasing a large volume of gas and water which may be overpressured. The overpressure can reactivate pre-existent structures such as headwall scarps of MTCs, faults or chimneys, allowing the released gas recycling upwards to the new hydrate zone. Since MTCs, faults and chimneys are common on continental margins where gas hydrates are expected to coexist, the model of gas recycling process along pre-existent structures should be generally applicable.

Chapter 5 uses a new seismic tool for the study of gas hydrates and FGZs. The BSR is mapped rather than chronostratigraphic reflections. The map of the BSR shows that the seismic amplitude of the BSR is not continuous but characterized by intervening high and low amplitude bands. The amplitude bands of the BSR are curvilinear and bend to different directions. The high amplitude of the BSR is interpreted to be caused by the presence of gas trapped below the base of gas hydrates in regularly spaced beds of coarser sediments. The amplitude map of the BSR provides evidence of lateral changes such as P-T conditions and salinity due to variable water depth of the slope, impingement of salt diapir and mud diapir, and canyon cutting at the seabed, which are responsible for the changes of BSR depth and amplitude. The base of gas hydrates often represents the top of FGZs. So the high amplitude bands on the map of the BSR may indicate possible locations of FGZs. Previously the description of FGZs is often based on the observation from cross sections. In chapter 5 a RMS amplitude map was generated within a window between the BSR and 50 ms below, showing the distribution of FGZs. Generally the study in chapter 5 exemplifies the potential of 3D seismic data in displaying the 3D complexity of the BSR and FGZs and mapping the BSR probably indicates an effective method to study gas hydrates.

6.2 Uncertainties

The research is based solely on interpretation of the 3D seismic data from offshore Mauritania which have been processed by post-stack time-migration. The absence of other additional data may hinder a better understanding of the gas hydrate system in this research.

In marine environments gas hydrates mainly occur at shallow depth below the seabed which is relatively well imaged on seismic data because the frequency content decreases as penetration depth increases due to attenuation of waves (Brown, 2010; Ireland, 2011). The 3D seismic data have a high vertical resolution of ~ 8.5 m, which can increase the confidence of seismic interpretation.

In this thesis, many localized high amplitude anomalies (HAAs) are interpreted to be caused by either free gas or gas-related diagenesis and the HAAs are regarded as the evidence of gas migration. Additionally the amplitude change of the BSR is hypothesized to be caused by the presence or absence of free gas related to the variable sediment porosity and lateral changes in the ambient hydrate stability conditions. To guarantee the accuracy of seismic interpretation, borehole data or reliable velocity data are required to aid the seismic interpretation (Bacon et al., 2007). At the Storegga Slide, Bünz and Mienert (2004) analyzed the P-wave velocity of an ocean-bottom cable (OBC) dataset to demonstrate the existence of gas hydrates and free gas. Some geotechnical data were also used to model the hydrate and gas concentrations, such as the porosity, water content, mineral constituents and organic carbon. These data can provide important constraints on seismic interpretation and help understand the details of the gas hydrate system. So although there is no well drilled in the study area, the availability of such additional data could improve the understanding of the gas hydrate system and related fluid migration processes accurately.

Furthermore the models built in the thesis are only based on one 3D seismic dataset from offshore Mauritania. Although they may represent significant processes of gas recycling below the BSR and describe extraordinary features of the BSR, more datasets are required to prove whether these models are generally applicable or not. Unfortunately only one 3D seismic dataset is available for this research.

6.3 Future work

Similar to conventional petroleum systems, gas hydrate reserves also involve a few prospect elements such as source, reservoir, seal, trap, timing and migration, which should be well understood before hydrate production (Mosher, 2011). So techniques used to explore and estimate conventional hydrocarbon reserves can also be used in hydrate research. The significance of gas hydrates has been repeatedly emphasized by many researchers, but a firm understanding of the details of gas hydrates requires additional multidisciplinary research. So many types of data are required to do detailed research on gas hydrates, such as seismic data, borehole data or pore water chemistry data. The following are some topics for my future work which probably need an analysis of high quality geophysical data, in particular well logs:

1) What are the gas sources of gas hydrates? Does the occurrence of gas hydrates rely on focused fluid migration? This should be carried out by seismic interpretation and analysis of borehole data, isotopic and compositional data. The relationship between hydrate occurrence and fluid migration pathways will suggest whether most of the gas hydrate systems are dependent of the focused fluid migration or the generation of in situ biogenic gas. If the formation of gas hydrates mainly depends on focused fluid migration, the concentration of gas hydrate may be larger near the focused fluid migration conduits.

2) How are the hydrated layers distributed in the subsurface? The presence of hydrate-related BSR only indicates the position of the base of gas hydrates. Very little is known about the details of gas hydrate layers, such as their thickness, hydrate saturation, the physical properties of hydrated sediments and the rate of hydrate dissociatin in natural envrionments (Rodrigo et al., 2009; Boswell et al., 2012). When these parameters are available, the reserve of gas hydrates can be estimated and the areas of economic hydrates can be detected for further development (Mosher, 2011).

3) What are the characteristics of the different hydrate reservoirs? The hydrate reservoirs can be classified into different types based on their thermodynamic conditions, hosting geological structures or trapping configurations. According to Lee and Collett (2011), the hydrate reservoirs in Gulf of Mexico can be classified into three types based on resistivity and velocity analysis: isotropic reservoirs in sands, vertical fractured reservoirs in shale and horizontally layered reservoirs in silty shale. Chen et al. (2006) classify the hydrate reservoirs into two types based on their gas supply mechanisms: diffusion hydrates and vent hydrates. A full

understanding of the characteristics of hydrate reservoirs will help further hydrate development.

6.4 Conclusions

- MTC margins and related faults are possible fluid migration pathways transporting fluid upward through the MTC succession, indicated by the spatially consistent HAAs above the alignments of MTC margins.
- The fluids responsible for the formation of MTC-related HAAs may be from hydrate dissociation due to the frequent upward resetting of the BSR although other sources cannot be ruled out.
- Gravity-driven faults can act as gas recycling pathways when hydrates dissociate and release a large volume of gas and water due to the upward resetting of the BSR.
- Released gas can migrate upwards along the faults which have higher permeability until it reaches the new position of the BSR. The gas can then be stored in a FGZ or form new hydrates.
- Mapping the BSR probably represents an efficient method to study gas hydrates, providing a wealth of information of the BSR characteristics and FGZ locations.
- This thesis exemplifies the potential of high resolution 3D seismic data to study the subsurface features.

References

A

Abrams, M.A., 1992, Geophysical and geochemical evidence for subsurface hydrocarbon leakage in the Bering Sea, Alaska: Marine and Petroleum Geology, v. 9, p. 208-221.

Andresen, K.J., Huuse, M., Clausen, O.R., 2008, Morphology and distribution of Oligocene and Miocene pockmarks in the Danish North Sea – implications for bottom current activity and fluid migration: Basin Research, v. 20(3), p.445-466.

Anderson, J.E., Cartwright, J., Drysdall, S.J., Vivian, N., 2000, Controls on turbidite sand deposition during gravity-driven extension of a passive margin: examples from Miocene sediments in Block 4, Angola: Marine and Petroleum Geology, v. 17(10), p. 1165-1203.

Andreassen, K., Hart, P.E., MacKay, M., 1997, Amplitude versus offset modeling of the bottom simulating reflection associated with submarine gas hydrates: Marine Geology, v. 137, no. 1-2, p. 25-40.

Antobreh, A., Krastel, S., 2007, Mauritania Slide Complex: morphology, seismic characterisation and processes of formation: International Journal of Earth Sciences, v. 96, p. 451-472.

B

Bacon, M., Simm, R., Redshaw, T., 2007, 3-D Seismic Interpretation, Cambridge University Press.

Bangs, N.L., Hornbach, M.J., Moore, G.F., Park, J.-O., 2010, Massive methane release triggered by seafloor erosion offshore southwestern Japan: Geology, v. 38, p. 1019-1022.

Bangs, N.L., Westbrook, G.K., 1991, Seismic modeling of the decollement zone at the base of the Barbados Ridge Accretionary Complex: Journal of Geophysical Research: Solid Earth, v. 96(B3), p. 3853-3866.

Benson, A.K., Wu, J., 1999, A modeling solution for predicting (a) dry rock bulk modulus, rigidity modulus and (b) seismic velocities and reflection coefficients in porous, fluid-filled rocks with applications to laboratory rock samples and well logs: Journal of Applied Geophysics, v. 41(1), p. 49-73.

Bernard, B.B., Brooks, J.M., Sackett, W.M., 1976, Natural gas seepage in the Gulf of Mexico: Earth and Planetary Science Letters, v. 31(1), p. 48-54.

Berndt, C., 2005, Focused fluid flow in passive continental margins: Royal Society of London Transactions Series A, v. 363, p.2855-2871.

Berndt, C., Bünz, S., Clayton, T., Mienert, J., Saunders, M., 2004, Seismic character of bottom simulating reflectors: examples from the mid-Norwegian margin: Marine and Petroleum Geology, v. 21, no. 6, p. 723-733.

Berndt, C., Costa, S., Canals, M., Camerlenghi, A., Mol, B., Saunders, M., 2012, Repeated slope failure linked to fluid migration: The Ana submarine landslide complex, Eivissa Channel, Western Mediterranean Sea: Earth and Planetary Science Letters, v. 319-320, p. 65-74.

Berndt, C., Mienert, J., Vanneste, M., Bünz, S., Bryn, P., 2002, Submarine slope-failure offshore Norway triggers rapid gas hydrate decomposition: Proceedings of the Fourth international Conference on Gas Hydrates, p. 71-74.

Boswell, R., Frye, M., Shelander, D., Shedd, W., McConnell, D.R., Cook, A., 2012, Architecture of gas-hydrate-bearing sands from Walker Ridge 313, Green Canyon 955, and Alaminos Canyon 21: Northern deepwater Gulf of Mexico: Marine and Petroleum Geology, v. 34(1), p. 134-149.

Brown, A., 2010, Interpretation of Three-Dimensional Seismic Data, seventh edition : Tulsa.

Brown, H.E., Holbrook, W.S., Hornbach, M.J., Nealon, J., 2006, Slide structure and role of gas hydrate at the northern boundary of the Storegga Slide, offshore Norway: Marine Geology, v. 229, p. 179-186.

Brown, K.M., Bangs, N.L., Froelich, P.N., Kvenvolden, K.A., 1996, The nature, distribution, and origin of gas hydrate in the Chile Triple Junction region: Earth and Planetary Science Letters, v. 139, p. 471-483.

Bruce, C.H., 1984, Smectite dehydration--Its relation to structural development and hydrocarbon accumulation in Northern Gulf of Mexico Basin: American Association of Petroleum Geologists Bulletin, v. 68, p. 673-683.

Bull, S., Cartwright, J., Huuse, M., 2009, A review of kinematic indicators from mass-transport complexes using 3D seismic data: Marine and Petroleum Geology, v. 26(7), p. 1132-1151.

Bünz, S., Mienert, J., 2004, Acoustic imaging of gas hydrate and free gas at the Storegga Slide: Journal of Geophysical Research, v. 109, B04102.

Bünz, S., Mienert, J., Berndt, C., 2003, Geological controls on the Storegga gas-hydrate system of the mid-Norwegian continental margin: Earth and Planetary Science Letters, v. 209, p. 291-307.

Bünz, S., Mienert, J., Bryn, P., Berg, K., 2005, Fluid flow impact on slope failure from 3D seismic data: a case study in the Storegga Slide: Basin Research, v. 17, p. 109-122.

C

Carpenter, G.B., 1981, Coincident sediment slump/clathrate complexes on the U.S. Atlantic slope, Geo-marine letters, v. 1, p. 29-32.

Cartwright, J.A., 2007, The impact of 3D seismic data on the understanding of compaction, fluid flow and diagenesis in sedimentary basins: Journal of the Geological Society, v. 164(5), p. 881-893.

Cartwright, J.A., Dewhurst, D.N., 1998, Layer-bound compaction faults in fine-grained sediments: Geological Society of America Bulletin, v. 110, p. 1242-1257.

Cartwright, J.A., Huuse, M., 2005, 3D Seismic: The geological 'Hubble.': Basin Research, v. 17, p. 1-20.

Cartwright, J.A., Huuse, M., Aplin, A., 2007, Seal bypass systems: American Association of Petroleum Geologists Bulletin, v. 91(8), p. 1141-1166.

Cartwright, J.A., Lonergan, L., 1996, Volumetric contraction during the compaction of mudrocks: a mechanism for the development of regional-scale polygonal fault systems: Basin Research, v. 8, p. 183-193.

Chen D., Su, Z., Cathles, L.M., 2006, Types of gas hydrates in marine environments and their thermodynamic characteristics: Diqiu Kexue Jikan = TAO, Terrestrial, Atmospheric and Oceanic Sciences, v. 17(4), p. 723-737.

Clayton, C.J., Hay, S.J., Baylis, S.A., Dipper, B., 1997, Alteration of natural gas during leakage from a North Sea salt diapir field: Marine Geology, v. 137(1-2), p. 69-80.

Clennell, M.B., Hovland, M., Booth, J.S., Henry, P., Winters, W.J.,1999, Formation of natural gas hydrates in marine sediments 1. Conseptual model of gas hydrate growth conditioned by host sediment properties: Journal of Geophysical Research, v. 104, p. 22,985-23,003.

Collett, T.S., Riedel, M., Cochran, J.R., Boswell, R., Kumar, P., Sathe, A.V., the NGHP Exp. 01 Scientific Party, July 6-10, 2008, Indian continental margin gas hydrate prospects: results of the Indian National Gas Hydrate program (NGHP) expedition 01. Proceedings of the 6th International Conference on Gas Hydrates (ICGH 2008), Vancouver, BC, Canada.

Cooper, A.K., Hart, P.E., 2002, High-resolution seismic-reflection investigation of the northern Gulf of Mexico gas-hydrate-stability zone: Marine and Petroleum Geology, v. 19, p. 1275-1293.

Cox, S.F., Knackstedt, M.A., Braun, J., 2001, Principles of structural control on permeability and fluid flow in hydrothermal systems: Reviews in Economic Geology, v. 14, p. 1-24.

D

Dai, J., Xu, H., Snyder, F., Dutta, N., 2004, Detection and estimation of gas hydrates using rock physics and seismic inversion: Examples from the northern deepwater Gulf of Mexico: The leading edge, p. 60-66.

Davie, M.K., Buffett, B.A., 2003, Sources of methane for marine gas hydrate: inferences from a comparison of observations and numerical models: Earth and Planetary Science Letters, v. 206(1-2), p. 51-63.

Davies, R.J., 2003, Kilometre-scale fluidization structures formed during early burial of a deep-water slope channel on the Niger Delta: Geological Society of America, v. 31, no. 11, p. 949-952.

Davies, R.J., Cartwright, J.A., 2002, A fossilized Opal A to Opal C/T transformation on the northeast Atlantic margin: support for a significantly elevated Palaeogeothermal gradient during the Neogene?: Basin Research, v. 14, p. 467-486.

Davies, R.J., Clarke, A.L., 2010, Methane recycling between hydrate and critically pressured stratigraphic traps, offshore Mauritania: Geology, v. 38, p. 963-966.

Davies, R.J., Goulty, N.R., Meadows, D., 2008, Fluid flow due to the advance of basin-scale silica reaction zones: Geological Society of America Bulletin, v. 120, no. 1-2, p. 195-206.

Davies, R.J., Thatcher, K.E., Armstrong, H., Yang, J., Hunter, S., 2012a, Tracking the relict bases of marine methane hydrates using their intersections with stratigraphic reflections: Geology, v. 40, p. 1011-1014.

Davies, R.J., Thatcher, K.E., Mathias, S.A., Yang, J., 2012b, Deepwater canyons: An escape route for methane sealed by methane hydrate: Earth and Planetary Science Letters, v. 323-324, no. 0, p. 72-78.

Deshenenkov, I.S., Kozhevnikov, D.A., Kovalenko, K.V., 2011, Well to Seismic Ties Modeling with the Adaptive Log Analysis, Adapted from extended abstract prepared in conjunction with poster presentation at AAPG International Conference and Exhibition, Milan, Italy.

Dickens, G.R., 1999, The blast in the past: Nature, v. 401, p. 752-755.

Dickens, G.R., 2001a. Modeling the global carbon cycle with a gas hydrate capacitor: significance for the Latest Paleocene thermal maximum. In: Paull, C.K., Dillon, W.P. (Eds.), Natural Gas Hydrates: Occurrence, Distribution, and Detection, Geophysical Monograph Series. v. 124, p. 19-38, American Geophysical Union, Washington, D.C.

Dickens, G.R., 2001b. On the fate of past gas: what happens to methane released from a bacterially mediated gas hydrate capacitor? Geochemistry, Geophysics, Geosystems, v. 2(1), p. 1037.

Dickens, G.R., 2001c, The potential volume of oceanic methane hydrates with variable external conditions: Organic Geochemistry, v. 32(10), p. 1179-1193.

Dickens, G.R., O'Neil, J.R., Rea, D.K., Owen, R.M., 1995, Dissociation of oceanic methane hydrate as a cause of the carbon isotope excursion at the end of the Paleocene: Paleoceanography, v.10, p. 965-971.

Dillon, W.P., Paull, C.K., 1983, Marine gas hydrates—II: Geophysical evidence, in Cox, J.L., edition, Natural gas hydrates: Properties, occurrence and recovery: Boston, Butterworth, p. 73-90.

E

Edwards, R.A.,1998, 22 Integration of seismic reflection, physical properties, and downhole logging data, In Mascle, J., Lohmann, G.P., and Moullade, M. (Edition), Proceeding of the Ocean Drilling Program, Scientific Results, v. 159, p. 225-240.

Emery, D., Myers, K., Bertram, G.T., 1996, Sequence stratigraphy: Blackwell Science, Oxford, Cambridge, Mass.

F

Ferentinos, G., Brooks, M., Collins, M., 1981, Gravity-induced deformation on the north flank and floor of the sporadhes basin of the North Aegean sea trough: Marine Geology, v. 44, p. 289-302.

Field, M.E., Kvenvolden, K.A., 1985, Gas hydrates on the northern California continental margin: Geology, v. 13, p. 517-520.

Foland, S.S., Maher, N., Yun, J.W., 1999, Pockmarks along the Californian Continental Margin: implications for fluid flow, Abstract: American Association of Petroleum Geologists Bulletin, v. 83, p. 681-706.

G

Garziglia, S., Migeon, S., Ducassou, E., Loncke, L., Mascle, J., 2008, Mass-transport deposits on the Rosetta province (NW Nile deep-sea turbidite system, Egyptian margin): Characteristics, distribution, and potential causal processes: Marine Geology, v. 250(3-4), p. 180-198.

Gay, A., Berndt, C., 2007, Cessation/reactivation of polygonal faulting and effects on fluid flow in the Vøring Basin, Norwegian Margin: Journal of the Geological Society, v. 164, no. 1, p. 129-141.

Gay, A., Lopez, M., Berndt, C., Séranne, M., 2007, Geological controls on focused fluid flow associated with seafloor seeps in the Lower Congo Basin: Marine Geology, v. 244, p. 68-92.

Gay, A., Lopez, M., Cochonat, P., Séranne, M., Levaché, D., Sermondadaz, G., 2006, Isolated seafloor pockmarks linked to BSRs, fluid chimneys, polygonal faults and stacked Oligocene-Miocene turbiditic palaeochannels in the Lower Congo Basin: Marine Geology, v. 226, p. 25-40.

Gay, A., Lopez, M., Cochonat, P., Sultan,N., Cauquil, E., Brigaud, F., 2003, Sinuous pockmark belt as indicator of a shallow buried turbiditic channel on the lower slope of the Congo Basin, West African Margin: Geological Society of London, Special Publication, v. 216, p.173-189.

Ginsburg, G.D., 1998, Gas hydrate accumulation in deep-water marine sediments: Geological Society, London, Special Publications, v. 137(1), p. 51-62.

Gordon, D.S., Flemings, P.B., 1998, Generation of overpressure and compaction-driven fluid flow in a Plio-Pleistocene growth-faulted basin, Eugene Island 330, offshore Louisiana: Basin Research, v. 10(2), p. 177-196.

Guerin, G., Goldberg, D., Meltser, A., 1999, Characterization of in situ elastic properties of gas hydrate-bearing sediments on the Blake Ridge: Journal of Geophysical Research: Solid Earth, v. 104(B8), p. 17781-17795.

H

Haacke, R.R., Westbrook, G.K., Hyndman, R.D., 2007, Gas hydrate, fluid flow and free gas: Formation of the bottom-simulating reflector: Earth and Planetary Science Letters, v. 261, no. 3-4, p. 407-420.

Hale, D., 2009, Structure-oriented smoothing and semblance: Center for Wave Phenomena Publ. CWP-635.

Hampton, M.A., Lee, H.J., Locat, J., 1996, Submarine landslides: Reviews of Geophysics, v. 34(1), p. 33-59.

Haq, B.U. 1998, Natural gas hydrates: searching for the long-term climatic and slope-stability records: In. HENRIET, J.-P. & MmNERT, J. (eds) Gas Hydrates: Relevance to World Margin Stability and Climate Change. Geological Society, London, Special Publications, v. 137, p. 303-318.

Heiniö, P., Davies, R., 2009, Trails of depressions and sediment waves along submarine channels on the continental margin of Espirito Santo Basin, Brazil: Geological Society of America Bulletin, v. 121, no. 5-6, p. 698-711.

Henrich, R., Cherubini, Y., Meggers, H., 2010, Climate and sea level induced turbidite activity in a canyon system offshore the hyperarid Western Sahara (Mauritania): The Timiris Canyon: Marine Geology, v. 275, p. 178-198.

Henrich, R., Hanebuth, T.J.J., Krastel, S., Neubert, N., Wynn, R.B., 2008, Architecture and sediment dynamics of the Mauritania Slide Complex: Marine and Petroleum Geology, v. 25, p. 17-33.

Henry, P., Clennell, M.B., Thomas, M., 1999, Formation of natural gas hydrates in marine sediments: 2. Thermodynamic calculations of stability conditions in porous sediment: Journal of Geophysical Research 104, v. 23, p. 005-022.

Hickey, B.M., 1997, Response of a narrow submarine canyon to strong wind forcing: Journal of Physical Oceanography, v. 27, p. 697-726.

Hilgers, C., Kirschner, D.L., Breton, J.P., Urai, J.L., 2006, Fracture sealing and fluid overpressures in limestones of the Jabal Akhdar dome, Oman mountains: Geofluids, v. 6(2), p. 168-184.

Ho, S., Cartwright, J., Imbert, P., 2012, Vertical evolution of fluid venting structures in relation to gas flux, in the Neogene-Quaternary of the Lower Congo Basin, Offshore Angola: Marine Geology, v. 332-334(0), p. 40-55.

Holbrook, W.S., Hoskins, H., Wood, W.T., Stephen, R.A., Lizarralde, D., Leg 164 Science Party, 1996, Methane hydrate and free gas on the Blake Ridge from vertical seismic profiling: Science, v. 273, p. 1840-1843.

Hornbach, M.J., Saffer, D.M., Holbrook, W.S., 2004, Critically pressured free-gas reservoirs below gas-hydrate provinces: Nature, v. 427, p. 142-144.

Horozal, S., Lee, G.H., Yi, B.Y., Yoo, D.G., Park, K.P., Lee, H.Y., Kim, W., Kim, H.J., Lee, K., 2009, Seismic indicators of gas hydrate and associated gas in the Ulleung Basin, East Sea (Japan Sea) and implications of heat flows derived from depths of the bottom-simulating reflector: Marine Geology, v. 258(1-4), p. 126-138.

Hovland, M., Gallagher, J. W., Clennell, M. B., Lekvam, K., 1997, Gas hydrate and free gas volumes in marine sediments: Example from the Niger Delta front: Marine and Petroleum Geology, v. 14, no. 3, p. 245-255.

Hovland, M., Gardner, J.V., Judd, A.G., 2002, The significance of pockmarks to understanding fluid flow processes and geohazards: Geofluids, v. 2, p. 127-136.

Hovland, M., Judd, A.G., 1988, Seabed pockmarks and seepages: impact on geology, biology and the marine environment. Graham and Trotman, London.

Hovland, M., Talbot, M.R., Qvale, H., Olaussen, S., Aasberg, L., 1987, Methane-related carbonate cements in pockmarks of the North Sea: Journal of Sedimentary Petrology, v. 57, p. 881-892.

Hübscher, C., Kukowski, N., 2003, Complex BSR pattern in the Yaquina Bsin off Peru: Geo-Mar Letter, v.23, p. 91-101.

Hustoft, S., Mienert, J., Bünz, S., Nouzé, H., 2007, High-resolution 3D-seismic data indicate focussed fluid migration pathways above polygonal fault systems of the mid-Norwegian margin: Marine Geology, v. 245, p. 89-106.

Hyndman, R.D., Davis, E.E., 1992, A mechanism for the formation of methane hydrate and seafloor bottom-simulating-reflectors by vertical fluid expulsion: Journal of Geophysical Research, v. 97 (B5), p. 7025-7041.

I

Ingram, G.M., Chisholm, T.J., Grant, C.J., Hedlund, C.A., Stuart-Smith, P., Teasdale, J., 2004, Deepwater North West Borneo: hydrocarbon accumulation in an active fold and thrust belt: Marine and Petroleum Geology, v.21(7), p. 879-887.

Ireland, M.T., 2011, 3-D seismic investigation of the diagenesis and deformation of Cenozoic siliceous sediment on the Eastern Atlantic Margin: Doctoral thesis, Durham University.

Ireland, M.T., Goulty, N.R., Davies, R.J., 2011, Influence of stratigraphic setting and simple shear on layer-bound compaction faults offshore Mauritania: Journal of Structural Geology, v. 33, no. 4, p. 487-499.

Isaacs, C.M., 1982, Influence of rock composition on kinetics of silica phase-changes in the Monterey Formation, Santa-Barbara area, California: Geology, v. 10, p. 304-308.

J

Judd, A.G., Hovland, M., 2007, Seabed Fluid Flow – The Impact on Geology, Biology and the Marine Environment. Cambridge University Press, Cambridge.

K

Katz, D., Cornell, D., Kobayashi, R., 1959, Handbook of Natural gas Engineering, MacGraw-Hill, New York.

Klauda, J.B., Sandler, S.I., 2005, Global Distribution of Methane Hydrate in Ocean Sediment: Energy Fuel, v.19, p. 459-470.

Kopf, A.J., 2002, Significance of mud volcanism. Rev. Geophys., v. 40, p. 1-52.

Krastel, S., Wynn, R.B., Hanebuth, T.J.J., 2006, Mapping of seabed morphology and shallow sediment structure of the Mauritania continental margin, Northwest Africa: some implications for geohazard potential: Norwegian Journal of Geology, v. 86, p. 163-176.

Krooss, B.M., Leythaeuser, D., 1996, Molecular diffusion of light hydrocarbons in sedimentary rocks and its role in migration and dissipation of natural gas: in D. Schumacher and Abrams, M.A., eds., Hydrocarbon migration and its nearsurface expression: AAPG Memoir, v. 66, p. 173-183.

Krooss, B.M., Leythaeuser, D., Schaefer, R.G., 1988, Light hydrocarbon diffusion in a caprock: Chemical Geology, v. 71(1-3), p. 65-76.

Kumar, D., Sen, M.K., Bangs, N.L., 2006, Seismic characteristics of gas hydrates at Hydrate Ridge, offshore Oregon: The leading edge, p. 610-614.

Kvenvolden, K.A., 1998, A primer on the geological occurrence of gas hydrate, in Henriet, J.P., and Mienert, J. (eds) Gas hydrate: Relevance to World Margin Stability Change: Geological Society Special Publication, v. 137, p. 9-30.

Kvenvolden, K.A., 1999, Potential effects of gas hydrate on human welfare: Proceedings of National Academy of Science, v. 96, p. 3420-3426.

Kvenvolden, K.A., 2002, Methane hydrate in the global organic carbon cycle: Terra Nova, v. 14(5), 302-306.

Kwon, T.H., Cho, G.C., Santamarina, J.C., 2008, Gas hydrate dissociation in sediments: Pressure-temperature evolution: Geochemistry, Geophysics, Geosystems, v. 9(3), Q03019.

L

Laberg, J. S., Andreassen, K., 1996, Gas hydrate and free gas indications within the Cenozoic succession of the Bjørnøya Basin, western Barents Sea: Marine and Petroleum Geology, v. 13, no. 8, p. 921-940.

Laird, A.P., Morley, C.K.. 2011, Development of gas hydrates in a deep-water anticline based on attribute analysis from three-dimensional seismic data: Geosphere, v.7(1), p. 240-259.

Landmark, 2005, SeisWorks/3D Horizon Interpretation, in: Landmark Users Manuals. Landmark Graphics Corporation.

LeBlanc, C., Louden, K., Mosher, D., 2007, Gas hydrates off Eastern Canada: Velocity models from wide-angle seismic profiles on the Scotian Slope: Marine and Petroleum Geology, v. 24(5), p. 321-335.

Leduc, A. M., R.J. Davies, A.L. Densmore, J. Imber, 2011, The lateral strike-slip domain in gravitational detachment delta systems: A case study of the northwestern margin of the Niger Delta, American Association of Petroleum Geologists Bulletin, p. 1-20.

Lee, M.W., Collett, T.S., 2011, In-situ gas hydrate hydrate saturation estimated from various well logs at the Mount Elbert Gas Hydrate Stratigraphic Test Well, Alaska North Slope: Marine and Petroleum Geology, v. 28(2), p. 439-449.

Lee, H.-Y., Park, K.-P., Koo, N.-H., Yoo, D.-G., Kang, D.-H., Kim, Y.-G. Hwang, K.-D., Kim, J.-C., 2004, High-resolution shallow marine seismic surveys off Busan and Pohang, Korea, using a small-scale multichannel system: Journal of Applied Geophysics, v. 56(1), p. 1-15.

Lewis, K.B., 1971, Slumping on a continental slope inclined at 1–4°: Sedimentology, v. 16, p. 97-110.

Leythaeuser, D., Schaefer, R.G., Yukler, A., 1982, Role of diffusion in primary migration of hydrocarbons: American Association of Petroleum Geologists Bulletin, v. 66(4), p. 408-429.

Ligtenberg, J.H., 2005, Detection of fluid migration pathways in seismic data: implications for fault seal analysis: Basin Research, v. 17, p. 141-153.

Linari, V., 2004, A practical approach to well-seismic data calibration: The leading edge, v. 23(8), p. 774-775.

Liu, X., Flemings, P.B., 2006, Passing gas through the hydrate stability zone at southern Hydrate Ridge, offshore Oregon: Earth and Planetary Science Letters, v. 241, no. 1-2, p. 211-226.

Løseth, H., Wensaas, L., Arntsen, B., Hanken, N.-M., Basire, C., Graue, K., 2011, 1000 m long gas blow-out pipes: Marine and Petroleum Geology, v. 28(5), p. 1047-1060.

Lüdmann, T., Wong, H.K., Konerding, P., Zillmer, M., Petersen, J., Flüh, E., 2004, Heat flow and quantity of methane deduced from a gas hydrate field I the vicinity of the Dnieper Canyon, northwestern Black Sea: Geo-Mar letter, v. 24, p. 182-193.

M

MacDonald, I.R., Guinasso, N.L., Jr., Sassen, R., Brooks, J.M., Lee, L., Scott, K.T., 1994, Gas hydrate that breaches the sea floor on the continental slope of the Gulf of Mexico: Geology, v. 22, p. 699-702.

Makogon, Y.F., 1997, Hydrates of Natural Gas. Penn Well Books, Tulsa, Oklahoma.

Malinverno, A., 2010, Marine gas hydrates in thin sand layers that soak up microbial methane: Earth and Planetary Science Letters, v. 292, no. 3-4, p. 399-408.

Mark, A.S., Steven, H.W., Craig, L.F., Oxford, 1995, Seawater (Second Edition), Chapter 2 - Temperature in the oceans: Oxford, Butterworth-Heinemann, p. 14-28.

Matsumoto, R., 1989, Isotopically heavy oxygen-containing siderite derived from the decomposition of methane hydrate: Geology, v. 17, p. 707-710.

Max, M.D., 2003, Natural Gas Hydrate in Oceanic and Permafrost Environments, Kluwer Academic Publishers, Netherlands.

McIver, R.D., 1977, Hydrates of natural gas–Important agent in geological processes: Geological Society of America, Abstracts, v. 9, p. 1989-1990.

McIver, R.D., 1981, Gas hydrates. In: Meyer, R.G., Olson, J.C. (Eds.), Long-Term Energy Resources Pitman, Boston, MA, p. 713-726.

Milkov, A.V., 2000, Worldwide distribution of submarine mud volcanoes and associated gas hydrates: Marine Geology, v. 167(1-2), p. 29-42.

Milkov, A.V., 2004, Global estimates of hydrate-bound gas in marine sediments: how much is really out there?: Earth-Science Reviews, v. 66, p. 183-197.

Milkov, A.V., Claypool, G.E., Lee, Y.-J., Dickens, G.R., Xu, W., Borowski, W.S., the ODP Leg 204 Scientific Party, 2003, In situ methane concentrations at Hydrate Ridge offshore Oregon: new constraints on the global gas hydrate inventory from an active margin: Geology, v. 31, p. 833-836.

Miller, P., Dasgupta, S., Shelander, D., 2012, Seismic imaging of migration pathways by advanced attribute analysis, Alaminos Canyon 21, Gulf of Mexico: Marine and Petroleum Geology, Marine and Petroleum Geology, v. 34(1), p. 111-118.

Mitchum, R.M., Jr., Vail, P.R., 1977, Seismic stratigraphy and global changes of sea level, part 7: Seismic Stratigraphic Interpretation Procedure, in: Payton, C. (Edition), Seismic Stratigraphy-Applications to Hydrocarbon Exploration, American Association of Petroleum. Geologists Memoir 26, p. 135-143.

Mosher, D.C., 2011, A margin-wide BSR gas hydrate assessment: Canada’s Atlantic margin: Marine and Petroleum Geology, v. 28(8), p. 1540-1553.

N

Navalpakam, R.S., Pecher, I.A., Stern, T., 2012, Weak and segmented bottom simulating reflections on the Hikurangi Margin, New Zealand — Implications for gas hydrate reservoir rocks: Journal of Petroleum Science and Engineering, v. 88-89(0), p. 29-40.

O

O’Brien, G.W. Woods, E.P., 1995, Hydrocarbon-related diagenetic zones (HRDZs) in the Vulcan Subbasin,Timor Sea: recognition and exploration implications. APEA Journal, v. 35, p.220-252.

Orange, D.L., Breen, N.A., 1992, The effects of fluid escape on accretionary wedges, 2, Seepage force, slope failure, headless submarine canyons, and vents: Journal of Geophysical Research, v. 97, p. 9277-9295.

Osborne, M.J., Swarbrick, R.E., 1997, Mechanisms for generating overpressure in sedimentary basins: A reevaluation: American Association of Petroleum Geologists Bulletin, v. 81(6), p. 1023-1041.

P

Paull, C.K., Dillon, W.P., Ussler III, W., 2000, Potential role of gas hydrate decomposition in generating submarine slope failures. In: Max, M.D. (Edition), Natural Gas Hydrate in Oceanic and permafrost Environments. Kluwer Academic Publishers, Dordrecht, p. 149-156.

Paull, C.K., Matsumoto, R., Wallace, P.J., et al., 1996, Proc. ODP, Init. Repts., 164: College Station, TX (Ocean Drilling Program).

Paull, C.K., Ussler III, W., Borowski, W.S., 1994, Sources of Biogenic Methane to Form Marine Gas Hydrates In Situ Production or Upward Migration?: Annals of the New York Academy of Sciences, v. 715(1), p. 392-409.

Paull, C.K., Ussler, W., III, Dillon, W.P., 1991, Is the extent of glaciation limited by marine gas-hydrates?: Geophysical Research Letters, v. 18, p. 432-434.

Pearson, C.F., Halleck, P.L., McGuire, P.L., Hermes, R., Mathews, M., 1983, Natural gas hydrates:A review of in situ properties: The Journal of Physical Chemistry, v. 87, p. 4180-4185.

Pecher, I.A., Henrys, S.A., Wood, W.T., Kukowski, N., Crutchley, G.J., Fohrmann, M., Kilner, J., Senger, K., Gorman, A.R., Coffin, R.B., Greinert, J., Faure, K., 2010, Focussed fluid flow on the Hikurangi Margin, New Zealand — Evidence from possible local upwarping of the base of gas hydrate stability: Marine Geology, v. 272(1-4), p. 99-113.

Pecher, I.A., Kukowski, N., Huebscher, C., Greinert, J., Bialas, J., 2001, The link between bottom-simulating reflections and methane flux into the gas hydrate stability zone - new evidence from Lima Basin, Peru Margin." Earth and Planetary Science Letters 185(3-4): 343-354.

Pecher, I.A., Minshull, T.A., Singh, S.C., Huene, R.V., 1996, Velocity structure of a bottom simulating reflector offshore Peru: Results from full waveform inversion: Earth and Planetary Science Letters, v. 139, no. 3-4, p. 459-469.

Pilcher, R., Argent, J., 2007, Mega-pockmarks and linear pockmark trains on the West African continental marine: Marine Geology, v. 244, p. 15-32.

Plaza-Faverola, A., Bünz, S., Mienert, J., 2011, Repeated fluid expulsion through sub-seabed chimneys offshore Norway in response to glacial cycles: Earth and Planetary Science Letters, v. 305, no. 3-4, p. 297-308.

Posewang, J., Mienert, J., 1999, High-resolution seismic studies of gas hydrates west of Svalbard: Geo-Marine Letters, v. 19(1), p. 150-156.

R

Rajput, S., Müllera, T.M., Clennella, M.B., Raob, P.P, Thakurb, N.K., 2012, Constraints on seismic reflections and mode conversions at bottom simulating reflectors associated with gas hydrates: Journal of Petroleum Science and Engineering, v. 88-89, p. 48-60.

Rempel, A.W., Buffett, B.A., 1997, Formation and accumulation of gas hydrate in porous media: Journal of Geophysical Research: Solid Earth, v.102(B5), p. 10151-10164.

Rice, D.D., Claypool, G.E., 1981, Generation, Accumulation, and Resource Potential of Biogenic Gas: American Association of Petroleum Geologists Bulletin, v. 65, p. 5-25.

Roberts, H.H., Sassen, R., Milkov, A., 2000, Seafloor expression of fluid and gas expulsion from deep petroleum systems, deepwaterGulf ofMexico: in Weimer, P., edition, Petroleumsystems of deepwater basins: Gulf Coast Section SEPM 21st Annual Research Conference, p. 401-422.

Rodrigo, C., González-Fernández, A., Vera, E., 2009, Variability of the bottom-simulating reflector (BSR) and its association with tectonic structures in the Chilean margin between Arauco Gulf (37°S) and Valdivia (40°S): Marine Geophysical Researches, v. 30, p. 1-19.

Riedel, M., Long, P.E., Collett, T.S., 2006, Estimates of in situ gas hydrate concentration from resistivity monitoring of gas hydrate bearing sediments during temperature equilibration: Marine Geology, v. 227(3-4), p. 215-225.

Ruddiman, W., Sarnthein, M., Baldauf, J. et al., 1988, Proceedings of the Ocean Drilling Program. Scientific Results 108: College Station, TX (Ocean Drilling Program).

Rutter, E.H., Green, S., 2011, Quantifying creep behaviour of clay-bearing rocks below the critical stress state for rapid failure: Mam Tor landslide, Derbyshire, England: Journal of the Geological Society, v. 168, no. 2, p. 359-372.

S

Saeland, G.T., Simpson, G.S., 1982, Interpretation of 3-D data in delineating a sub-unconformity trap in Block 34/10, Norwegian North Sea, in Halbouty, M.T., edition, The deliberate search for the subtle traps: AAPG Memoir, v. 32, p. 217-236.

Sassen, R., 1988, Geochemical and carbon isotopic studies of crude oil destruction, bitumen precipitation, and sulfate reduction in the deep Smackover Formation: Organic Geochemistry, v. 12(4), p. 351-361.

Sassen, R., Joye, S., Sweet, S.T., DeFreitas, D.A., Milkov, A.V., MacDonald, I.R., 1999, Thermogenic gas hydrates and hydrocarbon gases in complex chemosynthetic communities, Gulf of Mexico continental slope: Org Geochem, v. 30, p. 485-497.

Sassen, R., Sweet, S.T., Milkov, A.V., DeFreitas, D.A., Kennicutt, M.C., 2001, Thermogenic vent gas and gas hydrate in the Gulf of Mexico slope: Is gas hydrate decomposition significant?: Geology, v. 29(2), p. 107-110.

Schmuck, E.A., Paull,C.K., 1993, Evidence for gas accumulation associated with diaprism and gas hydrates at the head of the Cape Fear Slide: Geo-Marine Letters, v. 13, p. 145-152.

Schroeter, J.P., Kobayashi, R., Hildebrand. M.A., 1983, Hydrate decomposition conditions in the system H_2S-methane-propane: Ind. Eng. Chem. Fundam., v. 22, p. 361-364.

Shedd, W., Boswell, R., Frye, M., Godfriaux, P., Kramer, K., 2012, Occurrence and nature of “bottom simulating reflectors” in the northern Gulf of Mexico: Marine and Petroleum Geology, v. 34(1), p. 31-40.

Sheriff, R.E. , Geldart, L.P., 1995, Exploration Seismology: CambridgeUniversity Press,USA.

Shipley, T.H., Houston, M.H., Buffler, R.T., Shaub, F.J., Mcmillen, K.J., Ladd, J.W., Worzel, J.L., 1979, Seismic evidence for widespread possible gas hydrate horizons on continental slopes and rises: Bulletin of the American Association of Petroleum Geologists, v. 63, p. 2204-2213.

Singh, S.C., Minshull, T.A., Spence, G.D., 1993, Velocity structure of a gas hydrate reflector: Science, v. 260, p. 204-207.

Sloan, E.D., 1998, Clathrate Hydrates of Natural Gases: 2nd edition, New York.

Stainforth, J.G., Reinders, J.E.A., 1990, Primary migration of hydrocarbons by diffusion through organic matter networks, and its effect on oil and gas generation: Organic Geochemistry, v. 16(1-3), p. 61-74.

Stuevold, L.M., Faerseth, R.B., Arnesen, L., Cartwright, J., Möller, N., 2003, Polygonal faults in the Ormen lange field, Møre basin, offshore mid Norway, In P. Van rensbergen, R.R. Hillis, A.J. Maltman, C.K. Morley, Subsurface sediment mobilization: Geological society, London, special publications, v. 216.

Sultan, N., Cochonat, P., Canals, M., Cattaneo, A., Dennielou, B., Haflidason, H., Laberg, J.S., Long, D., Mienert, J., Trincardi, F., Urgeles, R., Vorren, T.O., Wilson, C., 2004a, Triggering mechanisms of slope instability processes and sediment failures on continental margins: a geotechnical approach: Marine Geology, v. 213, p. 291-321.

Sultan, N., Cochonat, P., Foucher, J.P., Mienert, J., 2004b, Effect of gas hydrates melting on seafloor slope instability: Marine Geology, v. 213(1–4), p. 379-401.

Sultan, N., Voisset, M., Marsset, B., Marsset, T., Cauquil, E., Colliat, J.-L., 2007, Potential role of compressional structures in generating submarine slope failures in the Niger Delta: Marine Geology, v. 237(3-4), p. 169-190.

Sun, Q., Wu, S., Cartwright, J., Dong, D., 2012, Shallow gas and focused fluid flow systems in the Pearl River Mouth Basin, northern South China Sea: Marine Geology, v. 315-318, p. 1-14.

Sun, Q., Wu, S., Cartwright, J., Lüdmann, T., Yao, G., 2013, Focused fluid flow systems of the Zhongjiannan Basin and Guangle Uplift, South China Sea: Basin Research, v. 25(1), p. 97-111.

Sylta, Ø., 2005, On the dynamics of capillary gas trapping: implications for the charging and leakage of gas reservoirs: Geological Society, London, Petroleum Geology Conference series, v. 6, p. 625-631.

T

Taylor, M.H., Dillon, W.P., Pecher, I.A., 2000, Trapping and migration of methane associated with the gas hydrate stability zone at the Blake Ridge Diapir: new insights from seismic data: Marine Geology, v. 164, p. 79-89.

Tohidi, B., Anderson, R., Clennell, M.B., Burgass, R.W., Biderkab, A.B., 2001, Visual observation of gas-hydrate formation and dissociation in synthetic porous material by means of glass macromodels: Geology, v. 29, p. 867-870.

Trofimuk, A.A., Cherskiy, N.V., Tsarev, V.P., 1973, Accumulation of natural gases in zones of hydrate—formation in the hydrosphere: Doklady Akademii Nauk SSSR, v. 212, p. 931-934 (in Russian).

Tucholke, B.E., Bryan, G.M., Ewing, J.I., 1977, Gas hydrate horizons detected in seismic profiler data from the western North Atlantic: American Association of Petroleum Geologists Bulletin, v. 16, p. 698-707.

V

Vandré, C., Cramer, B., Gerling, P., Winsemann, J., 2007, Natural gas formation in the western Nile delta (Eastern Mediterranean): Thermogenic versus microbial: Organic Geochemistry, v. 38(4), p. 523-539.

Vanneste, M., De Batist, M., Golmshtok, A., Kremlev, A., Versteeg, W., 2001, Multi-frequency seismic study of gas hydrate-bearing sediments in Lake Baikal, Siberia: Marine Geology, v. 172(1-2), p. 1-21.

Vear, A., 2005, Deep-water plays of the Mauritanian continental margin: Petroleum Geology Conference series v. 6, p. 1217-1232.

Vially, R., 1992, Bacterial gas: Proceedings of the conference held in Milan, September 25-26, 1989: Editions technip, Paris.

W

Weinberger, J.L., Brown, K.M., Long, P.E., 2005, Painting a picture of gas hydrate distribution with thermal images: Geophysical Research Letters, v. 32, L04609.

Westbrook, G.K., Thatcher, K.E., Rohling, E.J., Piotrowski, A.M., Palike, H., Osborne, A.H., Nisbet, E.G., Minshull, T.A., Lanoiselle, M., James, R.H., Huhnerbach, V., Green, D., Fisher, R.E., Crocker, A.J., Chabert, A., Bolton, C., Beszczynska-Moller, A., Berndt, C., Aquilina, A., 2009, Escape of methane gas from the seabed along the West Spitsbergen continental margin: Geophysical Research Letters, v. 36, L15608.

Wood, W.T., Stoffa, P.L., Shipley, T.H., 1994, Quantitative detection of methane hydrate through high-resolution seismic velocity analysis: Journal of Geophysical Research: Solid Earth, v. 99(B5), p. 9681-9695.

Woodcock, N.H., 1979, Sizes of submarine landslides and their significance: Journal of Structural Geology, v. 1, p. 137-142.

X

Xu, W., C. Ruppel, 1999, Predicting the occurrence, distribution, and evolution of methane gas hydrate in porous marine sediments: Journal of Geophysical Research: Solid Earth, v. 104(B3), p. 5081-5095.

Y

Yakushev, V.S., Chuvilin, E.M., 2000, Natural gas and gas hydrate accumulations within permafrost in Russia: Cold Regions Science and Technology, v. 31(3), p. 189-197.

Yang, J., Davies, R.J., 2013, Gravity-driven faults: migration pathways for recycling gas after the dissociation of marine gas hydrates: Marine Geology, v. 336, p.1-9.

Yang, J., Davies, R.J., Huuse, Mads, 2013, Gas migration below gas hydrates controlled by mass transport complexes, offshore Mauritania: Marine and Petroleum Geology, v. 48, p. 366-378.

Yilmaz, Ö., Doherty, S.M., 1987, Seismic data processing. Society of Exploration Geophysicists, Tulsa, OK.

Appendix A- Comparison of 2D and 3D seismic data

1) 2D and 3D seismic surveys offshore Mauritania

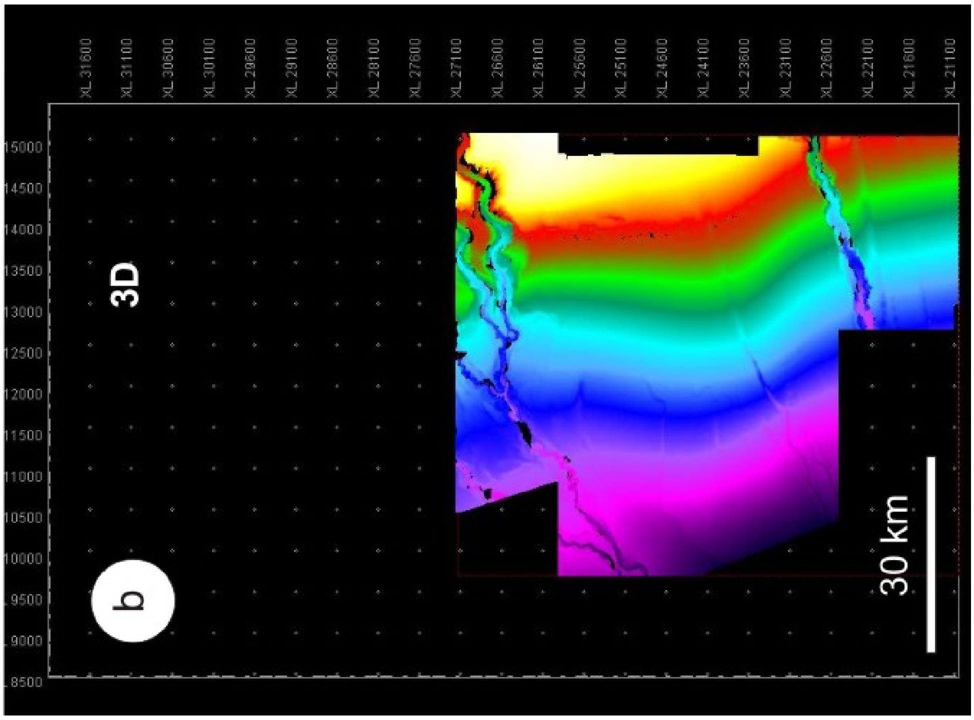

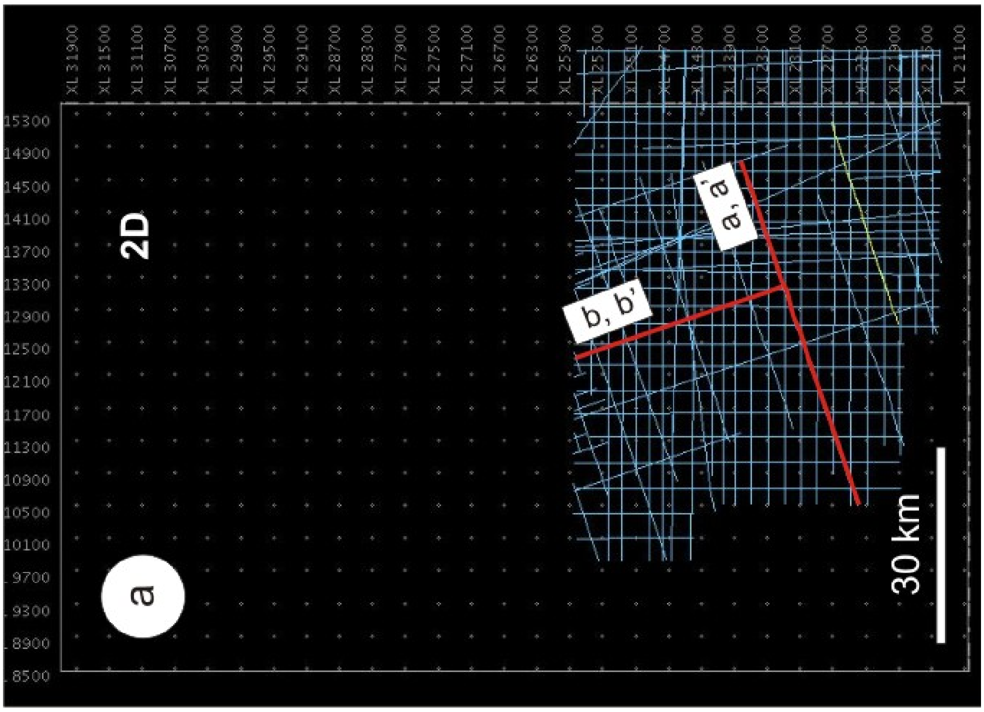

2) 2D and 3D seismic lines

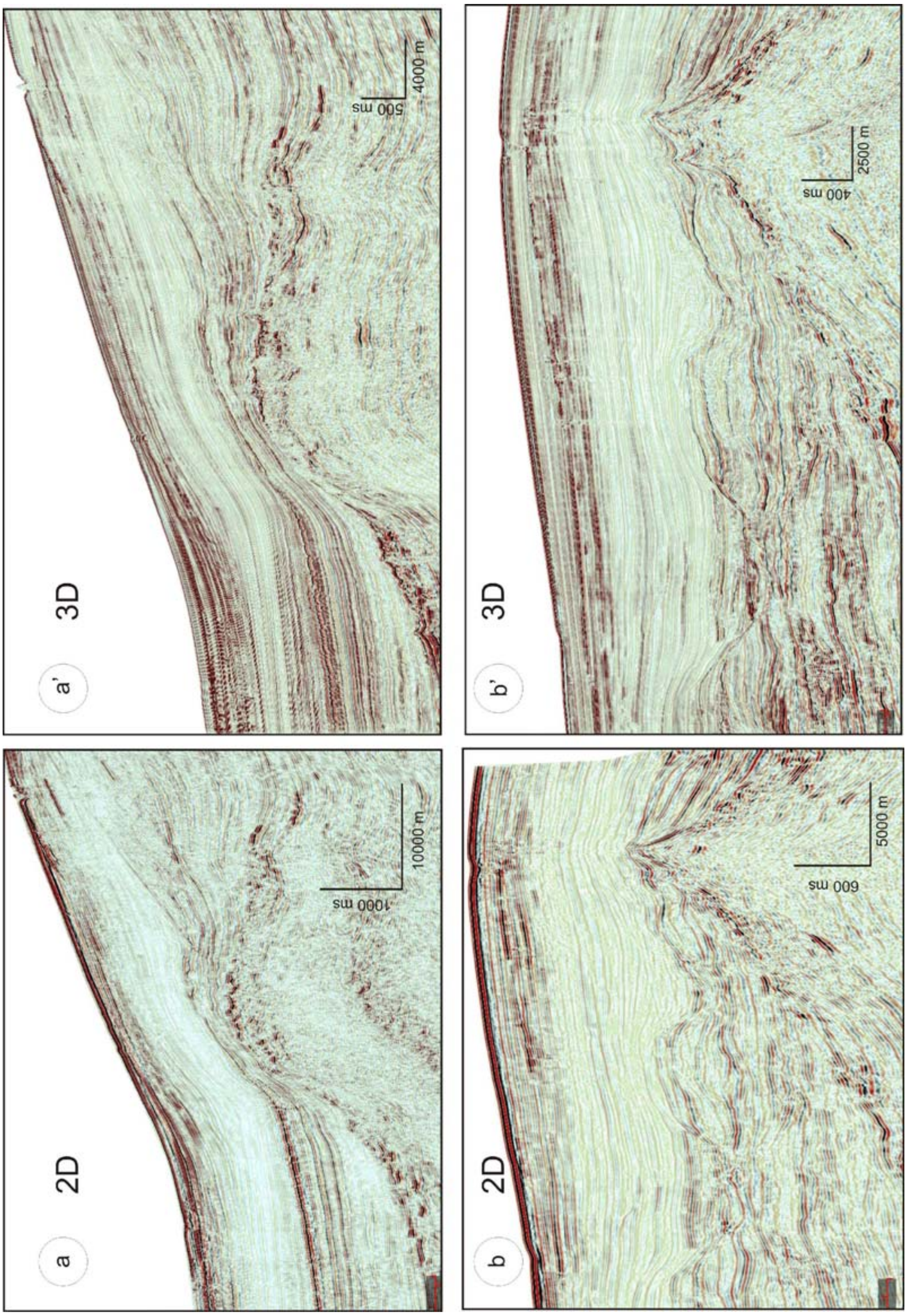

See 2D seismic survey for locations.

Appendix B- Supporting material for chapter 3

1) Interpreted reflections to study the localized HAAs

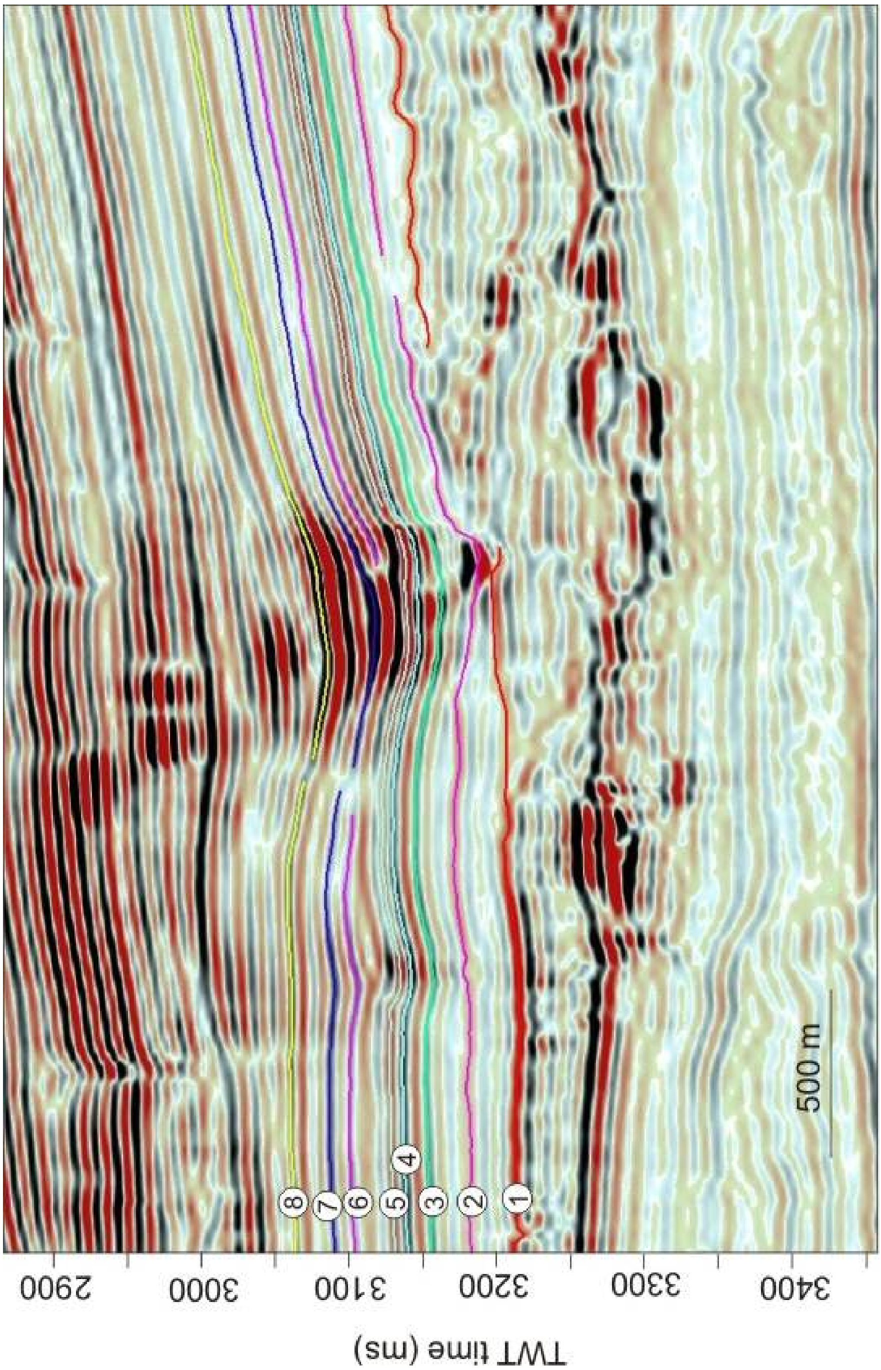

2) Amplitude maps of reflections 2, 3 and 5

See figure 3.1b for map location.

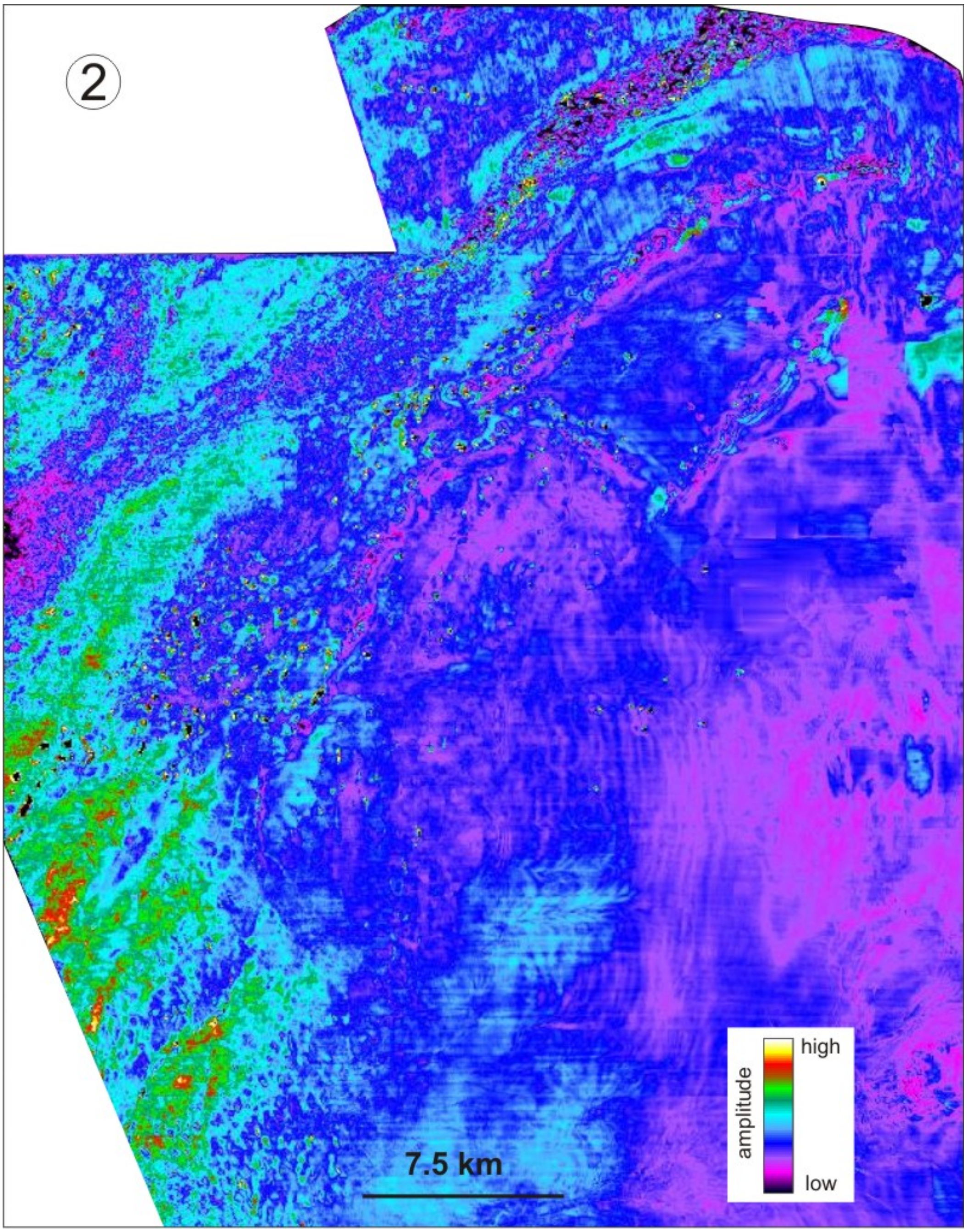

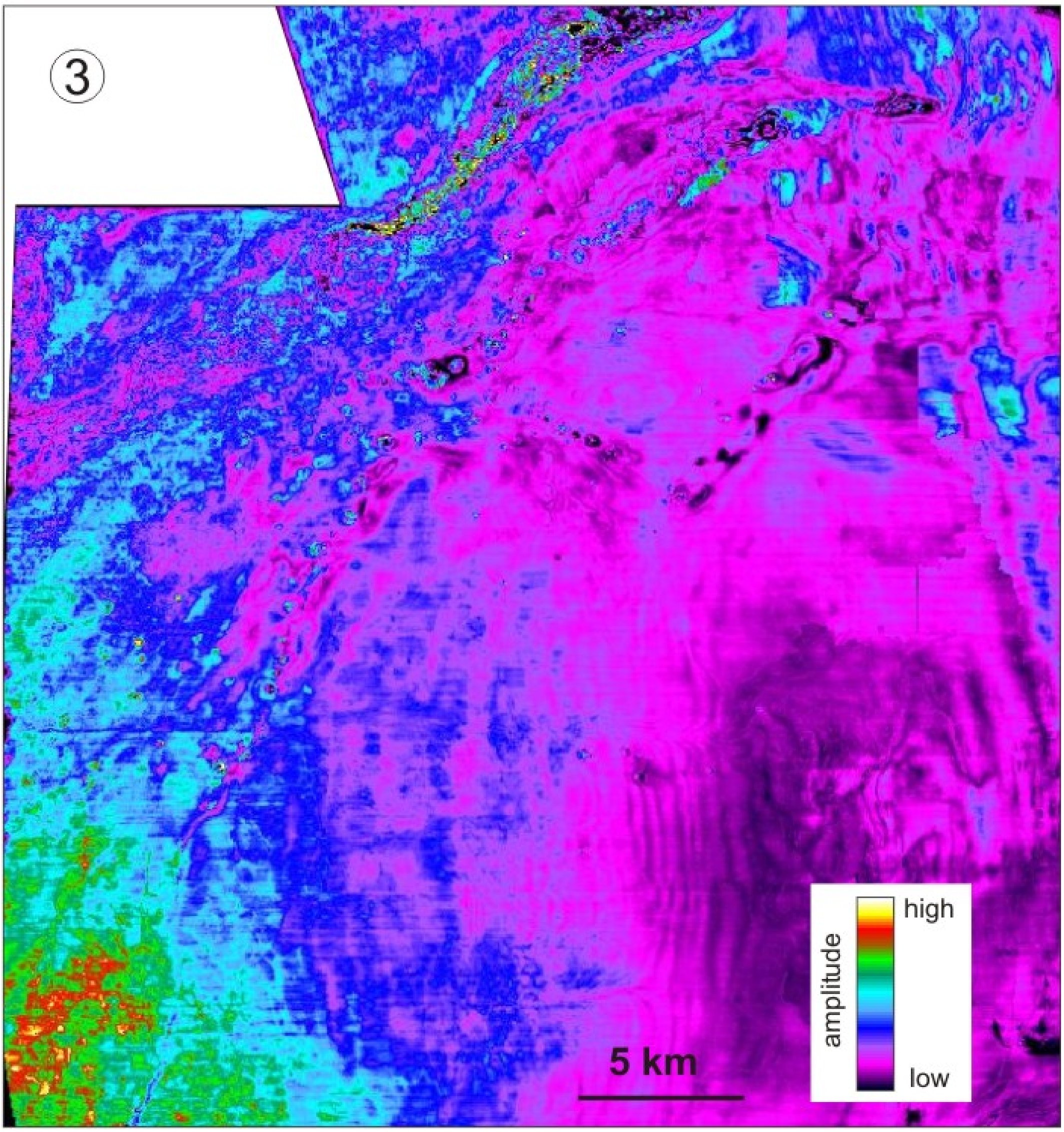
③
5 km
high
amplitude
low

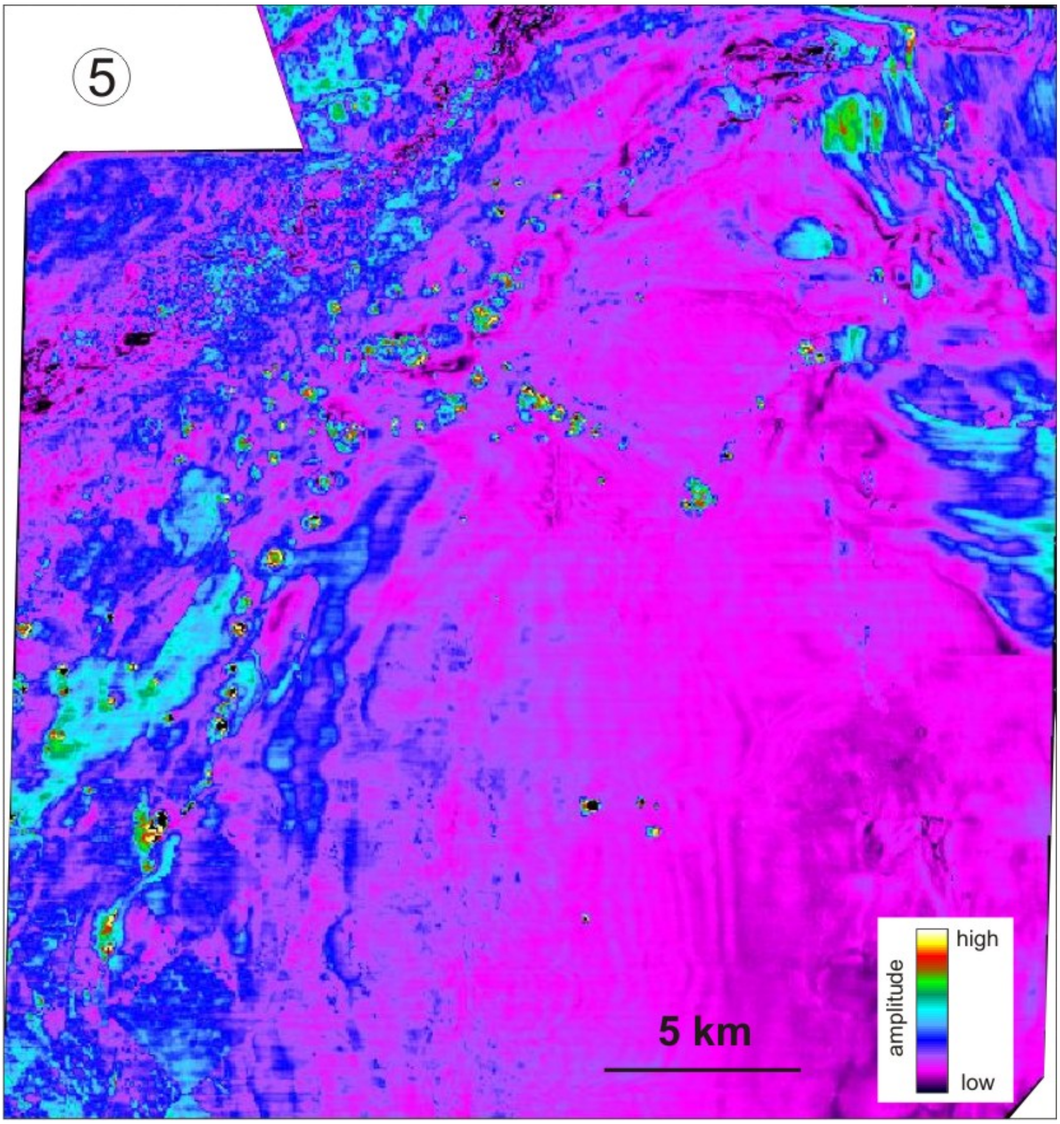
5
5 km
high
amplitude
low

Appendix C- Supporting material for chapter 4

1) Time slice, showing structures at depth of 2772 ms

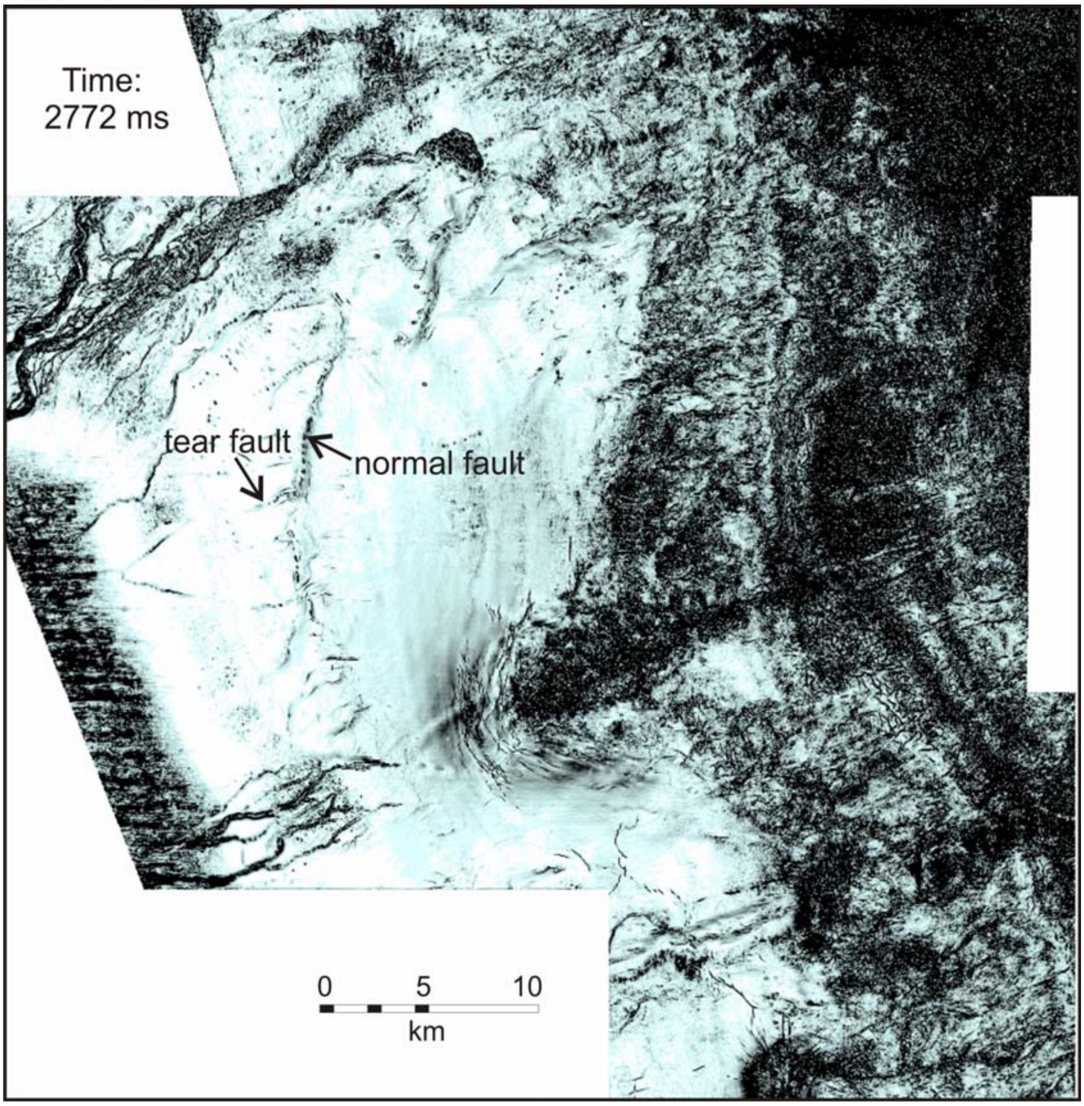

2) 3D visualization of the locations of a normal fault, a stratigraphic gas trap and a FGZ

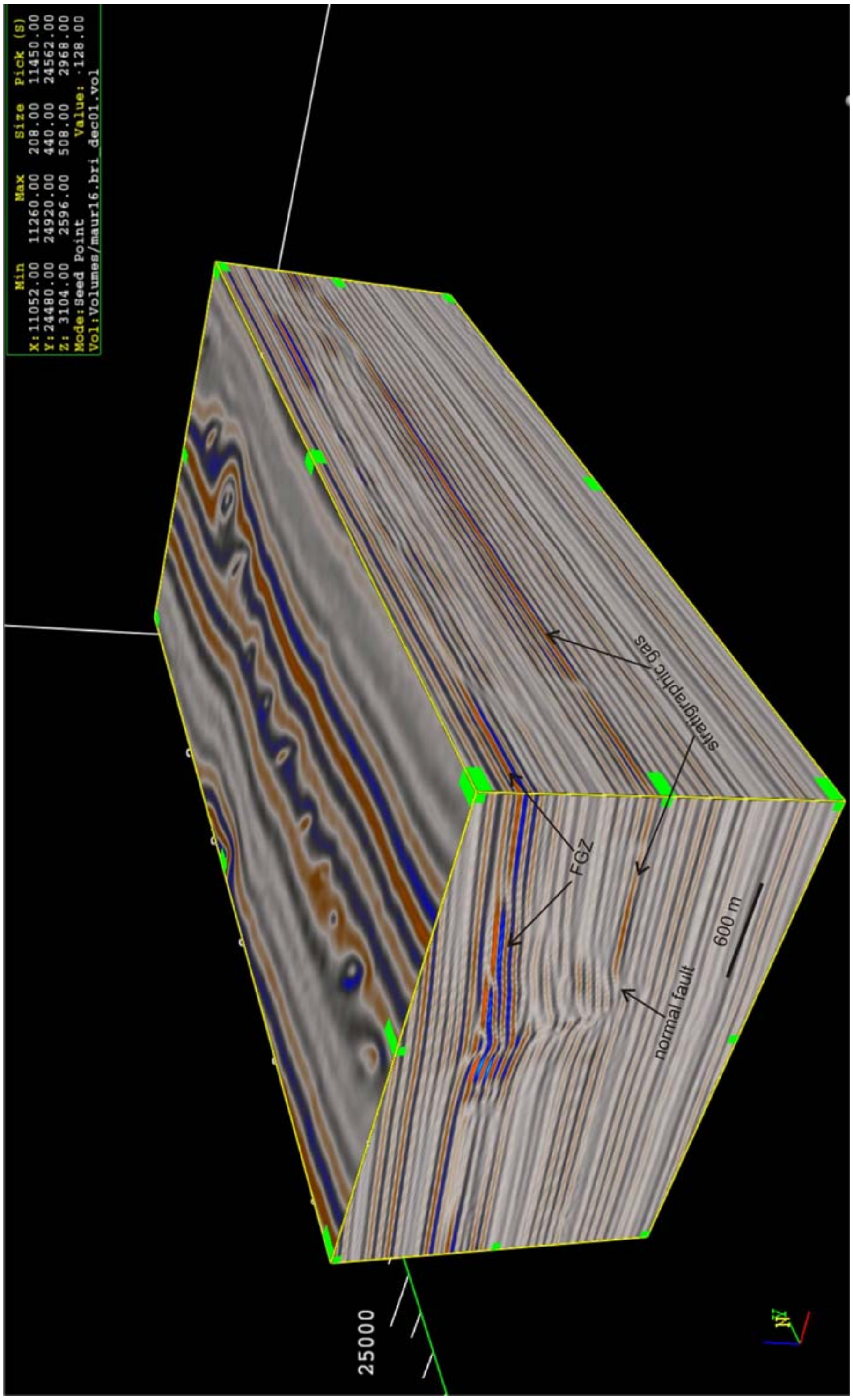

```
        Min        Max       Size   Pick (S)
X: 11052.00   11260.00    208.00   11450.00
Y: 24480.00   24920.00    440.00   24562.00
Z:  3104.00    2596.00    508.00    2968.00
Mode: Seed Point            Value: -128.00
Vol: Volumes/maur16.bri_dec01.vol
```

Appendix D- Supporting material for chapter 5

---

1) Seismic sections showing the BSR, with (b) showing wiggle on top

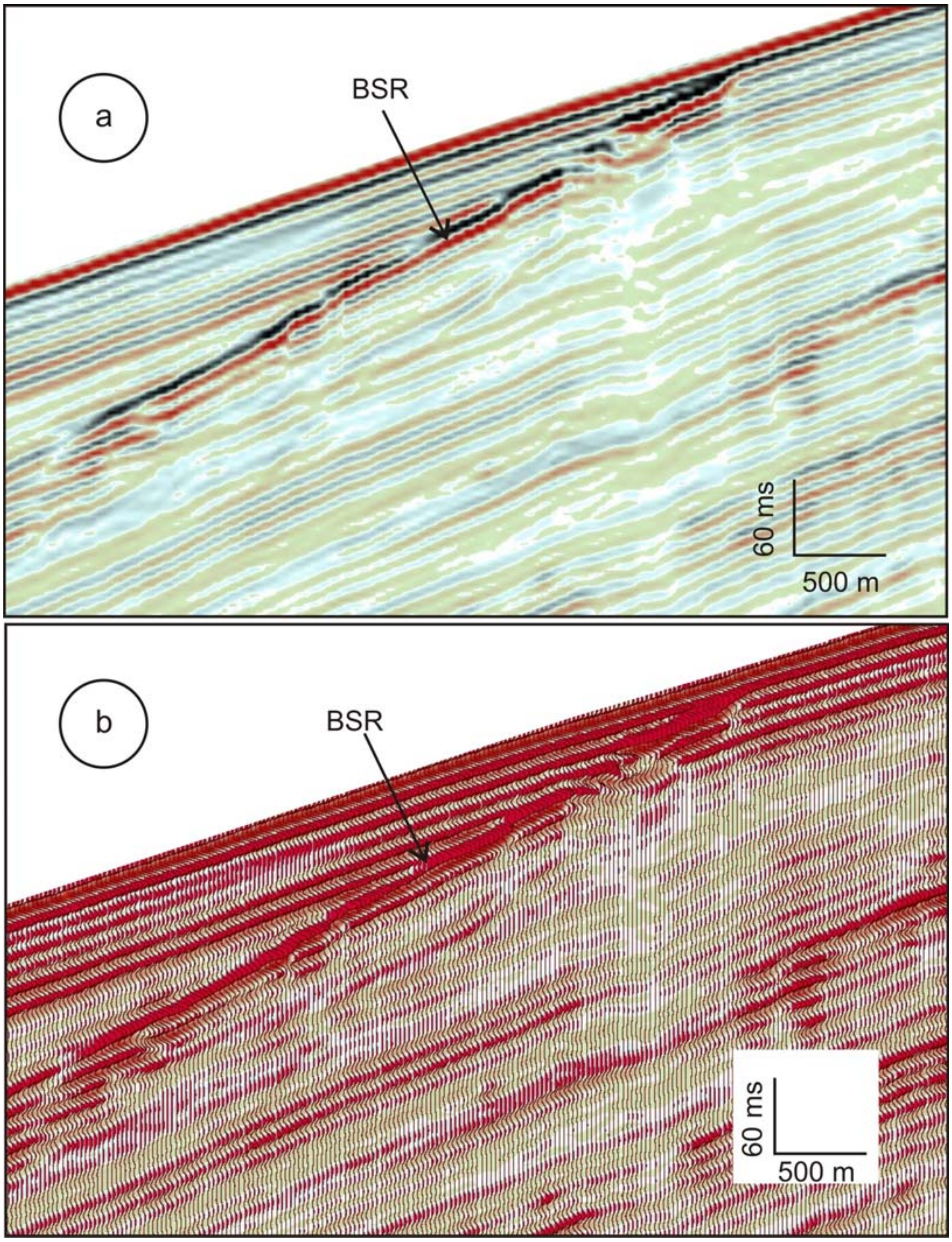

2) Maps with contours on top

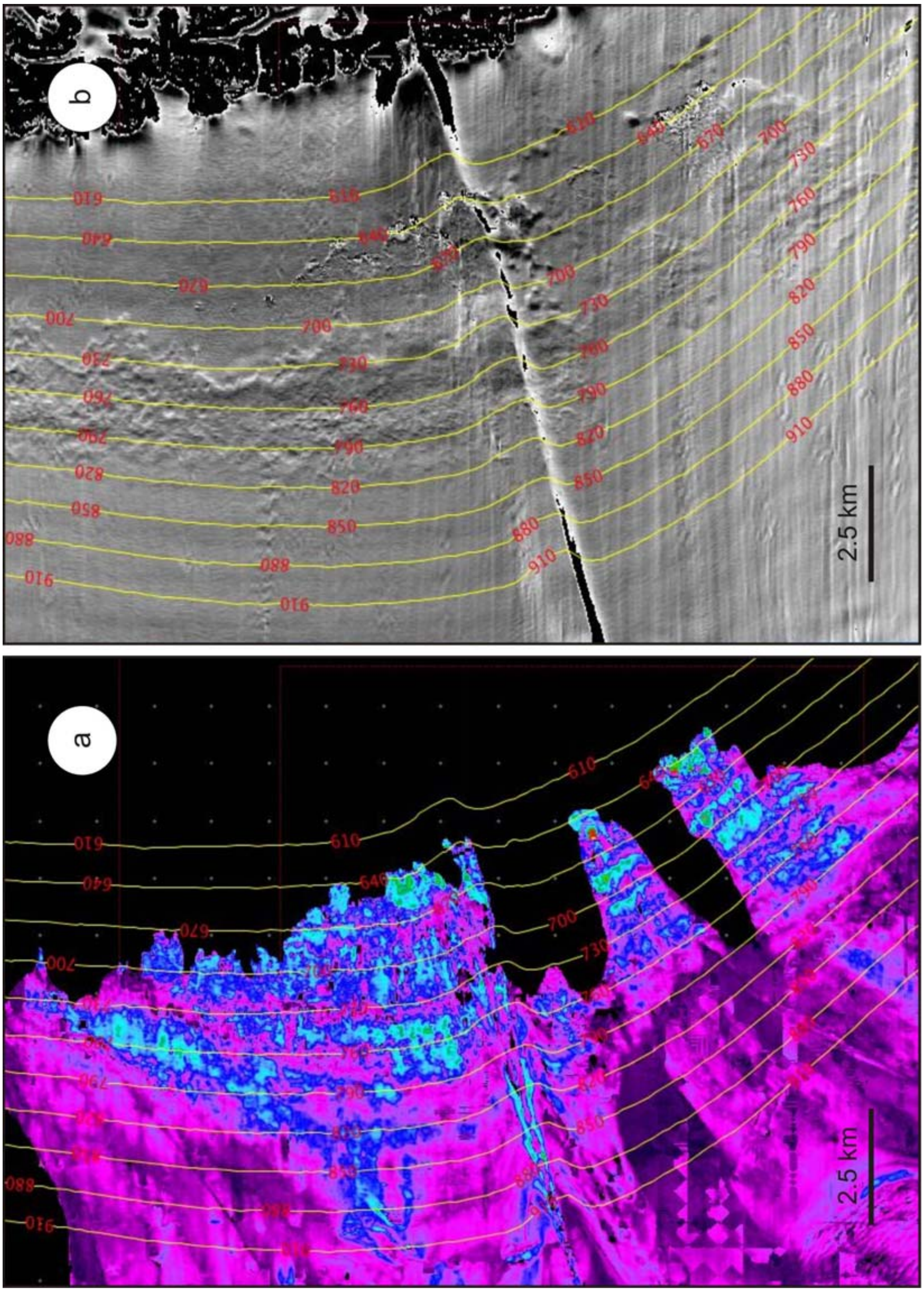

(a): Amplitude map of the BSR; (b): Seabed dip map. Yellow dotted lines: seabed contours in depth (m).

3) 3D seismic cube — TWT map of the seabed at the top

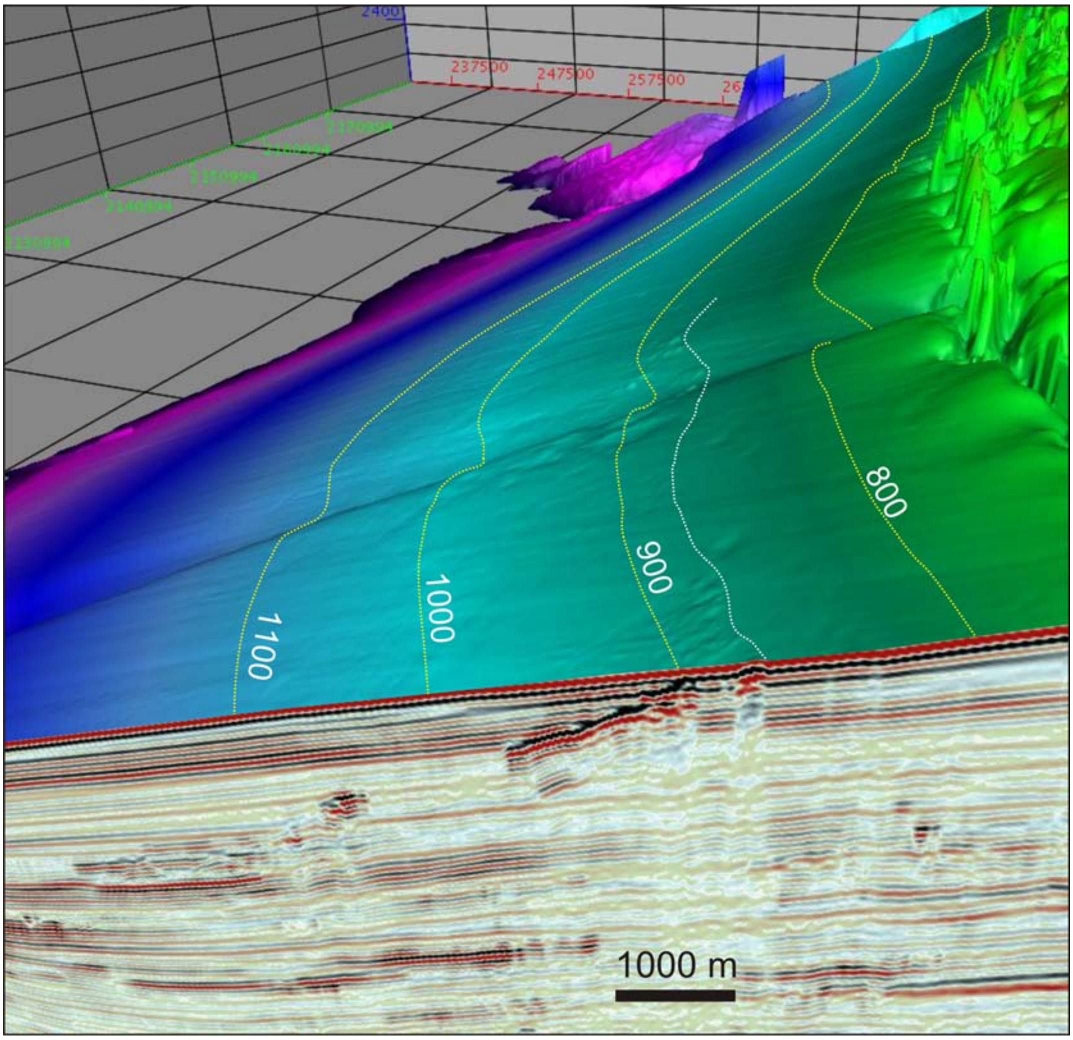

Yellow dotted lines: seabed contours in TWT (ms).

White dotted line: the intersection depth of BSR and the seabed.